ON TRANSPORT MECHANISMS IN SOLAR CELLS INVOLVING ORGANIC SEMICONDUCTORS

Jairo César Nolasco Montaño

Dipòsit Legal: T-1517-2011

UNIVERSITAT ROVIRA I VIRGILI

On transport mechanisms in solar cells involving organic semiconductors

Doctoral thesis presented by

Jairo César Nolasco Montaño

Tarragona 2011

Jairo César Nolasco Montaño

On transport mechanisms in solar cells involving organic semiconductors

Doctoral thesis supervised by
Dr. Josep Pallarès Marzal

Departament d'Enginyeria Electrònica, Elèctrica i Automàtica

UNIVERSITAT ROVIRA I VIRGILI

Tarragona
2011

UNIVERSITAT
ROVIRA I VIRGILI
ESCOLA TÈCNICA SUPERIOR D'ENGINYERIA
DEPARTAMENT D'ENGINYERIA ELECTRONICA, ELÈCTRICA I AUTOMÀTICA

Avinguda dels Països Catalans, 26
Campus sescelades
43007 Tarragona
Tel. (977) 55 96 10
Fax (977) 55 96 05
e-mail: secelec@etse.urv.es
http://www.etse.urv.es/DEEEA/

I state that the present study, entitled "On transport mechanism in solar cells involving organic semiconductors", presented by Jairo César Nolasco Montaño for the award of the degree of Doctor, has been conducted under my supervision at the Department of Electrical, Electronic and Automatic Engineering of this University, and that it satisfies all the requirements to be eligible for the European Doctorate Award.

Tarragona, 20th June 2011

Doctoral Thesis Supervisor

Dr. Josep Pallarès Marzal

Agradecimientos

Al pueblo Español, y en especial al Catalán por haber financiado la beca que me ha permitido llevar a cabo mis estudios de Doctorado en la URV.

A mi tutor de tesis: Josep Pallarès por darme la oportunidad de realizar este trabajo. En particular por recordarme una y otra vez la importancia del orden y la coherencia.

A los profesores y al personal de la ETSE, en particular a Lluís Marsal, Josep Ferrè y Roger Cabré por sus comentarios y observaciones realizadas a mi trabajo, las cuales han contribuido en mi formación como investigador.

A Magali Estrada y Antonio Cerdeira del CINVESTAV, por su colaboración, su honestidad y conocimientos en todos los ámbitos del pensamiento.

A Roberto Pacios, y Christoph Waldauf, de IKERLAN, por darnos la oportunidad de estudiar sus muestras, y su constante interés en la discusión y profundización del conocimiento.

A Emilio Palomares y a su grupo, en especial a Antonio Sanchez. A todos ellos, por su abierta colaboración e impulso para superar cualquier record.

To Elizabeth von Hauff and Bernhard Ecker of EHF in Oldenburg, for their collaboration, their sense of collective work and their courage to overcome any difficulty.

A todos los miembros del tribunal y los revisores de esta tesis: Lluís Marsal, Josep Ferré, Emilio Palomares, Roberto Pacios, Anna Reynal, Miquel Planells, Pilar Formentín, Elizabeth van Hauff, y Holger Bortchert.

Por último agradezco a todas las personas que me ha compartido espacios de su vida, durante el desarrollo de esta tesis y que de alguna u otra forma han fortalecido mi espíritu para llevar a buen fin este modesto trabajo; a toda mi familia, a mis amigos, a mis compañeros de grupo, a la comunidad universitaria extranjera en Tarragona, a los Tarraconenses, y al pueblo de México.

This work has been supported by the Spanish Ministry of Innovation and Science (MICINN) under grant numbers TEC2006-06531, TEC2009-09551, HOPE CSD2007-00007 and TME2009-00401.

A mis Padres, y a Jana

Journal publications arising from this thesis

1) J.C. Nolasco, R. Cabre, J. Ferre-Borrull, L.F. Marsal, M. Estrada, J. Pallares, *Journal of Applied Physics*. 107, 044505 (2010).

2) J.C. Nolasco, A. Sanchez-Diaz, R. Cabre, J. Ferre-Borrull, L.F. Marsal, E. Palomares, and J. Pallares, *Applied Physics Letters* 97, 013305 (2010).

3) B. Ecker, J. C. Nolasco, J. Pallarés, L. F. Marsal, J. Posdorfer, J. Parisi, and E. von Hauff*, Advanced Functional Materials,* 21, 2705 (2011).

4) J.C. Nolasco, A. Sanchez-Diaz, J. Ferre-Borrull, L.F. Marsal, E. Palomares, and J. Pallares, "Effect of C60 thickness on the charge collection in Pentacene/C60 solar cells"*, Submitted to Applied Physics Letters.*

Conference proceedings

1) J. C. Nolasco, R. Cabre, R. Pacios, C. Waldauf, M. Neophytou, E. Palomares, L. F. Marsal, and J. Pallares., *Proceedings of the 2009 Spanish Conference on Electron Devices, CDE'09* , 398, 4800517 (2009).

Work not included in this thesis

1) V. S. Balderrama, M. Estrada, A. Cerdeira, B. S. Soto-Cruz, L. F. Marsal, J. Pallares, J.C. Nolasco, B. Iñiguez, E. Palomares, J. Albero*, Microelectronics Reliability,* 51, 597 (2011).

Conference talks and poster presentations

1) J.C. Nolasco, J. Pallarès, L.F. Marsal, R. Cabré, M. Estrada, and Y. Matsumoto "Conduction mechanisms of hybrid solar cells based on P3HT/N-Crystalline-Silicon", Poster, *EMRS, Strasbourg, France (2008).*

2) J.C. Nolasco, J. Pallarès, L.F. Marsal, R. Cabré, M. Estrada, and Y. Matsumoto "Electrical characterization of n-Crystalline-Silicon/P3HT

heterojunction using a compact equivalent circuit", Talk, *International Symposium on Flexible Electronics, Tarragona, Spain (2008).*

3) J.C. Nolasco, R. Cabré, R. Pacios, C. Waldauf, M. Neophytou, E. Palomares, L.F. Marsal and J. Pallarès, **"**Analysis of the dark current-voltage-temperature characteristics of ITO/P3HT:PCBM/Ca/Al solar cells", *Poster, EMRS, Strasbourg, France (2009).*

4) J.C. Nolasco, J. Pallares, L.F. Marsal, R. Cabre, M. Estrada, and Y. Matsumoto, "Electrical Parameters Extraction of the P3HT in P3HT/n-crystalline Silicon Heterojunction Solar Cells Solar Cells", Poster, *EMRS, Strasbourg, France (2009).*

5) M. Estrada, V. Balderrama, J. Albero, J. C. Nolasco, A. Cerdeira, L.F. Marsal, J. Pallarès, B. Iñiguez, E. Palomares, "Importance of blend preparation in P3HT:PCBM solar cells", Presentation, *International Conference Materials Science in the Age of Nano, Habana, Cuba (2009)*

6) J.C. Nolasco, A. Sánchez-Díaz, R. Cabré, J.Ferré-Borrull, L.F. Marsal, E. Palomares, and J. Pallarès, "Dark conduction mechanism in Pentacene/C60 solar cell", *6th French-Spanish Meeting on Chemistry and Solid State Electronics, Tarragona, Spain (2010).*

7) M. Estrada, V. Balderrama, J. Albero, J.C. Nolasco, A. Cerdeira, L.F. Marsal, J. Pallarès, B. Iñiguez, E. Palomares "Effect of variations in blend preparation on the properties of P3HT:PCBM blend solar cells", Presentation, *2010 27th International Conference on Microelectronics, MIEL 2010, Nis, Serbia (2010).*

8) J.C. Nolasco, Antonio Sánchez-Díaz, R. Cabré, J.Ferré-Borrull, L.F. Marsal, E. Palomares, J. Pallarès, "Determination of the Charge Concentration and Band Offsets using C-V characteristics in Pentacene/C60 solar cells", Poster, 2011 *Spanish Conference on Electron Devices, CDE'2011, Majorca Spain (2011).*

9) B. Ecker, J.C. Nolasco, J. Pallarés, L.F. Marsal, J. Posdorfer, J. Parisi, and E. von Hauff, "Degradation effects related to the hole transport layer in organic solar cells", Poster, *EMRS, Strasbourg France (2011).*

Contents

Chapter 3: P3HT/Si hybrid solar cell

Chapter 4: Pentacene/C_{60} solar cell

Chapter 5: P3HT:PCBM bulk heterojunction solar cells

General Introduction

Motivation

As the evidence of global warming increases and recurrent nuclear accidents occur, it is becoming clear that we will have to find ways to produce electricity without the release of carbon dioxide and nuclear garbage. Renewable energy is an alternative since it neither runs out nor has any significant harmful effects on the environment. Harvesting energy directly from sunlight using photovoltaic technology is widely recognized as an essential component of future global energy production. Among current solar cell technologies, organic solar cells have been widely studied. These materials are attractive because they can be applied to light and flexible substrates. Moreover, their physical properties can be changed by fine tuning their chemical structure. To successfully bring organic solar cells onto the market, good efficiencies, low cost-effective processing, and stable devices need to be achieved. Understanding the underlying physics of the devices is necessary for increasing efficiency, stability and optimizing the technological process. Currently this topic is still in its infancy.

Objectives

In this thesis we study solar cells involving organic materials. Our main objective is to study charge transport in this kind of device in order to identify which charge carrier losses reduce solar cell efficiency. To do so, we:

- identify and solve several open questions on charge transport in organic solar cells;
- electrically model and simulate semiconductor heterojunctions.

- study charge transport in organic solar cells with several architectures.

Methodology

The methodology used in this thesis mainly involves the use of electrical characterization techniques, electrical modeling and simulation rather than fabrication since we received most of the devices analyzed as collaboration from other research groups such as IKERLAN, ICIQ, EHF and CINVESTAV.

We used equivalent circuit device (ECD) models to describe the dark current-voltage (I-V) characteristics, a numerical simulator to model capacitance-voltage (C-V) characteristics, and impedance spectroscopy to calculate Density of States (DOS) distribution. To do so, we:

- revised transport mechanisms and equivalent circuit models that can be applied for organic solar cell modeling;
- modeled dark I-V curves using ECDs;
- used the numerical simulator AFOR-HET to study C-V characteristics; and
- used impedance spectroscopy to calculate DOS distribution in organic bulk heterojunction (OBHT) solar cells.

Scientific contribution

We successfully used models previously applied in amorphous inorganic solar cells to solar cells involving organic materials. We determined that conduction mechanisms such as multituneling capture emission (MTCE) and tuneling-enhanced interface recombination (TEIR) can contribute to dark current characteristics for P3HT/Si, Pentacene (Pc)/C_{60} and Poly[3-hexylthiphene] (P3HT):PCBM solar cells. Specifically, for P3HT/Si we provide a method for determining P3HT parameters that can be used with other organic materials. For Pc/C_{60}, in addition to conduction mechanisms, we consistently simulated energy band diagrams (EBD) and studied the origin of photocurrent losses for different C_{60} thicknesses. Finally, for P3HT:PCBM we calculated the DOS distribution using impedance spectroscopy. We also analyzed the role of the hole transport layer (HTL) in the stability of the device.

Thesis structure

Here we review the main contents of each chapter. At the beginning of each chapter, however, we present a more specific description of its contents.

In chapter 1 we review the fundamentals of organic semiconductors and highlight the differences between organic semiconductors and inorganic ones.

In chapter 2 we describe the fundamentals of solar cell working and characterization. In the second part of chapter 2 we review the theory of modeling.

In chapters 3, 4 and 5 we present the results. In Chapter 3 we determine the transport mechanisms of the P3HT/Si heterojunction solar cell. We also

calculate the electron affinity, charge concentration and width of the assumed DOS distributions for P3HT, and present the fitting methodology using ECDs.

In chapter 4, we analyze the transport in Pc/C_{60} organic solar cells, model and simulate C-V characteristics, study by simulations the built-in potential variations observed in C-V curves, and analyze the charge collection in devices with different C_{60} thicknesses.

In chapter 5 we show the transport in P3HT:PCBM bulk heterojunction solar cells, present an I-V comparison for different solar cells, and discuss how to obtain a more general ECD model for this kind of solar cell. We then describe DOS determination using impedance spectroscopy and use this spectroscopy to study the role of the hole transport layer in P3HT: PCBM solar cells.

In chapter 6 we present a general conclusion, summarize the most important results, and present several topics to be addressed in the future.

Chapter 1

Chapter 1

Organic semiconductor fundamentals and metal-semiconductor junction

In this chapter we discuss the differences between organic and inorganic materials. When studying electrical transport in organic solar cells, it is important to bear in mind the mechanical, optical, electrical and chemical properties of the semiconductor. Here we describe these properties, discuss some of the relations between them, define concepts such as as polaron, exciton, HOMO, LUMO, and Fermi Level, and present a summary of the metal-semiconductor junction theory, which is useful for studying the electrode interfaces in any type of electrical device.

1.1 Should we apply the physics of inorganic semiconductors to organic semiconductors?

Organic semiconductor materials have been studied for around 60 years[1] but it is only in the last two decades that they have begun to be studied more intensively. Researchers became motivated by the discovery of their relatively good semiconductor properties[2,3] as well as their technological properties such as flexibility and low cost deposition[4,5].

Well-established theories of solid state physics exist for inorganic semiconductors, including band theory, in which concepts such as conduction band and valence band are useful for explaining the physics of the electronic devices. For amorphous inorganic materials, concepts such as localized and delocalized states have been used to model their disordered nature and their large quantity of traps. In these amorphous materials the mode of charge transport becomes dominated by localized states[6].

Applications of the above concepts to organic materials depend on the kind of organic semiconductor used. Basically, there are two types of organic semiconductor materials: small molecule materials and polymer materials, details of which will be discussed later. Typically, small molecule materials have crystalline or polycrystalline structures[7], and so crystalline models have sometimes been used to study them[8]. Because of the amorphous nature of polymer materials, the physics behind them are closer to those of amorphous inorganic materials than to those of crystalline ones[9]. However, one property is common to all organic semiconductors: the existence of localized states whose origin is their bond nature (there may be other localized states due to disorder effects or impurities). Therefore, it seems unrealistic to use electrical models that do not consider such localized states.

In this thesis we successfully apply current models to study solar cells involving organic materials[87,88]. Such models, which consider localized states and sometimes interface states, were initially proposed for inorganic

semiconductors. Although similar models can be applied to organic semiconductors, it should be borne in mind that their physical parameters can be different. In this chapter we will define the main physical properties that determine the electrical and optical properties of organic semiconductors.

1.2 Types of Organic Semiconductors and their Structural Properties

Organic materials mostly contain carbon. The tendency of this element to bond to other carbon atoms leads to the formation of hexagonal and pentagonal molecules, which are the core of most organic semiconductors.

Monomers are atoms or small molecules that bind chemically to other monomers to form organic semiconductors. These materials are divided into two general types according to their chemical structure: oligomers, which are molecules formed by only a few monomers (also called small molecule organic semiconductors); and polymers, which are molecules formed by more than 10 monomers. Fig. 1.1 shows these two types of organic materials.

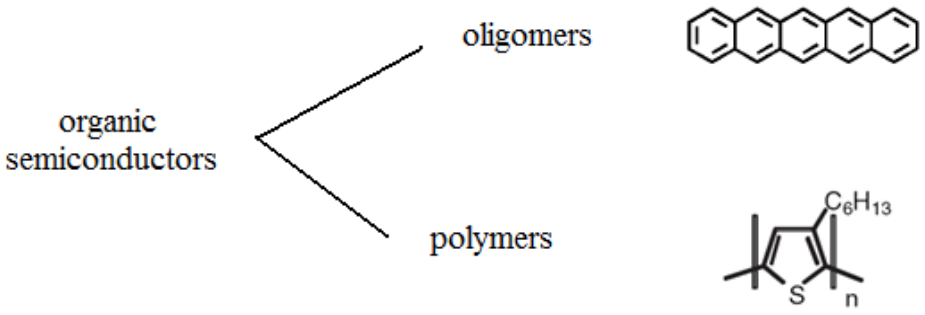

Fig. 1.1 Types of organic semiconductors

Oligomers and polymers form systems of molecules that are linked by Van der Waals forces. This kind of bond gives the material flexibility.

Basically, the macroscopic structural properties of these systems of molecules (macromolecules) depend on their chemical structure and method of deposit. Typically, smaller molecules are more soluble and have lower sublimation temperatures but larger molecules provide better films upon spin coating. Thermal evaporation is therefore the usual technique for depositing oligomers, while polymers are deposited by wetting processes. The fabrication of devices via thermal sublimation requires high vacuum conditions and high temperatures, whereas wetting processes can be performed at room temperature and ambient pressure.

Oligomers and monomers that absorb visible light are often called chromophores and are referred to as dyes if they are clearly soluble and pigments if they are not[1].

Fig. 1.2 shows how a change in chemical structure defines the type of material. This change depends on the position and number of side chains. Side chains are usually attached to core molecules to introduce or improve solubility, which is a good property since it can prevent aggregation between molecules. A change in the side chain defines a material as a dye or as a pigment: dyes are soluble oligomer materials, whereas pigments are insoluble.

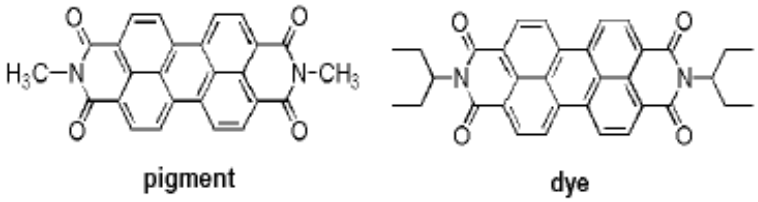

Fig. 1.2: Organic semiconductor molecules.

Flat molecules in particular have a strong tendency to stick together due to π-π interaction and form clusters of solids in many solvents. Bulky side chains can separate these molecules and make it easier for solvent molecules to surround individual ones and dissolve them.

Fig. 1.3 shows some typical molecules used in organic solar cell fabrication. The materials used in this thesis were: $C_{60,}$ PCBM, Pc and P3HT. C_{60} and Pc are small molecule materials so they were deposited by thermal evaporation. The PCBM molecule is based on the C_{60} molecule, with the addition of one radical, which provides the molecule with solubility. PCBM and P3HT were deposited by wet processing techniques.

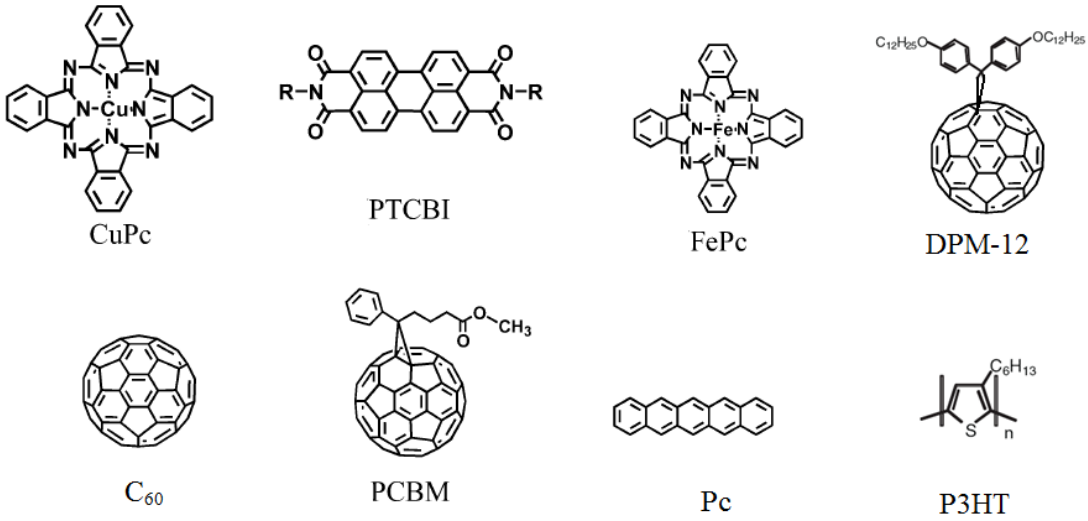

Fig. 1.3 Molecules of several organic semiconductor materials used for solar cell applications.

1.3 The origin of HOMO and LUMO

Due to dimerization, alternation between simple- and a double-bond (π and σ) (see Fig. 1.4) conjugated systems exhibit neither pure covalent nor pure polar bonds. In fact, they represent a separate class in regard to their bond nature, exhibiting huge electron lattice coupling in comparison with inorganic crystalline solids.

This huge electron lattice coupling causes most of the charges to be localized, mainly under thermal equilibrium conditions (in the dark and with

no applied voltage). Therefore, additional energy is needed to generate mobile (free) charge.

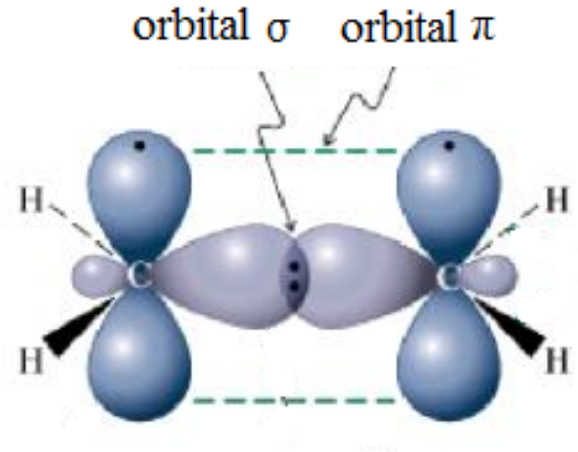

Fig. 1.4: Type π and σ bonds in ethane molecules (CH_2=CH_2).

For each molecule, as the electrons of the π atomic orbitals formed by a sp^2-hybridization of atoms are far from the carbon core, they are easily polarized and can become mobile charge. The occupied orbital of less energy derived from this bond is called HOMO (highest occupied molecular orbital) and the next orbital with a higher energy is called LUMO (lowest unoccupied molecular orbital). Fig. 1.5 shows a scheme of these orbitals.

As Fig. 1.5 shows, the difference between HOMO and LUMO is the band gap (E_g). We know that the lower the E_g, the larger the conjugated π system. Examples of large π systems are phthalocyanines[10,11], naphthalocyanines[12,13] and perylenes[14,15].

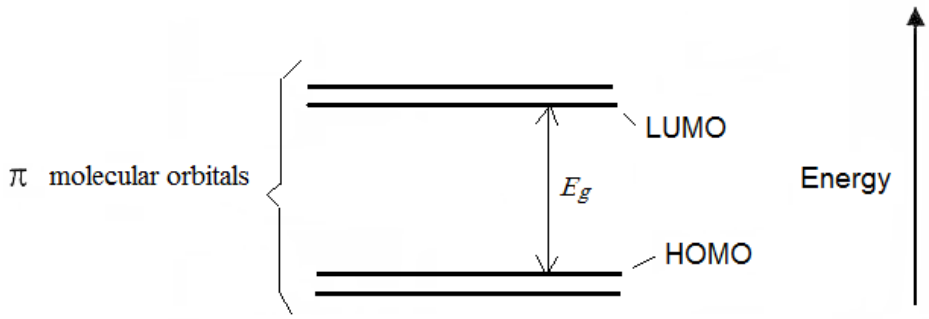

Fig. 1.5: Definition of HOMO and LUMO in organic semiconductors

Due to the strong coupling between the charge carrier and the local lattice relaxation, removing an electron requires somewhat less energy than the HOMO suggests, and an electron joining the molecule gains somewhat more energy than the LUMO suggests. The energies required are called the ionization potential (I_P) and the electron affinity (E_A), respectively[16]. Because such differences in energy are small, HOMO and LUMO levels are typically approximated by I_P and E_A, respectively.

1.4 Optical and electrical properties of organic semiconductors

Solar cells are devices that involve optical and electrical phenomena at the same time. When an organic material is illuminated, excitation states such as excitons and polarons are created. In charge transport, concepts such as the Fermi level, doping and DOS are important for improving solar cell performance.

1.4.1 Excitation in organic semiconductors

The origin of the term polaron for charged quasiparticles is found in classical polar crystals for the associated charge, i.e. the electron repels adjacent electrons while attracting the nuclei, resulting in a polarization of the lattice in its closer vicinity. This accompanying cloud of polarization increases the effective mass of the polarons and decreases their mobility. These quasi particles can be identified by the additional energy levels associated with them and can be represented in the semiconductor bandgap. Polarons in conjugated systems affect not only the polarization in their vicinity but they also change the nature of bonds via excitation and while traveling. Polaron energy has been reported as several tens of meV[17].

The differences in energy between HOMO and LUMO levels from I_P and E_A measurements, respectively, are equal to the polaron energy. The levels of HOMO and LUMO therefore correspond to the polaron level, and polarons can be considered as a mobile charge.

Fig. 1.6 shows an exciton. This is a quasiparticle generated by optical excitation. In organic materials, excitons are usually localized at a molecule and so have considerable binding energy. In inorganic materials, on the other hand, exciton binding energy is estimated to be around 16 meV. This means that excitons become important predominantly at lower temperatures[18].

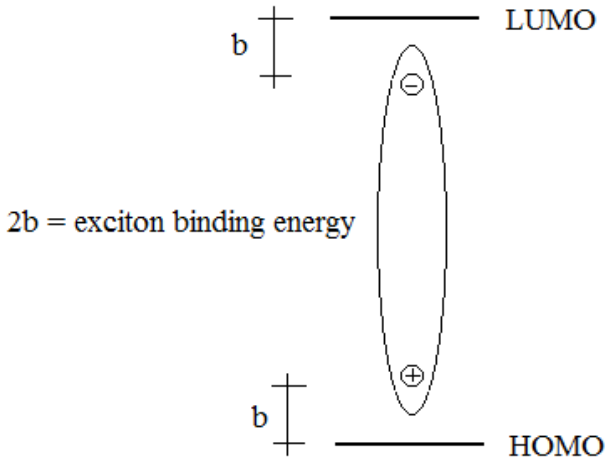

Fig. 1.6: Exciton binding energy

In organic semiconductors the exciton binding energy (see Fig. 1.6) is estimated to be between 0.4eV[19,20] and 0.95 eV[21], depending on the kind of material. Since excitons are formed by an electron and a hole, these quasiparticles have a neutral electric charge. This is a key point that must be considered in solar cell design, which will be discussed in the next chapter.

A consequence of the weak electronic delocalization is that organic semiconductors have an important peculiarity with regard to their inorganic counterparts. This is the existence of well-defined spin states (singlet and triplet), like in isolated molecules. These states have different energy levels

and depend on the material's morphology and the system in which the material is involved. They therefore affect the separation or recombination of the exciton differently.[22]

1.4.2. Importance of the Fermi level

The energetic position of the Fermi level (E_F) in a semiconductor represents the balance between the concentration of holes and electrons occupying allowed energy levels under the equilibrium condition. When designing devices, the energetic position of the Fermi level is important for three reasons:

1) Together with the work function of the metal, the Fermi level determines whether a blocking or ohmic contact is formed at the semiconductor/metal interface;

2) The relative position of the Fermi level with respect to the bands is a measure of the type of conductivity, i.e. whether the semiconductor preferably conducts holes the Fermi level is close to the Valence band (V_B) and to the Conduction band (C_B) if the semiconductor conducts electrons. These semiconductors are referred as p-type and n-type, respectively. In theory, HOMO and LUMO levels were defined for an isolated molecule but as this concept can be extended to a film of material, in this work we will refer to such energy levels as V_B and C_B, respectively.

3) In materials with tails and deep localized states, such as organic semiconductors, the position of the Fermi level determines the charge transport: when the E_F is in the middle of the band gap, the probability of charge recombination increases; when E_F is in the energy region of the deep states, transport can occur by means of multi-trapping and release process (MTR); and when E_F is close to the conduction band, hopping is more likely.

This is the typical transport suggested for organic thin film transistors[23,24]. In the literature it is demonstrated that hopping transport in disordered organic semiconductors can be mathematically equivalent to band transport with MTR[9,25].

The position of the Fermi level can therefore be written as a function of the effective DOS in the conduction band (N_C) or in the valence band (N_V) depending the type of semiconductor, as well as of the effective concentration of donors (N_D) and acceptors (N_A). For n-type semiconductors, this gives:

$$E_F = E_C - k_B T \cdot In\left(\frac{N_C}{N_D}\right) \tag{1.1}$$

For p-type semiconductors, this gives:

$$E_F = E_V - k_B T \cdot In\left(\frac{N_V}{N_A}\right) \tag{1.2}$$

E_V and E_C are the energy levels of the V_B and C_B, respectively. In organic materials the magnitudes of N_D and N_A are usually affected by trap states. When voltage is applied and/or the semiconductor is illuminated, the concept of a Fermi level can no longer be applied. Upon illumination, for example, the higher concentration of electrons in the C_B shifts E_F upwards while the higher concentration of holes in the V_B requires shifting E_F down at the same time. As a consequence, two separate Fermi levels—the so-called quasi Fermi levels—are introduced to describe the situation under this non-equilibrium condition[26]:

$$E_{FN} = E_C + k_B T \cdot In\left(\frac{N_C}{n_e}\right) \tag{1.3}$$

and

$$E_{FP} = E_V + k_B T \cdot In\left(\frac{N_V}{p}\right) \tag{1.4}$$

where n_e and p denote the charge concentration of free electrons in the C_B and free holes in the V_B, respectively. E_{FN} and E_{FP} are the quasi Fermi-levels associated with the balance of electrons and holes, both of which exist at the same time in one semiconductor. Fig. 1.7 shows p-type material in the dark (left) and under illumination (right). In the dark, the balance of charge is represented by E_F,. Under illumination, charge concentrations of both electrons and holes increase above their thermodynamic equilibrium value. Hence $E_{FP} < E_F < E_{FN}$, which results in a shorter distance of both quasi-Fermi levels from their corresponding bands.

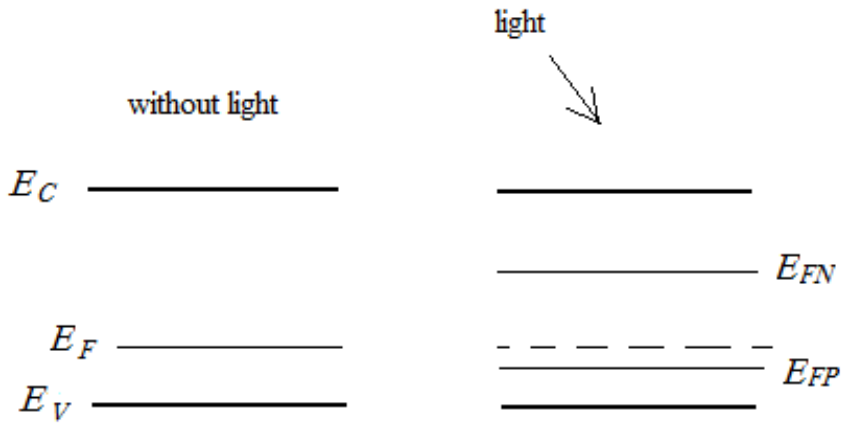

Fig. 1.7 Fermi and quasi-Fermi levels for a p-type semiconductor

It is important to bear in mind that the difference between these quasi-Fermi levels corresponds to the thermodynamic limit for the open circuit voltage in a solar cell in both a single material and in a junction (the latter will be explained in detail in chapter 2).

1.4.3 Localized density of states

The defect states in organic semiconductors can be represented by DOS distributions. Localized DOS are those whose energy is into E_g, as is indicated in Fig. 1.8, which uses a Gaussian DOS distribution. Delocalized DOS refer to the states out of E_g. Although localized DOS have been characterized using Gaussian and exponential distributions[27-29], to determine the exact nature of these states is not trivial. Their origin can be found in material amorphicity, interfacial defects, and external impurities. In general, amorphicity is responsible for DOS distributions close to the energy bands, while interfacial defects and external impurities are expected to create deep states[1].

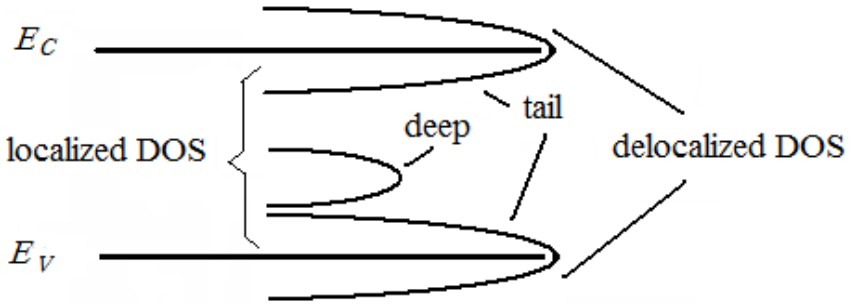

Fig. 1.8 DOS distributions in organic semiconductors

Depending on the DOS, in non-equilibrium conditions the occupancy in the material can change and therefore so can the quasi-Fermi levels. These trap states can also act as recombination centers of free charge carriers. Their characterization and reduction are important for increasing the performance of any organic electronic device.

The mathematical expression for a Gaussian DOS is given by:

(1.5)

where σ is the variance of the distribution, N is the maximum of the DOS, and E is measured relative to the center of the DOS. For simplicity, exponential DOS have sometimes been used to approximate these Gaussian distributions[27].

1.4.4. Doping

In inorganic semiconductors, doping occurs via the introduction of dopant atoms that provide additional free charge carriers at room temperature and the extra charge increases conductivity in the doped material. In organic semiconductors, doping is usually achieved by introducing foreign molecules rather than atoms.

Examples of functionalities that enable electron acceptor properties are: CN, CF_3, F, = O (keto-groups) and diimides[30]. These groups are known as electron-withdrawing groups if they are attached to an unsaturated (conjugated) system. Most organic semiconductors behave more like p-type materials[30].

It has been suggested that in organic semiconductors the DOS or defect states act like donors or acceptors[31]. Defect states preferentially trap one type of charge, leaving the other free to contribute to conductivity. A material in which defects preferentially trap electrons (donors near the valence band) acts as if it is doped p-type. This is the case for materials such as P3HT (see Fig. 1.9, which shows a p-type semiconductor). Although trap holes in uncompensated p-type defect can contribute to conductivity, the compensated p-type defects trap free holes degrading such conductivity Doping by DOS is therefore not very good at all[32].

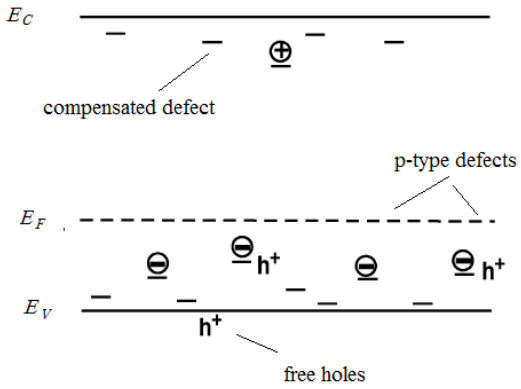

Fig. 1.9 Trap states in a p-type organic semiconductor.

It has also been shown that oxygen absorption dopes organic semiconductors and causes an increase in photoconductivity.[33,34]

1.5 Metal-semiconductor junction

The theory of contacts between doped semiconductors and metals was developed in 1938 by Mott and Schottky[35,36]. Since then, charge injection from metallic contacts into inorganic semiconductors has been extensively studied and is explained in detail in the literature on semiconductors[26]. However, application of this theory to metal-organic semiconductor junctions depends on the quality of their interface. Fig.1.9 shows the EBD as is expected before (a) and after (b) contact for an ideal junction. As we can see, after contact, band bending occurs at all interfaces and the Fermi levels and workfunctions equalize.

Band bending can be qualitatively predicted by assuming that the edges of the LUMOs and HOMOs maintain the absolute energy values they had before contacting. The bulk of the semiconductor maintains the same distance to the equalizing Fermi-level. The electron affinity and ionization potential of the semiconductors do not need to change even where band bending occurs since the corresponding vacuum level follows both the band curvature and vertical shifts.

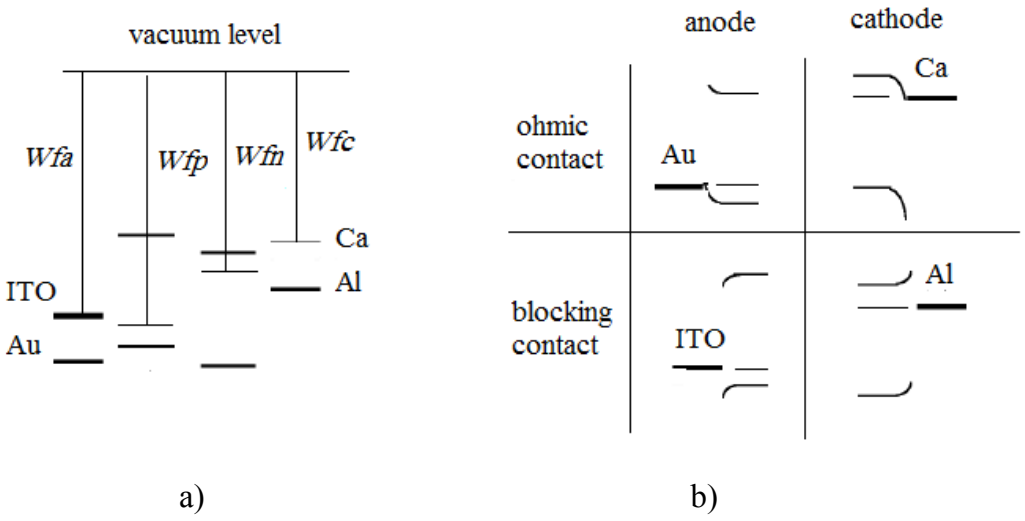

Fig. 1.9 Energy band diagrams a) before contact and b) after contact (ohmic and blocking contact for an anode and cathode).

The direction of the band bending depends on whether the work function of the electrode (W_{fa} = anode; W_{fc} = cathode) is above or below the work function of the semiconductor (W_{fn} = n-type, W_{fp} = p-type). If $W_{fa} > W_{fp}$ and $W_{fc} < W_{fn}$, an ohmic contact is formed, whereas if $W_{fa} < W_{fp}$ and $W_{fc} > W_{fn}$, a blocking contact is formed. Photoexcited electrons from the C_B of the n-type material meet a barrier before they can reach the Al electrode. The same occurs for holes from the V_B near the ITO contact. Since these contacts can become non-blocking when the potential of the electrode changes, they are also called rectifying or Schottky contacts.

Fig. 1.9b illustrates how the situation improves if Au and Ca are used as contact materials. Practice confirms that organic devices using Au and Ca instead of ITO and Al show considerably higher open circuit voltages and often higher photocurrents and external quantum efficiency (EQE)[37]. However, because the *Wf* of Ca is lower than that of Al, Ca is more prone to oxidation than Al. Gold electrodes are expensive, must be very thin to become transparent, and are more difficult to pattern via etching. For these reasons, Al or Ca/Al and ITO electrodes are more suitable for research devices because they can be reproduced more easily.

The charge transport model for the junction metal semiconductor will be presented in the next chapter.

Chapter 2

CHAPTER 2

Organic solar cell fundamentals and conduction mechanisms

In this chapter we review the fundamentals of photovoltaic energy conversion in organic solar cells, discuss the advantages of the different types of organic solar cells, and define the I-V parameters and their optimization of the solar cell.

Electrical equivalent circuit diagrams (ECD) are important tools for studying electronic devices. In this chapter we explain the relationship between each element in the ECD and the region of the device. Finally, we present an overview of the most common current mechanism found in organic heterojunctions.

2.1 A brief history of solar cells

In 1839 Becquerel first reported the photovoltaic affect[38]. However, the birth of the solar cell really occurred at Bell Laboratories in 1954 when Pearson and Fuller made a shallow diffused p-n junction in a thin slice of crystalline silicon and demonstrated conversion efficiencies of 6%[39].

The introduction of thin film technology in the 1970s, referred to as second generation photovoltaics, was based on polycrystalline and amorphous inorganic materials[40]. The main advantage of thin film solar cells is their low cost due to low-cost processing and the use of relatively low-cost materials. The third generation of solar cells relies on more elaborate structures and materials whose physics do not depend on the typical p-n junction, e.g. tandem cells from IV and III-V semiconductors[41], quantum dots solar cells[42], dye-sensitized solar cells[43], and organic solar cells[5].

With regard to organic solar cells, the first promising solar cell efficiency was demonstrated by Tang[44] for a bilayer solar cell. In the 1990s the synthesis of high-purity conjugated polymers enabled the fabrication of solar cells deposited from solutions[5]. Recently there has been intensive research into the materials, physics, stability, and efficiency of these technologies. Like thin film technology, this research is motivated by the promise of low-cost processing, the use of relatively low cost materials, and the fact that these materials can be deposited on flexible substrates.

Improvement in efficiency over the last 35 years is shown in figure 2.1 for different solar cell technologies. Note that organic solar cell technology (below right in figure) is still improving, while other technologies are more or less reaching stabilization. Recently, efficiencies approaching 8% have been achieved for this technology[45].

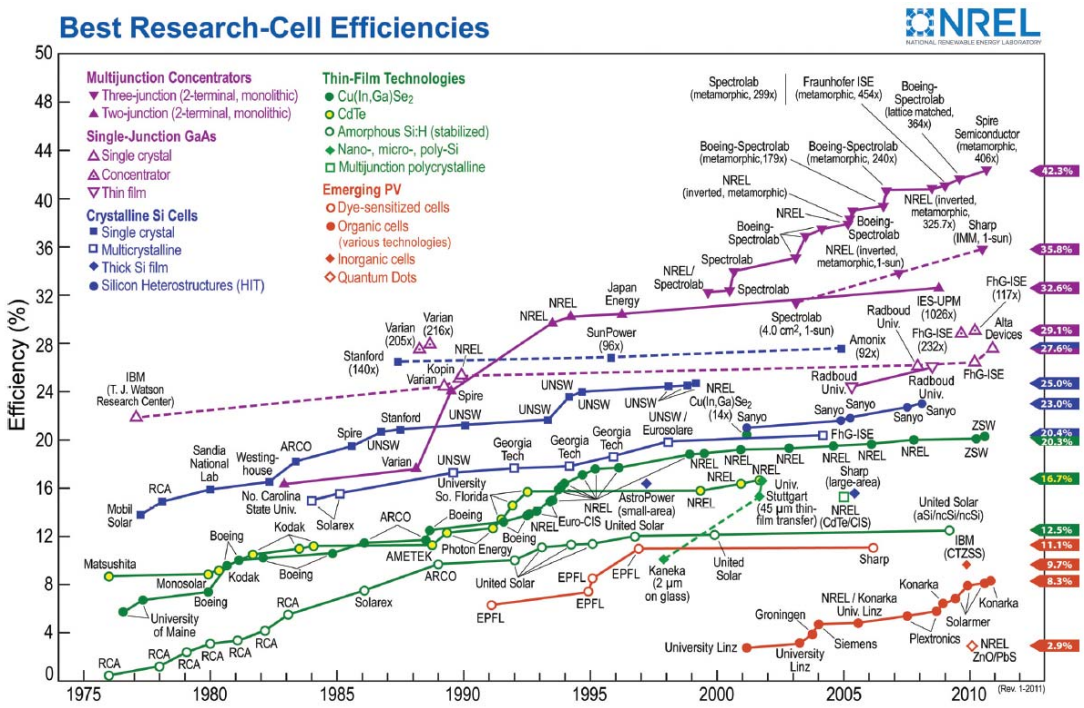

Fig. 2.1: Improvement in solar cell efficiency for different technologies. Copyright NREL.

2.2 Energy conversion in organic solar cells

A solar cell can be viewed as a solar-light driven electron pump. The higher the electrons can be pumped, the higher voltage the solar cell can develop. The maximum current is determined by the pump rate. If pumping can promote 100 electrons/s from the valence band into the conduction band, the highest possible continuous current of electrons flowing through the external circuit is 100 electrons/s. If the current flow through the external circuit is reduced by, e.g., a load resistor to, for example, 80 electrons/s, the remaining 20 electrons/s will drop back by recombination before they can leave the device[46]. Let us introduce the physics of the solar cell using a typical heterojunction band diagram. Figure 2.2 illustrates the photovoltaic effect in a short circuit (Fig. 2.2a) and when the device is connected to an external load R_L (Fig. 2.2b). Note that the excitons are created on both sides of the junction due to photon absorption. Once these excitons diffuse to the interface, their dissociation occurs. To produce exciton dissociation we need

either a stronger electric field ($F > 10^6$ V cm^{-1}) or a donor-acceptor heterojunction.[47] Finally, the free charge is transported by diffusion or under the influence of an internal electric field to the electrodes

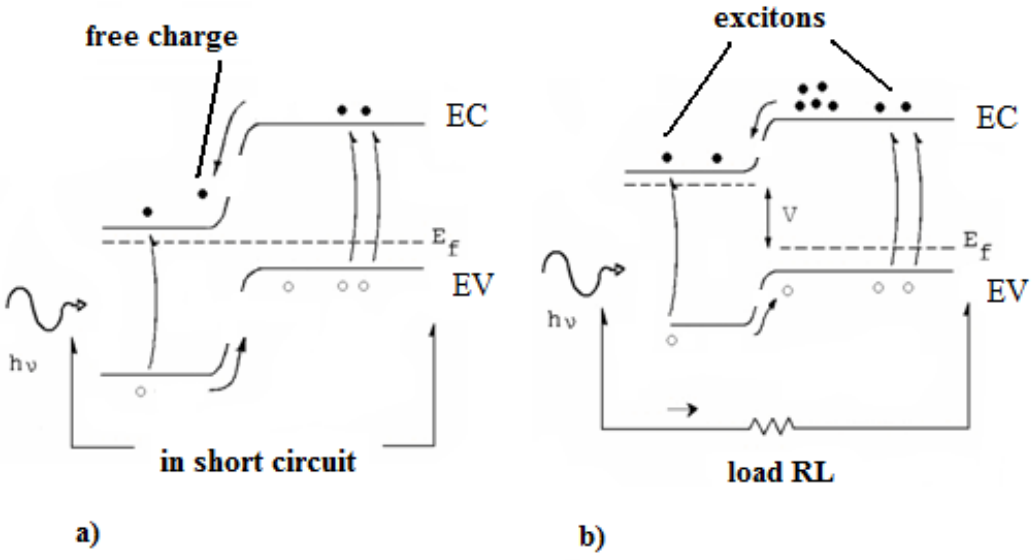

Fig. 2.2: Energy band diagrams for an arbitrary p-n heterojunction a) in short circuit conditions and b) connected to an external load R_L

In Fig. 2.2a all Fermi levels are aligned because of the short circuit conditions, while in Fig. 2.1b a difference of potential (V) is created in the junction interface. This potential is created due to the incident light. When R_L is very high (equivalent to an open circuit), V corresponds to the open circuit voltage.

Each process of the energy conversion is described in more detail below.

1) Absorption of photons

Fig. 2.3 shows the absorption coefficient for P3HT and PCBM. The same figure also presents the standard A.M. 1.5 terrestrial solar spectrum. Note that P3HT presents relatively high absorption coefficients (10^5 cm^{-1}) and a broad distribution. These kinds of properties are typical of materials with localized DOS distributions, such as those used in thin film technologies[49]. Due to the generally small overlap of the absorption coefficient and the solar spectrum, a maximum of 30 % of the total spectrum is absorbed, though of course the exact percentage depends on the material's absorption coefficient. To overcome this drawback, tandem structures have been proposed[50,51]. In these structures, several heterojunctions are connected in serial configuration and each heterojunction overlaps with different regions of the solar spectrum.

Another drawback with this kind of material is the low exciton diffusion length (around several tens of nm). This limits the maximum length of the absorber layer and usually also the absorption efficiency. Absorption in any material is given by: $I = I_o \cdot e^{-\alpha x}$, where I_o is the light intensity in the border of the film, α is the absorption coefficient, and x is the distance from the border to any distance of the film. For example, the exciton diffusion length of the excitons for P3HT is reported to be around 10 nm[52] (the maximum thickness for all excitons to reach the borders) for this thickness and, using the absorption equation and the maximum of the absorption coefficient $\alpha = 1 \times 10^5$ cm^{-1} (from Fig. 2.3), we find that only 10% of the incident light can be used. To overcome this drawback, reflective back contacts have been proposed[53].

Since organic solar cells comprise several thin layers of material with different optical properties, the interfaces lead to multiple reflections that produce an optical interferences effect. Consequently, there is a complicated interplay between the relative optical constants of the materials and their thickness[53]. These approaches mainly focus on increasing the photocurrent

but they are normally studied once other losses such as recombination become less dominant.

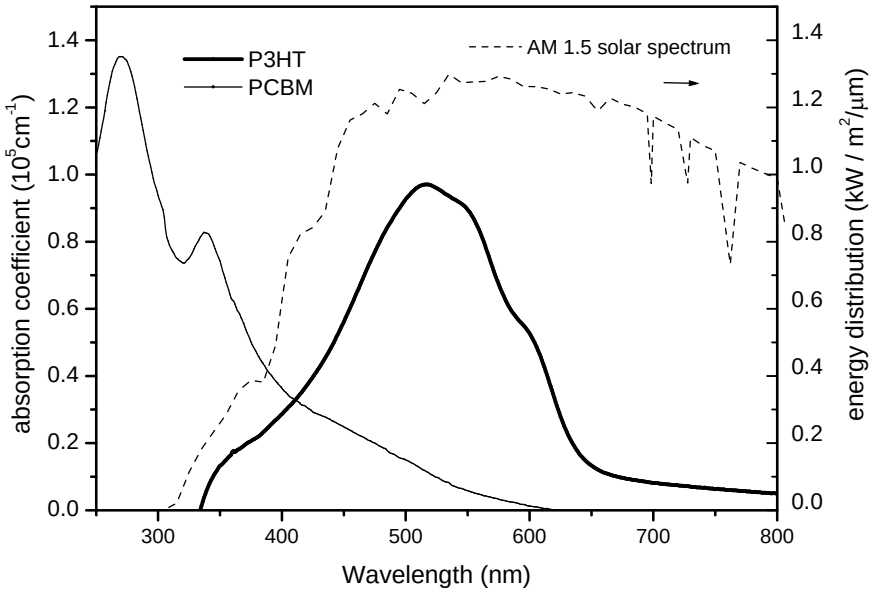

Fig. 2.3 Absorption coefficient for P3HT and PCBM, in addition the standard A.M. 1.5 terrestrial solar spectrum is showed.

2) Exciton diffusion

Ideally, all photoexcited excitons should reach a dissociation site. Since this site may be at the other end of the semiconductor, their diffusion length should be at least equal to the required layer thickness (for sufficient absorption), otherwise they recombine and photons are wasted. Exciton diffusion in polymers and pigments is typically around 10 nm[54,55] .However, some pigments such as perylenes are believed to have exciton diffusion lengths of several 100 nm[14].

Since excitons have a neutral electric charge, it has been proposed that their motion is not influenced by any electric field and that they therefore diffuse via random hops. This hopping mechanism has been described via the

Forster mechanism[56] for singlet excitons and via the Dexter mechanism[57] for triplet excitons. Singlet excitons can move more quickly than triples (ns vs μs or ms) but they also decay more quickly.

3) Exciton dissociation

Fig. 2.4 shows an electronic state diagram, which is typically used to explain exciton dissociation. When the exciton in the donor (p-type material, which usually absorbs more photons) reaches the interface, there is a charge transfer process for electrons from the exciton level to states of lowest energies. Such states can be one where the exciton is still somewhat bound, STB (bonding state), or a transit laying state STL. For the electron of the exciton to become a free charge, it must reach the free state (STF), which can be the LUMO of an acceptor. If the electron passes through STB, the electron-hole pair is closer, so the probability of recombination increases. On the other hand, if an electron goes through STL, separation is more likely.

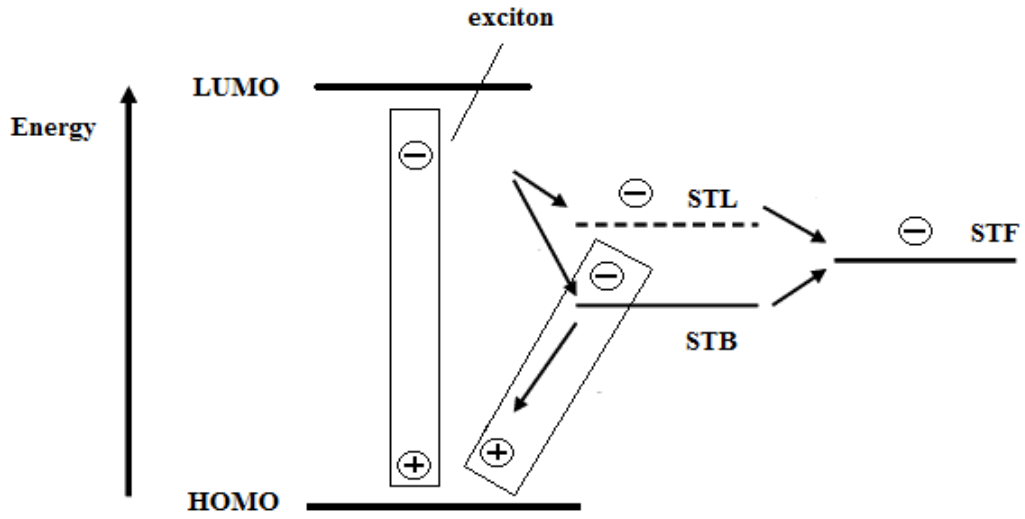

Fig. 2.4 Electronic state diagram for exciton dissociation

However, it is not yet clear why the electron can preferentially pass through STL since the charge always tends to low energy states. And if the electron goes through the difficult route (through STB), it is not yet clear why the separation occurs[58]. One possibility is that an internal electric field can contribute to charge separation.

4) Transport and charge collection

It is well known that the transport of separate charges to the electrode is by hopping. Because of the low diffusion length of such carriers, internal electric fields are necessary to extract such charges, especially when the active materials have a low mobility[9]. This transport can be affected by recombination during the journey to the electrodes. Also, interaction with atoms or other charges can slow down the speed of travel and thus limit the current.

Important in any electronic device are the electric contacts. In the final section of chapter 1 we reviewed the conditions required to obtain an ohmic contact. It is necessary to inject or extract charge without electrical losses.

2.3 Difference between organic and inorganic solar cells

The main difference between organic and inorganic solar cells is that in inorganic solar cells, photons create electron-hole pairs (excitons) of low bond energy that can lead to free charge. In organic solar cells, on the other hand, the photons create electron-hole pairs of relatively high bond energies. Therefore, while in inorganic solar cells the maximum length of the absorber layer is the diffusion length of the minority carriers (which may be electrons in a p-type material and holes in an n-type material depending on the type of absorber material), in organic solar cells the maximum length is the diffusion length of the exciton.

In fact, if the possible exciton recombination is excluded, I see no fundamental differences in the loss mechanism between organic and inorganic solar cells, especially with regard to thin film technology and bearing in mind that the nature of trap states in bulk and interfaces can be different.

2.4 MIM model or P-N heterojunction model?

EBD is useful for visualizing the transport mechanism suggested by mathematical models. In theory, electronic state diagrams and MIM model can be used to explain the photovoltaic phenomenon in organic solar cells[48].

However, the use of these simple models sometimes leads to controversial debate about exciton dissociation for electronic state diagrams, or whether to omit important characteristics of materials such as internal electric fields for the MIM model.

The main characteristic of the MIM model is that band bending in the device is determined by the difference in the work functions of the electrical contacts. This results in a constant electric field through the device (see Fig. 2.5). Once the excitons are separated at the internal electric field of the interface (the slope of the bands), the carriers drift towards their respective electrode.

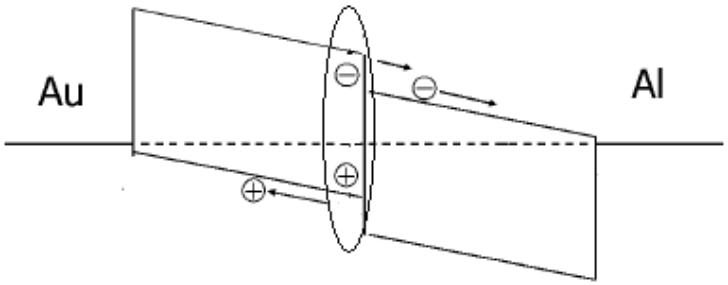

Fig. 2.5 MIM model for a bilayer organic solar cell.

However, this model cannot explain photocurrent degradation due to changes in the internal built-in electric fields derived from the charge carrier concentration previously studied using C-V curves[47]. These changes in carrier concentration are related to the purity and degradation of the active materials.

In this work we found the p-n heterojunction model consistently explains:

- the behavior of C-V characteristics. The MIM model does not explain the capacitance variation vs voltage;
- interface barriers obtained from the transport mechanism model used to study dark I-V curves at different temperatures;
- increases in recombination in Pc/C_{60} solar cells as the thickness of C_{60} increases (explain in chapter 4).

2.5 Organic solar cell architectures

Here we present the key characteristics of various organic solar cell architectures.

1) Single layer cell

Single layer structures consist of only one semiconductor material and are often referred to as Schottky type devices or Schottky diodes since charge separation occurs at the rectifying junction with one electrode[59-61] (see Fig 2.6).

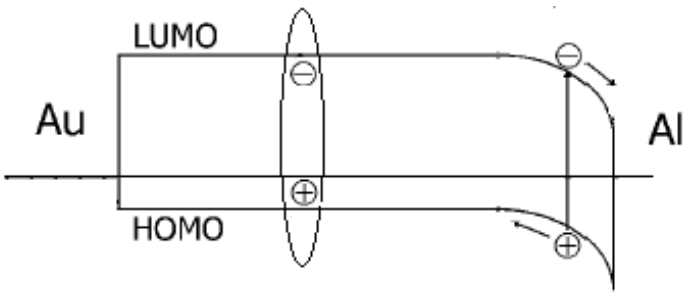

Fig. 2.6: Single layer solar cell

The other electrode interface is assumed to be ohmic in nature. The structure is simple but the photoactive region is often very thin and, since both positive and negative photoexcited charges travel through the same material, recombination losses are generally high.

2) Bilayer Cell

This structure benefits from the separated charge transport layers that ensure connectivity with the correct electrode and give the separated charge carriers only a small chance to recombine with their counterparts. The drawback is the small interface that allows only excitons of a thin layer to reach it and get dissociated[62] (see Fig. 2.7).

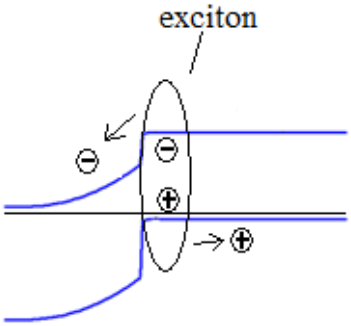

Fig. 2.7: Bilayer cell

3) Organic bulk heterojunction (OBHT) solar cells: melt and ordered structure

The advantage of this type of cell is the large interface area if molecular mixing occurs on a scale that allows for good contact between like molecules (charge percolation) and enables most excitons to reach the p/n interface[63-65] (see Fig. 2.8). This can usually be only partly achieved so the defects in the network structure, particularly connectivity with the correct electrode, represent a technological challenge.

Ordered structures are generally made by infiltrating polymers into nanostructured oxides, which are used as template. The nanostructure shown in Fig. 2.8 is considered ideal because it has small, straight pores and is thick enough to absorb most of the sunlight.

The pore radius should be slightly less than exciton diffusion length to enable maximum exciton harvesting. The thickness of the nanostructure

should be 300-500 nm so that the infiltrated polymer can absorb most of the incident light. The pores should be straight to provide the most direct path to the anode and cathode. The most common semiconductor oxides for these devices are: SnO_2[66], TiO_2[67], and ZnO[68,69]. Other interesting materials used to fabricate this kind of solar cell are carbon nanotubes[70].

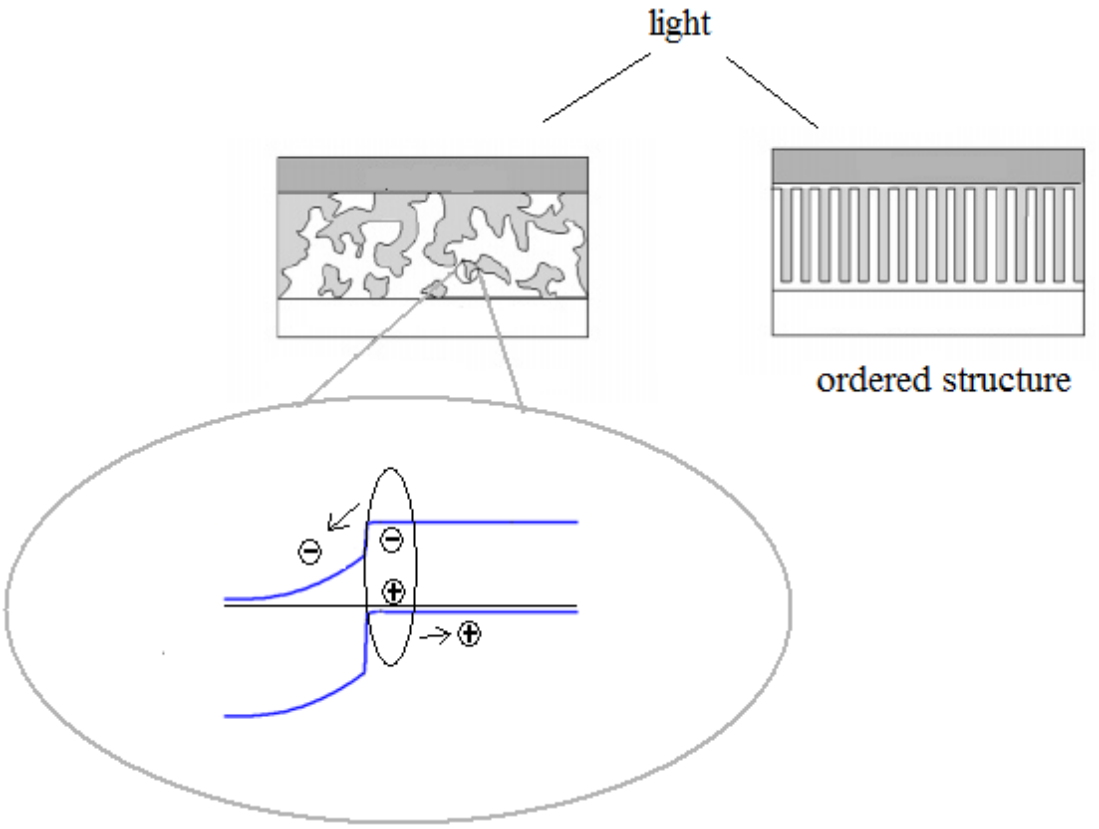

Fig. 2.8: OBHT solar Cells: melt and ordered structure

4) Hybrid cell

Hybrid solar cells are made up of both organic and inorganic materials. One approach involves introducing inorganic quantum dots into a semiconductor polymer matrix[42]. Another involves the use of inorganic semiconductors as active materials together with polymer semiconductors[71]. Finally, several studies are using well-known crystalline materials together with organic semiconductors. These cells have been fabricated with two aims in mind: (i)

to use the good properties of inorganic materials, such as conductivity and absorption, together with the technological features of organic materials in order to achieve good efficiencies[71]; and (ii) to study the properties of organic materials.

For more details, I recommend the review outlined in reference 72, which though not recent, provides detailed characteristics of the materials used for different solar cell architectures with acceptable efficiencies.

2.6 Solar cell I-V characteristics

As an electric device, solar cell characterization is conducted using the illuminated I-V curve. One example of this curve for a device with good performance is shown in Fig. 2.9

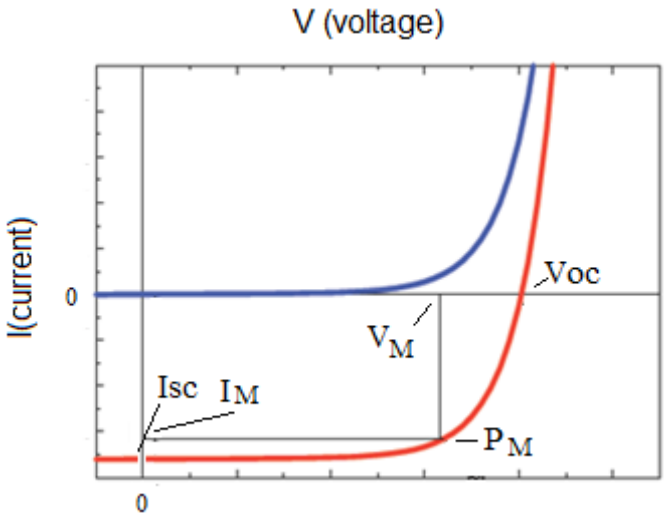

Fig. 2.9: I-V curve in the dark and under illumination for a cell with good performance.

If we consider the I-V curve, therefore, the maximum power is the maximum product of current and voltage that can be found among the data points in the fourth quadrant. This maximum area gets larger as the I-V curve begins to resemble a rectangle with the area *Voc* x *Isc*, the open-circuit voltage and the

short-circuit current, respectively. The ratio between these two areas is a measure of the quality of the shape of the I-V characteristics:

$$FF = \frac{(I \cdot V)_M}{I_{sc} \cdot V_{oc}} \tag{2.1}$$

Therefore:

$$P_M = (I \cdot V)_M = V_{oc} \cdot I_{sc} \cdot FF \tag{2.2}$$

The higher the *FF*, the more the I-V characteristics resemble a constant current source with a maximum voltage and the higher the electric power that can be extracted. The maximum voltage/current (V_M, I_M) combination that gives the largest power rectangle is called the maximum power point P_M. Therefore, any electrical appliance connected to a solar cell can utilize P_M if the load resistor is given by $R_L = V_M/I_M$. Otherwise, power would be wasted when heating the series resistor if $V < V_M$ or via increased current losses through the ideal diode and shunt resistor if $V > V_M$.

To describe the power conversion efficiency of a solar cell, the maximum output power P_M must be related to the power of the incident light P_{light}. Using Eq. 2.2 to express P_M and considering the wavelength dependence of the parameters involved, we can write:

$$\eta(\lambda) = \frac{I_{SC}(\lambda) \cdot V_{oc}(\lambda) \cdot FF(\lambda)}{P_{light}} \tag{2.3}$$

Because of the wavelength and intensity dependence, power conversion efficiencies are only meaningful for a given spectral distribution and intensity. This can be the solar spectrum or the spectrum of the artificial illumination.

To compare the efficiencies of solar cells, solar radiation standards have been defined. The most common current standard is the AM1.5 spectrum, which can be approached by a commercial solar simulator. If international recognition of the solar power conversion efficiency number of a cell is desired, the cell should be measured by one of the internationally recognized institutions that offer solar cell efficiency measurements, e.g. the National Renewable Energy Laboratories (NREL) in Golden (USA) or the Fraunhofer Institut for Solar Cell research in Freiburg (Germany).

2.7 Solar cell optimization

Three parameters need to be improved in order to obtain better efficiencies: *FF*, *Jsc* and *Voc*. Below we discuss the limits of these parameters.

1) Fill factor

In a more basic model, the fill factor can be affected by parasitic resistances. These are series R_S and shunt resistance $R_{SH.}$ The origin of R_S may be the bulk of the active materials or contact resistance, while the origin of R_{SH} may be parallel recombination paths to the main junction. Fig. 2.10 shows the effect of a high R_S and low R_{SH} on light I-V curve. An estimated value of these resistances can be calculated from the slope of the illuminated I-V curve around *Voc* for R_S and around J_{SC} for R_{SH}.

To avoid these effects, R_S must be as small and R_{SH} must be as high as possible. In organic materials, acceptable values are in the order of several tens and 10^6 ohms, respectively.

Similarly, as in inorganic solar cells, in organic cells the maximum value of the *FF* may be limited by the *Voc*[74].

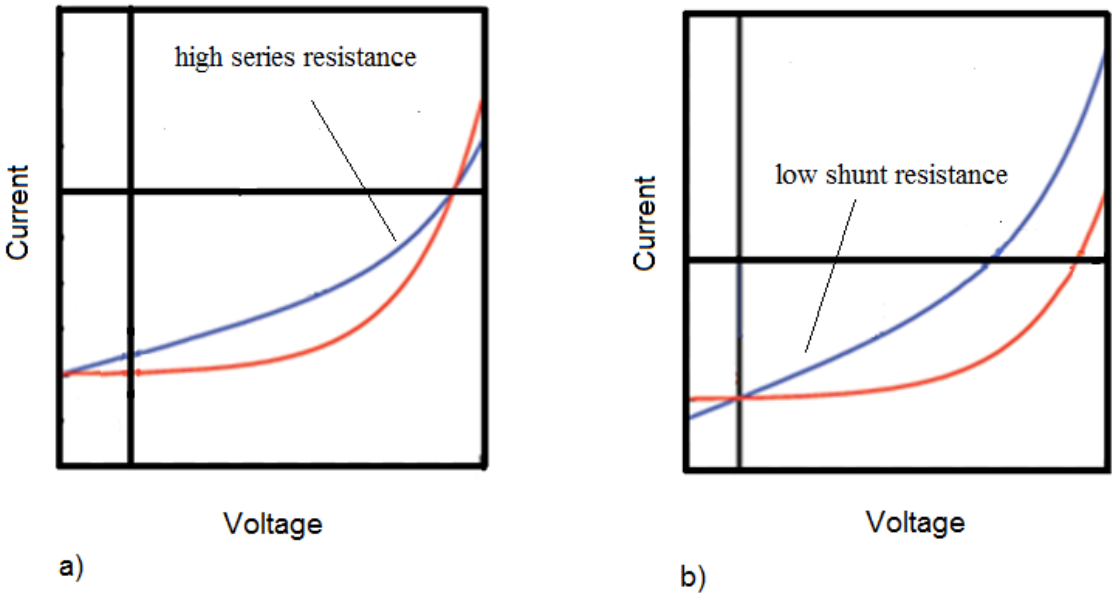

Fig. 2.10 Effect of electrical resistances on illuminated I-V curve

2) Short circuit current density

The maximum *Jsc* is given by:

$$J_{sc} = \int_{AM1.5} q \cdot \eta_{EQE}(\lambda) \cdot N_{ph}(\lambda) d\lambda \qquad 2.4$$

where η_{EQE} is the external quantum efficiency, which is defined by how efficiently an incident photon gives rise to an electron flowing in the external circuit. In organic solar cells, η_{EQE} depends on: photon absorption, diffusion and dissociation of the exciton, and the transport and collection of charge. N_{ph} (λ) is the photon flux density in the incident AM 1.5G spectrum at wavelength λ and a total intensity of 100 mW cm^{-2}. The upper limit of Jsc is obtained according to Eq. 2.4 by integrating from the high photon energy to the optical band gap of the absorber material. This is due to the photoexcited electron, which can decrease its potential energy by losing energy through phonons until it reaches the lowest lying level in the C_B. Since phonon

energy dissipates into heat, this process is known as thermalization. As a consequence of thermalization, the semiconductor bandgap is often regarded as a measure for the achievable voltage. The higher the bandgap, the higher the voltage can be. Otherwise, low bandgap material can absorb more photons, so the number of photogenerated charge carriers can increase and the photocurrent can increase. The lower the bandgap, the higher the photocurrent. Therefore, there must be an optimal bandgap for a given illumination spectrum. Shockley and Queisser[73] were the first to calculate the maximum power conversion efficiency for a semiconductor with a given bandgap assuming only radiative recombination and solar radiation on earth. They obtained a value of 30 % for a semiconductor with a bandgap of 1.12 eV like Si.

Organic semiconductors have E_g about 2 eV, which lead to efficiencies of around 20 %. However, non-radiative recombination must also be considered for this kind of solar cell[32]. The top limit has been calculated to be around 11%[75]. In theory, to achieve efficiencies between 5 and 10% and lifetimes between 5 and 10 years, this technology would need to be commercialized[76].

3) Open-circuit voltage

The limits of *Voc* in organic solar cells are controversial. They have been attributed to differences in electrical contact work functions and to the difference between the HOMO of the donor and the LUMO of the acceptor. However, when there are recombination losses the real *Voc* value depends on the inverse saturation current J_S of the junction in the dark[78-80]. For a junction and only one conduction mechanism, the relationship between J_S and *Voc* derived from solving the ECD of Fig. 2.12 is given by:

$$Voc = \frac{nk_BT}{q} In\left[\frac{Jsc}{J_S} + 1 - \frac{Voc}{R_{SH}J_S}\right] \qquad 2.5$$

where n is the ideality factor of the junction in the dark and J_S depends on the conduction mechanism.

As we mentioned in chapter 1, the thermodynamic limit of the *Voc* is the difference in the quasi Fermi-levels in the heterojunction. The dependence with the HOMO and LUMO of the donor and acceptor, respectively, is therefore due to whether, for example, the LUMO of the donor increases and the HOMO of the donor decreases. The quasi-Fermi levels (E_{FN} and E_{FP}) that are limited by LUMO and HOMO have the same tendency, so the *Voc* increases. Fig. 2.11 shows the *Voc* limit in a heterojunction.

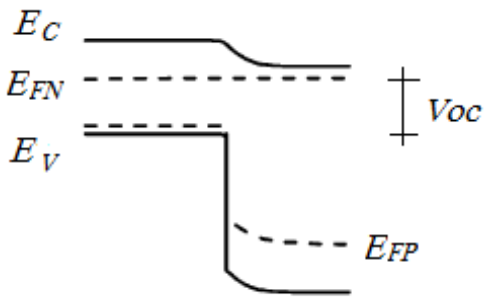

Fig. 2.11 Maximum *Voc* in a heterojunction

This does not mean that the electrical losses in the contacts and in the heterojunction (J_s) can also affect the *Voc* through the 2.5 relationship. It has been found that 2.5 is not totally in agreement with experimental results and, to overcome this drawback, possible effects on the ideality factors have been suggested[79].

2.8 Electrical equivalent circuit diagrams (ECDs)

ECD's are useful for describing the electrical behavior of semiconductor devices. They consist of a network of electrical components such as diodes, current or voltage sources, and resistors.

Ideal solar cells typically are represented by the ECD in Fig. 2.12.

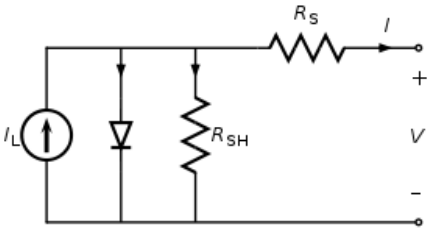

Fig. 2.12 ECD for an ideal solar cell

If R_{SH} is high, the total current under illumination conditions is given by:

$$I = I_L - I_D \tag{2.6}$$

where I_L is the photocurrent and I_D is the diode current ($J_D = J_S \, exp \, [qV/nk_B T]$). For ideal solar cells, I_L is the only light-dependent component, and I_D depends only on the potential. Therefore, the loss mechanisms are commonly attributed to the dark conduction mechanism. However, in non-ideal solar cells such as organic solar cells, the maximum I_L (I_{SC}) is given by 2.4 and, as we mentioned above, this parameter can depend on multiple factors. Therefore, in addition to illumination, I_L can depend on other physical parameters such as electric potential when the collection of charge depends on internal electric fields[81]. The possible dependence of I_L on parameters such as electric potential leads to further losses also for the photocurrent. It has also been reported that R_S, and R_{SH} are also light-dependent[82].

The complexity of the problem requires a systematic approach. Here we analyze the dark transport mechanism in order to detect a possible loss mechanism.

Our group previously showed that the two-diode model in Fig. 2.13 described well the non-ideal dark I-V curves from crystalline silicon/ amorphous silicon heterojunctions[83].

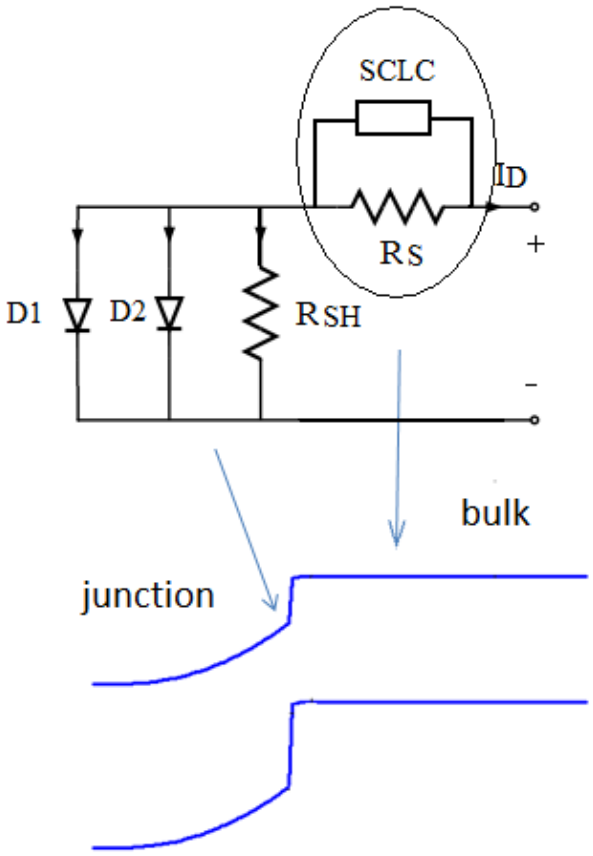

Fig. 2.13: Assignment of ECD elements for an arbitrary heterojunction

R_{SH} is due to recombination of charge carriers near the dissociation site (e.g. the D/A interface). R_S considers conductivity, i.e. the mobility of the specific charge carrier in the respective transport medium: for example, the mobility of holes in a p-type conductor or electrons in an n-type material donor material. Mobility can be affected by space charges and trap sites. R_S is also

increased by a longer traveling distance of the charges in, for example, thicker transport layers or contact resistances. Also considered is the space charge limited current (SCLC) mechanism, which is commonly present in high resistance materials such as organic semiconductors[84]. Diodes can model a specific mechanism occurs at one junction. These diodes are responsible for the nonlinear shape of the I-V curves. Fig. 2.13 shows the elements that are related to each region in one arbitrary device. Note that enclosed elements correspond to the bulk while the others correspond to the junction.

Two diodes are used to check whether two different mechanisms are present in the structure. The behavior of the inverse saturation current in diodes J_S vs temperature depends on the conduction mechanism present in the junction. We can therefore use this method to determine the conduction mechanism.

2.9 Recombination of charge

The highly localized DOS of organic materials lead to non-radiative recombination paths[81]. To identify the conduction mechanism we can localize the region of the device in which the recombination occurs. Fig. 2.14 shows different recombination paths: through the p-n junction interface, through the bulk, or at the electrodes interface.

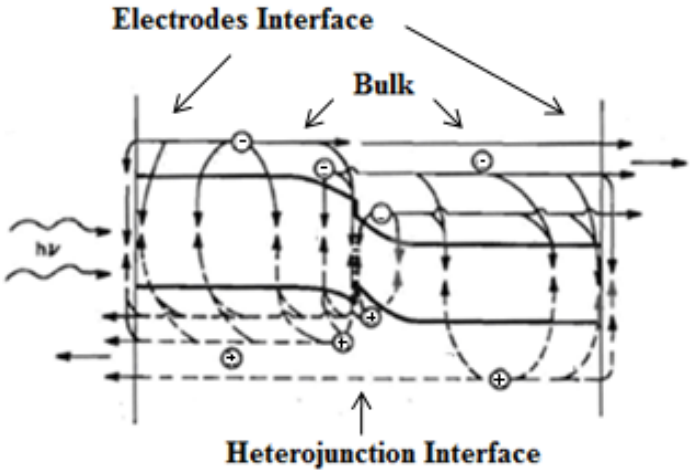

Fig. 2.14: Recombination paths in heterojunctions.

There has recently been an interesting debate about the recombination mechanism in OBHT devices. One side of the debate supports bimolecular mechanisms[85] and the other supports the monomolecular mechanism[81]. In general, recombination transitions to states between quasi Fermi-levels are monomolecular because the occupancy of these states does not depend much on light intensity. This type of recombination is often described as the Shockley-Read-Hall process. Recombination involving states outside the quasi-Fermi energies are generally second order or bimolecular for the opposite reason. From this debate, Street concluded that at high light intensities the bimolecular recombination dominates, while at low intensities monomolecular recombination is the dominant recombination mechanism[86].

2.10 Conduction mechanisms

In general there are four basic physical mechanisms: diffusion, recombination, tunneling, and thermionic emission. Depending on the structure and materials of the device, one or a combination of these mechanisms can occur. Below we present an overview of the most common mechanisms currently found in heterojunctions involving organic materials. Although these mechanisms were initially proposed for inorganic semiconductors, in this thesis we prove the validity of some of them for organic semiconductors.

2.10.1 Diffusion and recombination

The current density in a forward biased p-n junction is generally described by the Shockley equation:

(2.7)

with

$$J_S = \left(\frac{qD_h ni^2}{L_h N_D} + \frac{qD_e ni^2}{L_e N_A} \right) \tag{2.8}$$

where J_S is the inverse saturation current, q is the electron charge, k_B is the Boltzmann constant, T is the absolute temperature, V is the voltage across the p-n junction, n_i is the intrinsic concentration, D is the diffusion coefficient, and L is the diffusion length. The subscripts e and h refer to electrons and holes, respectively, as minority carriers, i.e. holes on the n-side and electrons on the p-side. The above equation (2.7), developed by Shockley, neglects the current component, which is due to recombination in the depletion region.

If we consider the temperature effect in the J_S, since the second part of the equation will behave like the first, and also a p^+n abrupt junction is considered, we can write J_S as[26]:

$$J_S \alpha T^{(3+\gamma/2)} \exp\left(-\frac{Eg}{k_B T} \right) \tag{2.9}$$

The temperature dependence of the term $T^{(3+\gamma/2)}$ is not important in comparison with the exponential term. The slope of a J_S versus $1/k_B T$ plot corresponds to the energy gap E_g.

Considering recombination in the depletion region, the experimental results in general can be represented by the empirical formula:

$$J \alpha \exp(\frac{qV}{nk_B T}) \tag{2.10}$$

where recombination current dominates and the ideality factor *n* becomes 2[26].

2.10.2 Tunneling mechanisms

1) Multituneling capture-emission mechanism (MTCE)

Matsuura et al.[87] proposed the multi-tunneling capture-emission mechanism illustrated in Fig. 2.15.

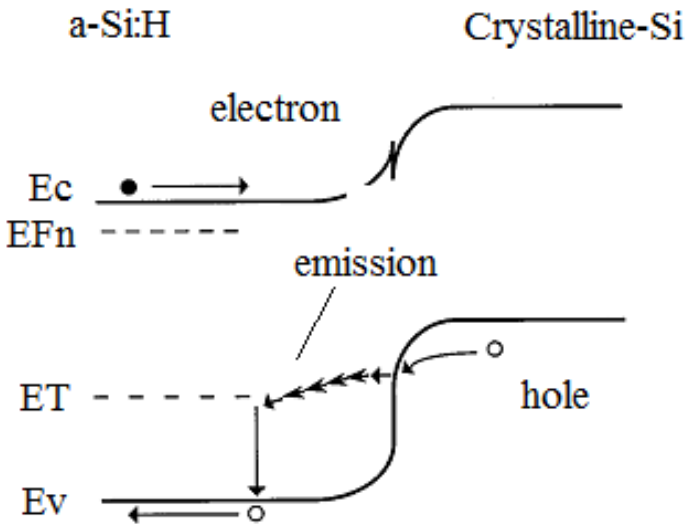

Fig.2.15: Scheme of tunneling conductions mechanisms.

A hole in the valence band of c-Si flows from one localized state to another in the a-Si:H within an energy range of k_BT by a multistep-tunneling process and keeps flowing until the tunneling rate becomes smaller than the rate of hole release from the localized state to the valence band of the a-Si:H, or until recombination of the hole with an electron in the conduction band of the a-Si:H.

The current density flowing from the crystalline semiconductor to the amorphous semiconductor is therefore given by:

$$J = J_S\left[\exp(A \cdot V) - 1\right] \tag{2.11}$$

where

$$A = \frac{1}{nk_BT} \tag{2.9}$$

and

$$J_S = B\sigma_n V_{th} N_c \exp\left(-\frac{E_C - E_T}{k_BT}\right) + B.\sigma_p V_{th} N_V \exp\left(-\frac{E_F - E_V}{k_BT}\right) \tag{2.12}$$

where B is a constant independent of the voltage and temperature, σ_n and σ_p are the capture cross section of electrons and holes, respectively, v_{th} is the thermal velocity, and k_BT is the thermal energy. The first term in Eq. 16 represents the emission of electrons from a localized state E_T to the E_V. The second term represents the capture of holes from the E_C in the Fermi level, E_F.

2) Tunneling-enhanced recombination mechanism (TEIR).

Rau et al[88] developed a model in which the recombination process is enhanced by tunneling and the reverse saturation current is given by J_S *α exp (- Ea/nk$_B$T)*, where *Ea* is an activation energy. According to this model, in the case of the tunneling-enhanced recombination mechanism in the space region of one of the active materials, *Ea* is related to the band gap energy of the material. On the other hand, for the tunneling-enhanced interface recombination mechanism (TEIR), *Ea* is equal to the effective barrier height for the interface (*Φb*).

2.10.3 Space charge affected by traps

The comparatively low charge carrier mobility in most organic semiconductors as well as the need to drive high currents through the device can lead to the accumulation of charges in the semiconductor bulk. These excess charges build up a space charge that creates a field which reduces the throughput, i.e. increases the transit time of charges between the device electrodes. This phenomenon is termed space charge limited current (SCLC).

Provided there are no traps, the total current through a semiconductor considering space charge formation as a function of voltage can be expressed as [84,90]:

$$I = qp\mu\frac{V}{d} + \frac{9}{8}\varepsilon\mu\frac{V^2}{d^3} \tag{2.13}$$

where p is the density of the thermally generated free carriers, μ is the mobility, d is the semiconductor thickness, and ε is the semiconductor dielectric constant.

As long as the density of the thermally generated free carriers p is dominant, the current follows Ohm's law. Otherwise, the current increases with the square of the voltage according to the second term in Eq. 2.13. This second term is known as the Mott and Gurney equation for trap free space charge limited currents. The transition from ohmic to space charge conduction here is very smooth. If the material contains shallow traps, the residence time inside the traps is shorter than the charge carrier transit time. The space charge then comprises the mobile free carriers and those that are thermally free from the shallow traps. When trap states exist in the studied material, the exponent of voltage in the second term of Ec. 2.13 increases and we can

rewrite this term in a more general form as: $k_B V^m$, where k_B is a constant. This form will be used in the next chapter.

2.10.4 Thermionic emission

There are two distinguishing mechanisms for charge carriers that overcome barriers: thermionic emission and quantum mechanical tunneling (field emission). For thermionic emission over a triangular barrier of height ϕ from a metal into a high-mobility semiconductor, the current density is given by:

$$J = AT^2 \exp^{\left(\frac{-\phi}{k_B T}\right)} \cdot (\exp^{\frac{qV}{k_B T}} - 1) \tag{2.14}$$

where A is the effective Richardson constant and T is the absolute temperature.

If an electric field E is applied across the barrier, the barrier height can decrease by

$$\Delta\phi = \sqrt{\frac{q^3 E}{4\pi\varepsilon_o}} \tag{2.15}$$

where q is the elementary charge and ε_o is the dielectric constant of vacuum.

In a semiconductor with a low mobility, it is necessary to take into account the diffusion of carriers within the barrier region back towards the contact. The analysis is strongly dependent on the type of barrier assumed. A full treatment is given by Kao and Hwang[89] . At sufficiently low temperatures, or for large barriers at high fields, emission due to quantum mechanical tunneling through the barrier (field emission) can be important.

Table 2.1 summarizes the basic conduction mechanisms. J_S vs T, and the ideality factor are indicated for each mechanism.

TRANSPORT MECHANISM	J_S	n	Ref
Diffusion	$J_S \alpha exp(-Eg/k_BT)$	$n = 1$	26
Recombination	$J_S \alpha exp(-Eg/2k_BT)$	$n \leq 2$	26
Tunneling	$J_S \alpha exp(-Ea/k_BT)$	$n \neq$ cte.	87
Thermionic emission	$J_S \alpha [exp(-\Phi_B/k_BT)]kT^2$	$n = 1$	89
TEIR	$J_S \alpha exp(-Ea/nk_B T)$	$n \neq$ cte.	88

Table 2.1 J_S and n for the main conduction mechanism in heterojunctions

In all cases, the exponential term of J_S has the same dependence with temperature, and Eg, Ea, or Φ are potential energies that can be calculated from the slope of a typical Arrhenius plot. Therefore, once this potential energy is calculated and the ideality factor is known, we can determine the transport mechanism in the heterojunction. The dependence on the voltage is the same for all the transport mechanisms listed in the table.

Fig. 2.16 shows a typical non-ideal semilog I-V curve. The curve is non-ideal because the transport can be affected by additional recombination mechanisms, e.g. recombination through DOS at a low-voltage region. Such non-ideal curves commonly show exponential dependence in low- and medium-voltage regions, while at relatively high voltages bulk mechanisms such as ohmic and SCLC effects are responsible for the behavior of the current. Therefore, to determine which transport mechanism dominates at each region, the physical parameters n and J_L can be extracted at each region (low- and medium-voltage regions). The value of n and the temperature dependence of J_L, which are represented in Table 2.1, are useful for determining the corresponding physical mechanism.

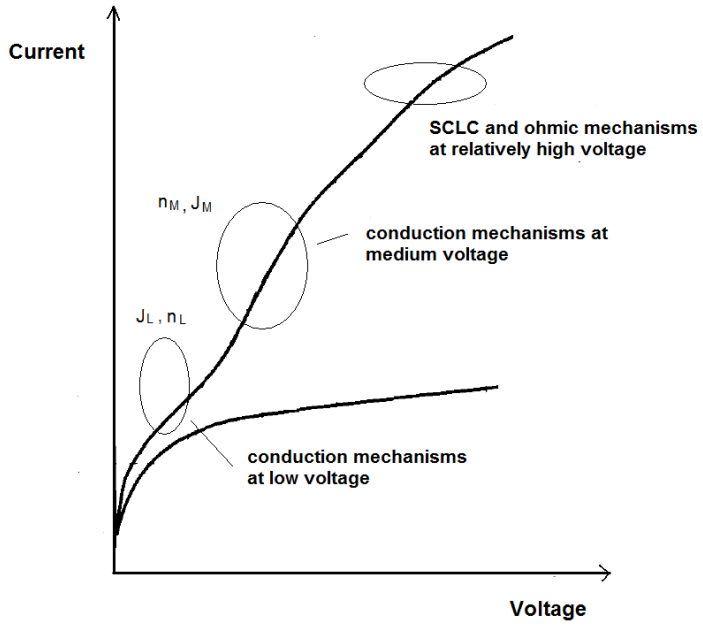

Fig. 2.16 Non-ideal Semilog I-V curve.

2.11 Capacitance voltage characteristics

Capacitance voltage characteristics are useful for determining fundamental parameters in heterojunctions such as charge carrier concentrations and dielectric constants.

Fig. 2.17 shows the basis of this technique. A small signal of AC (ΔV) superimposed onto a DC component (V) is applied to the sample. This change in potential increases the space of the charge and, therefore, the capacitance. This differential capacitance can be measured at different DC potentials in order to obtain the capacitance voltage characteristic.

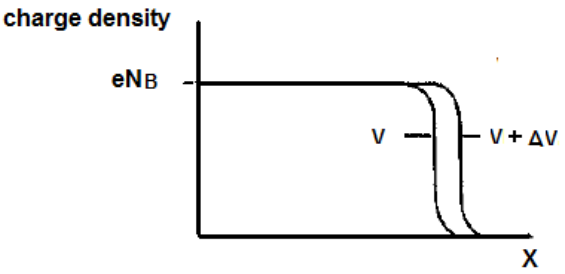

Fig. 2.17 Increase in space of charge by a differential of potential ΔV

If the charge density is constant through the space and one side of the heterojunction has a charge density that is higher than the other, the capacitance voltage characteristic can be approximated by[26]

$$\frac{A^2}{C^2} = \frac{2}{q\varepsilon_s N_B}(V - V_{bi}) \qquad (2.16)$$

where ε_s is the relative dielectric constant and N_B is the charge carrier concentration of the material with less carrier concentration. V_{bi} is the built-in potential in the heterojunction. Fig. 2.18 shows a typical $1/C^2$ vs V characteristic. According to Ec. 2.16, the intercept of the curve with the voltage axis corresponds to V_{bi}, and the product $\varepsilon_s N_B$ can be calculated from the intercept with the capacitance axis.

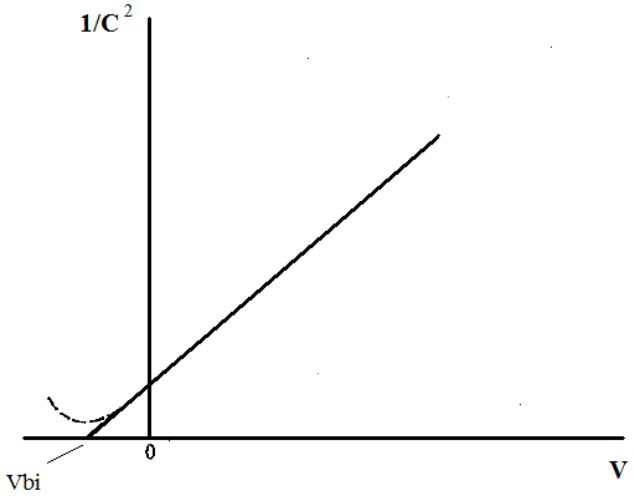

Fig. 2.18 Typical $1/C^2$ vs V characteristic

Chapter 3

Chapter 3

P3HT/Si hybrid solar cell

In this chapter the fabrication and characterization of P3HT/Si are summarized. The dark current density-voltage measurements at different temperature were modeled using a two diode equivalent circuit. When the method is applied to organic/inorganic solar cells, it allows us not only to determine the limiting conduction mechanisms of P3HT/Si diodes but also to calculate some physical parameters such as the electron affinity, the carrier concentration, and the width of the exponential density of states of the P3HT. Additionally, the energy band diagram of the heterojunction is proposed. Finally, the potential partition and capacitance voltage curves of the device are shown.

3.1 Illuminated I-V characteristics

One of the most popular polymers used for organic solar cells is an alkylthiophene derivative, P3HT (Poly (3-hexylthiophene)) which has provided mobility values as high as 0,1 cm^2/Vs[91] and optical absorption coefficient in the visible spectra in the order of 10^5 cm^{-1}.An organic-inorganic hybrid structure consisting of an Au/P3HT/n-type crystalline silicon/Al structure was prepared in the CINVESTAV in México. The fabrication process is indicated in Appendix A.

Fig. 3.1a shows the illuminated current-voltage characteristic of the device with the best performance. The solar cell parameters obtained were V_{OC} = 0.47 V, FF = 0.37 and J_{SC} = 7.44 mA/cm^2 under 100 mW/cm^2 illumination. The conversion efficiency of the heterojuntion was 1.27 %. The effective area was S_A = 0.07 cm^2. The illuminated current-voltage measurements were performed using Oriel 250 W Xenon lamp with the appropriate Oriel filters to simulate the 1.5 AM solar spectrum. This experimental setup is showed in Appendix B. It was remarkable the repeatability obtained for different devices in the same substrate.

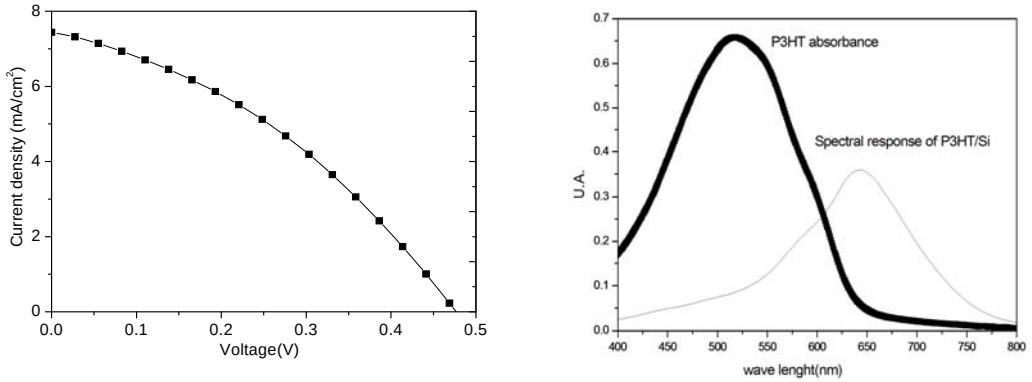

a) b)

Fig. 3.1: a) Illuminated I-V characteristics; b) Absorbance and spectral response of the n-c-Si/p-P3HT solar cell.

Fig. 3.1b shows P3HT absorbance measurements and spectral response of n-c-Si/p-P3HT solar cell. As can be observed, more than half of the spectral response spectrum is outside the P3HT absorbance, therefore we can say that most of the photocurrent is generated by Silicon.

3.2 Dark I-V curves at different temperatures

The current-voltage-temperature (I-V-T) measurements were performed using an HP4145B semiconductor parameter analyzer and K-20 temperature controller. The system is also showed in Appendix B.

Fig. 3.2 shows the dark current-voltage characteristics of the diodes measured at ± 2 V for temperatures between 300 and 360 K. A rectification factor of 10^2 was obtained at ± 1 V.

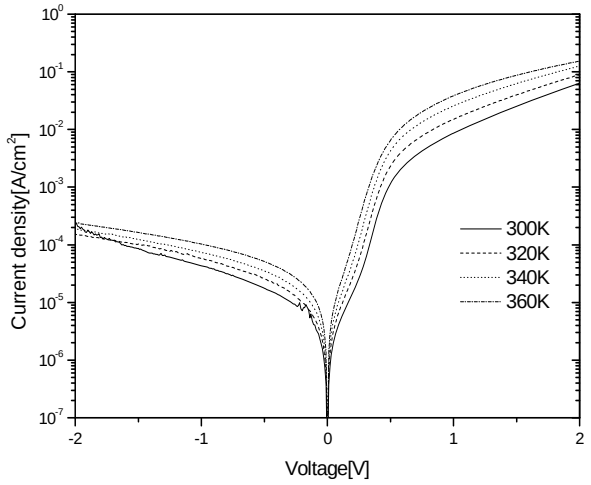

Fig. 3.2: Dark I-V characteristics of the n-c-Si/p-P3HT at different temperatures.

Note that different regions can be defined depending on the applied voltage, *V*. First, the current is limited by shunt mechanisms in the reverse region. Second, the current increases exponentially with the applied voltage in the low forward region (L, $0.1 < V\,(\mathrm{V}) < 0.3$) and in the medium forward region (M, $0.3 < V\,(\mathrm{V}) < 0.5$) but with different slopes. And third, the high forward

region (V > 0.5 V) where the current increases more slowly. It can be observed also in Fig. 3.3a.

3.3 Parameters extraction

In order to study hybrid structures using double diode model of Fig. 2.13, the set of equations to solve are:

$$V_D = V_J + V_B$$

$$J_D = J_{RS} + J_{SCLC} = \frac{V_B}{S_A R_S} + kV_B{}^m$$

$$J_D = J_{DL} + J_{DM} + J_{RSH} = \sum_{i=L,M} J_{Si}\{\exp(A_i V_J) - 1\} + \frac{V_J}{S_A R_{SH}} \qquad (3.1)$$

where J_{DL} and J_{DM} are the current densities of two ideal diodes, one for the low voltage region (L) and other for the medium voltage region (M), with their respective reverse saturation current densities (J_{SL}, J_{SM}) and exponential factors (A_L, A_M). R_S and R_{SH} are the series and shunt resistances, respectively. The J_{SCLC} is the current density due to the Space Charge Limited Current mechanism, defined by the parameters k and m. V_B and V_J are the voltage drop across the bulk and the voltage drop across the junction, respectively. Eight circuit model parameters (J_{SL}, A_L, J_{SM}, A_M, R_S, k, m *and* R_{SH}) are extracted using a numerical method and assign the parameters manually[83].

Fig. 3.3a shows the fitting of the measured I-V characteristics at 300 K and the contribution of each conduction term (J_{RSH}, J_{DL}, J_{DM} *and* J_{RS}) to the total current density. Table 3.1 shows the values of the eight fitting parameters and the ratio J_{SCLC}/J_{RS} at 1.5 V. The I-V derivate also is shown in Fig. 3.5b. This derivate is useful to get a good accuracy in the fitting.

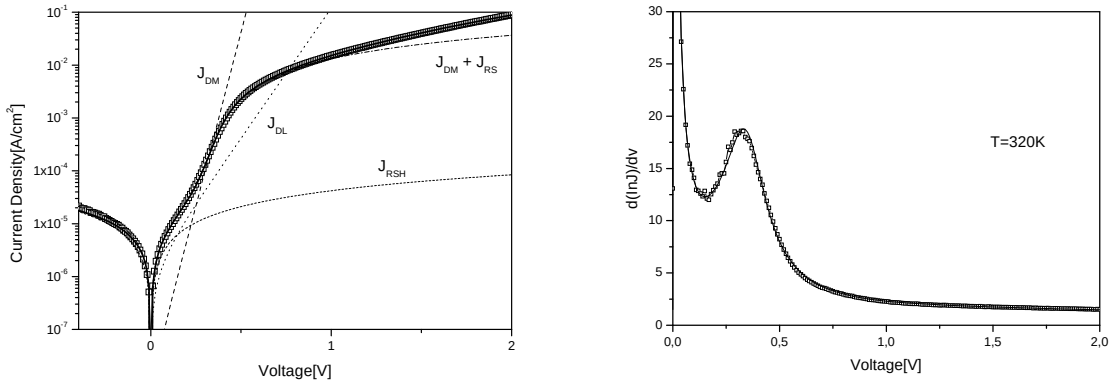

a) b)

Fig. 3.3: Experimental (symbols) dark current-voltage characteristics at 320k, a)the contribution of each conduction mechanism is shown separately and b) its derivate.

Fig. 3.3a also shows the current density contribution of the different conduction mechanism to the total current at 320K. The plot demonstrates that there some regions where the total current is not dominated by a particular conduction mechanism.

Because the ratio J_{SCLC}/J_{RS} has a value between 1 and 2 for all the studied temperatures, both mechanisms must be considered in the total current.

T (K)	A_L (V^{-1})	J_{SL} ($\mu A \cdot cm^{-2}$)	A_M (V^{-1})	J_{SM} ($nA \cdot cm^{-2}$)	R_S (Ω)	R_{SH} ($k\Omega$)	k ($Acm^{-2}V^{-m}$)	m	J_{RS}/J_{SCLC} @ 1.5 V
300	15.2	0.37	37.9	0.14	1060	400	$0.83x10^{-4}$	3.27	1.16
320	16.2	0.71	35.9	0.86	590	290	$1.15x10^{-3}$	3.12	1.47
340	16.3	1.36	33.5	6.43	360	220	$1.50x10^{-3}$	3.00	1.78
360	17.2	2.30	30.1	54.30	265	150	$1.90x10^{-3}$	2.89	1.92

Table 3.1. Values of the parameters used to fit the experimental data and the ratio J_{SCLC}/J_{RS} at 1.5V.

The procedure to get a good fitting can be summarized as:

1) Use the less number of components as possible. Sometimes it is not necessary use two diodes or SCLC element. The necessity of a second

diode can be cheeked on semilog I-V curve, it is when two slopes are observed, in the case that it cannot be observed easily due to shunt resistance contribution, it should be start with one diode.

2) Assign the values of electrical resistances. These values can be estimated by the slope of the I-V curve at low voltage linear region to the shunt resistance and the linear region after the elbow to series resistance.

3) Fit the values for diode at medium voltage region.

4) Fit the values for diode at low voltage region. In case of use two diodes, there is a region where both diodes contribute to current, so the second diode fitting must be iteratively with the first one.

5) Fit the SCLC element. Although typically this element is not important at voltage region where the solar cells deliver energy. It is useful to study the bulk properties in the active materials, e.g. the trap states.

3.4 Conduction mechanisms

We use the temperature dependence of the equivalent circuit parameters to discuss the conduction mechanisms that may be responsible for the device behavior. We considered ohmic contacts in the interface Al-Si and P3HT-Au[92], so the two diodes physically represent two conduction mechanisms in the same junction. Fig. 3.4 shows the thermal dependence of the exponential factor and the reverse saturation current density for the low voltage region, A_L and J_{SL} in Eq. 3.1 respectively.

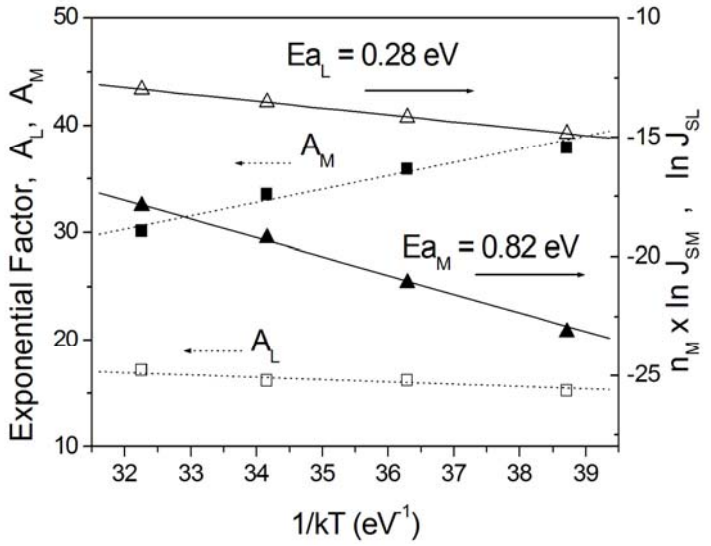

Fig. 3.4: Temperature dependence of the exponential term (A, square) and the reverse saturation current density (J_S, star) for low voltages (A_L, J_{SL}, empty symbols) and medium voltages (A_M, J_{SM}, full symbols).

Because factor A_L is weakly dependent on temperature we conclude that a tunneling mechanism is limiting the total current in this region. In addition, because factor J_{SL} varies exponentially with $1/T$ we assume that a multitunneling capture-emission (MTCE) is the limiting conduction mechanism at low voltages. From the MTCE model, the reverse saturation current is given by Eq. 2.12.

Assuming that electrons are injected from the silicon into the P3HT, and that in P3HT $(E_F\text{-}E_V) < (E_C\text{-}E_T)$, the activation energy of 0.28 eV calculated from the slope of the reverse saturation current behavior in Fig. 3.4 corresponds to the Fermi level $(E_F\text{-}E_V)$ of the P3HT so the second term in Eq. 2.10 is predominant. To corroborate this hypothesis, we calculated the dark carrier concentration of the P3HT to be $N_{P3HT} = 2\times10^{16}$ cm^{-3}, using an effective density of states of $N_V = 1\times10^{21}$ cm^{-3}. The value obtained for the carrier concentration is in good agreement with the values reported in literature for the P3HT using thin film transistor configuration[93].

Fig. 3.4 also shows the thermal dependence of the exponential factors for the medium voltage region , A_M in Ec. 3.1. Since the ideality factor, given by $n_M A_M k_B T = 1$, is around 1 for all temperatures and factor A_M is not constant, diffusion can be responsible of its behavior. In order to prove the conduction mechanism the activation energy from an Arrhenius plot is usually calculated. But in our case, the calculated value from J_{SM} on $1/k_B T$ plot is 0.92 eV, which does not corresponds to E_{gP3HT} = 1.80 eV[11]. In an alternative recombination model the activation energy E_{aM} is calculated by a modified Arrhenius plot using[88]

$$J_{SM} = J_{0M} \exp\left(\frac{-E_{aM}}{n_M k_B T}\right) \tag{3.2}$$

where J_{0M} is a weakly temperature-dependent prefactor and n_M is the ideality factor. As was explained in previous chapter, in the case of neutral bulk (diffusion process) and space charge region recombination, E_{aM} is related to the band gap energy of the absorber material whereas for interface recombination, E_{aM} is the effective barrier height at which charge carriers from the P3HT recombine at the interface, Φ_b. Since we obtained a value of E_{aM} = 0.82 eV from the slope of the modified Arrhenius plot in Fig. 3.4, which is a long way from the P3HT band-gap energy, we consider that the current observed in the medium voltage region is due to a tunneling-enhanced recombination mechanism with a characteristic potential barrier $\Phi_B = E_{aM} = 0.82$ eV.

It was observed that for different samples with worse performance, the same kind of tunneling mechanisms are present, but the J_S and n commonly increase, i.e structure reported in ref 94.

Finally, the high applied voltage region ($V > 0.6$ V) is limited by SCLC and series resistance. For the studied range of temperatures, the factor m is

around 2, the ideal value for SCLC. Fig. 3.5 shows the thermal dependence of the *K* and *Rs* factors.

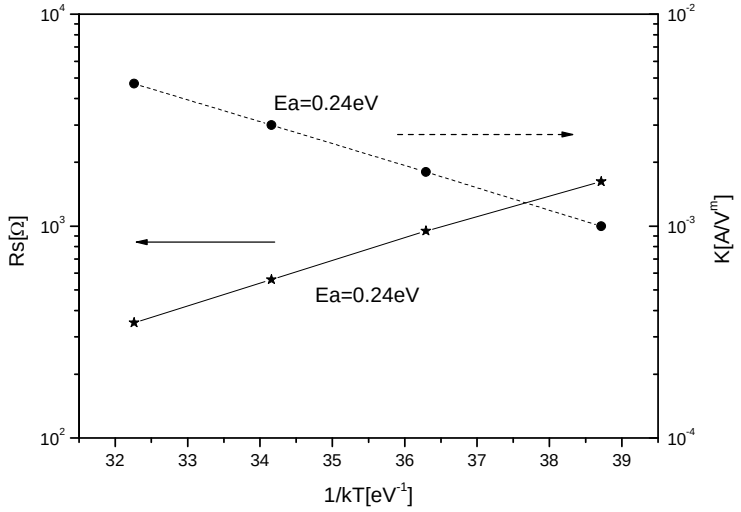

Fig. 3.5: Temperature dependence of *K* and *Rs*.

The factor *K* presents a thermally activated behavior, and also follows the equation 3.1. If we calculate the slope of the curve, we get the activation energy value of 0.24 eV, which is similar to the polymer Fermi level (E_F-E_V) previously calculated. As can be observed R_S has the same activation energy. Both mechanism are in parallel and represent the bulk properties. As both have an activation energy similar to the P3HT Fermi level we can say that the polymer is the layer that limits the conduction at high voltages by means of SCLC and ohmic mechanisms.

3.5 Extraction of P3HT properties and energy band diagram at the heterojuntion.

Fig. 3.6 shows the proposed energy-band diagram for the c-Si/P3HT p/n structure. From the Anderson's model the P3HT electron affinity (χ_{P3HT}) is given by[95]:

$$\chi_{P3HT} = qVd_{Si} + qVd_{P3HT} + \chi_{Si} + \delta_{Si} - Eg_{P3HT} + \delta_{P3HT} \quad (3.3)$$

where χ_{Si} = 4.05 eV is the electron affinity of silicon[26], $\delta_{Si} = k_B T \times \ln(N_C/N_{Si})$ = 0.11 eV is the difference between the conduction band and the silicon Fermi level, and Eg_{P3HT} = 1.80 eV is the P3HT band gap[96].

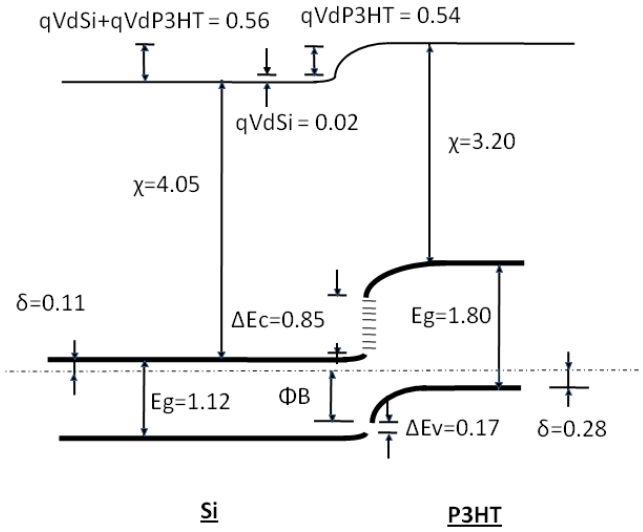

Fig. 3.6: Proposed energy-band diagram for n c-Si/ P3HT. Units in eV.

Previously we obtained the difference between the P3HT valence band and the Fermi level, $\delta_{P3HT} = E_F - E_V$ = 0.28 eV. In addition, the value of the P3HT built-in potential is the difference between the potential barrier and the position of the Fermi level, $qVd_{P3HT} = \Phi_B - \delta_{P3HT}$ = 0.82-0.28 = 0.54 eV. The Si built-in potential, qVd_{Si} = 0.02 eV, can be calculated from the values of the doping levels (N_{Si}, N_{P3HT}) and the dielectric constant, ε_{Si} = 11.8[26] and ε_{P3HT} = 6.5[96], using $qVd_{Si}/\ qVd_{P3HT} = N_{P3HT}\ \varepsilon_{P3HT}/\ N_{Si}\ \varepsilon_{Si}$. Finally, from Eq. 3.4 the electron affinity of P3HT obtained in our case was χ_{P3HT} = 3.2 eV, which is equal to the reported value in Ref 97 by applying optical methods.

To get the complete band diagram, the conduction band offset and valence band offset were ΔE_c = 0.85 eV and ΔE_v = 0.17 eV, respectively. They were calculated using

$$\Delta E_C = Eg_{P3HT} - qVd_{Si} - qVd_{P3HT} - \delta_{Si} - \delta_{P3HT} = Eg_{P3HT} - Eg_{Si} + \Delta E_V \qquad (3.4)$$

The temperature characteristic of the shallow density of traps can be calculated from the behavior of the parameter *m* vs temperature SCLC mechanism. The values shown in Table I for *m* in Eq. 3.1 follow the Rose model[98]:

$$m = \frac{T_T}{T} + 1 \qquad (3.5)$$

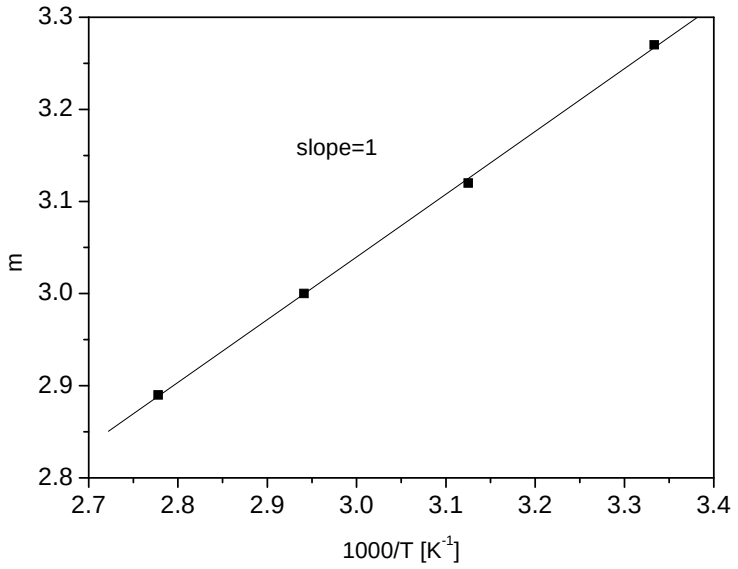

Fig. 3.7 Temperature dependence of m parameter

where T_T is the characteristic temperature of the exponential trap distribution. Because of the obtained values for carrier concentration and activation energy in P3HT, 2×10^{16} cm^{-3} and 0.28 eV respectively, exponential instead Gaussian distribution of the density of states can be assumed as proposed in ref 80. From the slope of Eq. 3.7, a value of T_T = 681 K is obtained. The typical values in PTFTs are around 450 K[99,100]. The increase in the calculated value of T_T could be due not only to the increment in the amorphicity of the

P3HT layer since it was deposited on a silicon hydrophobic surface, previously treated with HF, but also to the fact that this value was obtained from the diode structure whereas the previously reported values were obtained from the PTFT structure.

3.6 Junction and bulk voltage variations

The analysis of the compact equivalent circuit made it possible to calculate which part of the applied voltage (V_D) falls across the junction (V_J) and which part falls in the bulk (V_B). Fig. 3.8 shows that the reverse and low forward voltage drop in the bulk is negligible so, in this region, the current-voltage characteristics are junction controlled. On the other hand, at medium and high forward voltages, the voltage drop in the bulk is considerable and the characteristics are bulk controlled. It should be pointed out that the voltage value at which bulk effects start to be non-negligible is similar to the measured open-circuit voltage *Voc*, which is equal to 0.47 V.

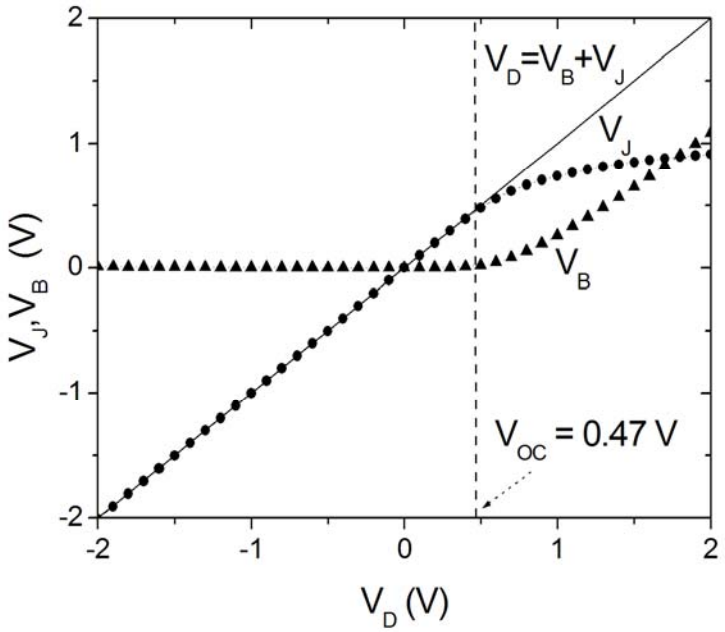

Fig. 3.8: Junction (V_J) and bulk (V_B) voltage variations with applied voltage (V_D). The measured open-circuit voltage is also shown.

3.7 Summary of results

Au/ P3HT (poly [3-hexylthiophene])/n-type crystalline silicon (n-c-Si)/Al heterojuntion solar cells were fabricated and characterized. The solar cell characteristics under illumination reported *Voc* = 0.47 V and *Jsc* = 0.52 mA/cm^2. The better conversion efficiency of this structure was 1.29 %.

We obtained some of the physical parameters of the P3HT layer from the analysis of the dark current-voltage characteristics of P3HT/n-type crystalline silicon solar cells. In particular, a charge concentration value of N_{P3HT} = 2×10^{16} cm^{-3}, an electron affinity value of χ_{P3HT} = 3.2 eV and a characteristic temperature of the exponential trap distribution value of T_T = 681 K. These values are in good agreement with those obtained by other electrical and optical calculation methods. In order to fit the experimental data we used a two diode equivalent circuit. From the temperature dependence of the parameters in the equivalent circuit we obtained the limiting conduction mechanisms of the P3HT/c-Si diode. At low forward bias the current is limited by multi-tunneling capture emission. At medium forward bias the current is limited by tunneling-enhanced recombination. Both mechanisms are related with hopping between localized states at the P3HT/Silicon interface region. At high voltages region the current is limited by series resistance and space-charge limited mechanisms whereas at reverse voltages the current is limited by shunt resistance. Using the values obtained for the P3HT parameters, we propose a band diagram for the structure. Finally, we observed that the measured value of the *Voc* of the P3HT/Si solar cell is similar to the applied voltage at which the bulk effects start to be non-negligible in the P3HT/Si diode.

Chapter 4

Chapter 4

Pentacene/C_{60} solar cell

In this chapter the conduction mechanisms of Pentacene (Pc)/C_{60} solar cells were determined, using the methodoly previously applied in chapter 3. Additionally, capacitance voltage (C-V) characteristics were modeled. The assumptions of applied models were validated by simulations. Finally the effect of the C_{60} film thickness was investigated using experiments and energy band diagram simulations.

4.1 Illuminated I-V characteristics

Pentacene (Pc) / C_{60} bilayer solar cells have emerged as promising photovoltaic devices because of the good conductivity of both donor and electron materials[101]. The first investigations into the Pc/C_{60} system focused on the effects that variations in the fabrication process have on overall efficiency, more specifically, variations in annealing[102,103], degradation[104,105], evaporation conditions[106] and the exciton blocking layer thickness[79]. More recent investigations have focused on the basic working principles of this structure. In particular, the origin of the open circuit voltage was studied using dark current voltage characteristics[79,80]. The charge collection has also been investigated using optical transfer matrix theory[101,104].

Fig. 4.1 shows the scheme of one substrate with four solar cell (x1… x4). These devices were fabricated at ICIQ and the fabrication process is indicate in Appendix A

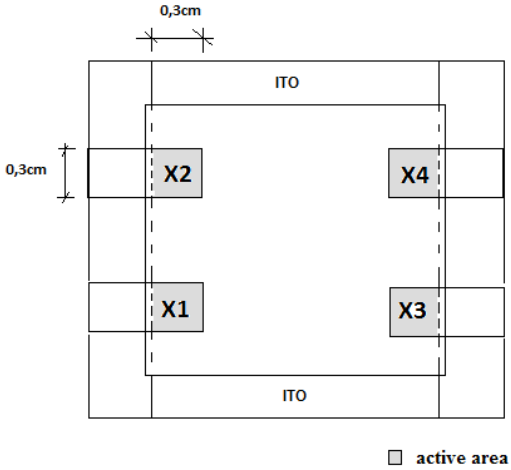

Fig. 4.1: Scheme of one substrate with four solar cells. The active correspond to the fill area.

The light current-voltage measurements were performed using the equipment previously used for P3HT/Si solar cells. The solar cell parameters

at 1000 W/m^2 were: an open-circuit voltage of 0.45 V, a fill factor of 59% and a short-circuit current density of 5.73 mA/cm^2. The efficiency was 1.5%.

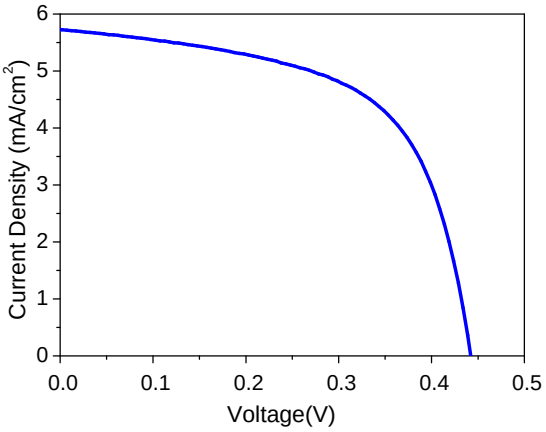

Fig. 4.2: Illuminated current density-voltage characteristics of the Pc/C_{60} solar cell.

4.2 Conduction mechanisms

We used an electrical circuit to model the measured I-V-T characteristics[83]. Fig. 4.3 shows the experimental and modeled curves at different temperatures.

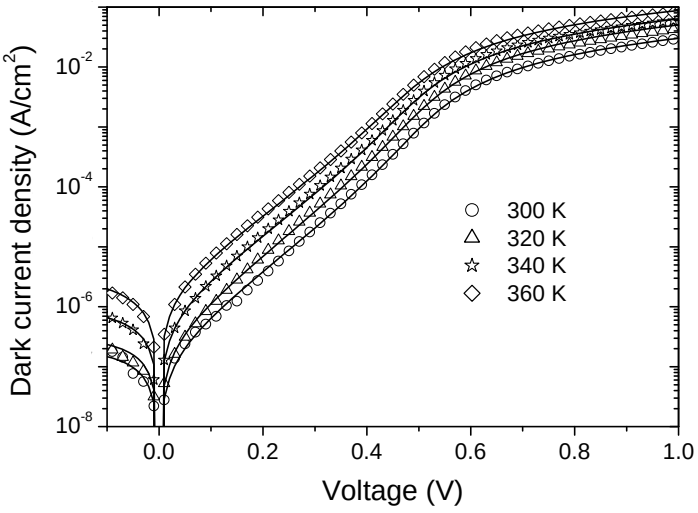

Fig. 4.3: Experimental (symbols) and fitted (solid line) dark I-V-T characteristics of the Pc/C_{60} solar cell.

In the analyzed range of voltage (- 0.1 V < V < 1 V), the model takes into account two diodes (J_L, J_M), a series resistance R_S, and a shunt resistance R_{SH}. The subscript L was used for low voltage regions (0 V < V < 0.3 V) and M was used for medium voltage regions (0.3 V < V < 0.6 V). Fig. 4.4 shows the current contribution of each diode. We assumed ohmic contacts at both the ITO/Pc and C_{60}/Bathocuproine/Al interfaces[107], so as in the P3HT/Si structure; the two diodes in this model physically represent two different conduction mechanisms in the same heterojunction. The exponential behavior of each diode is described using the ideality factor n, and reverse saturation current J_S. The fitting of the dark I-V-T values is also shown in Fig. 4.4 (solid lines). The fitting shows that the calculated R_{SH} value is greater than 150 MΩ at 300K and that it decreases when the temperature increases to 1.2 MΩ at 360 K. Similarly, the R_S value is 148 Ω at 300 K and decreases when the temperature increases to 55 Ω at 360 K.

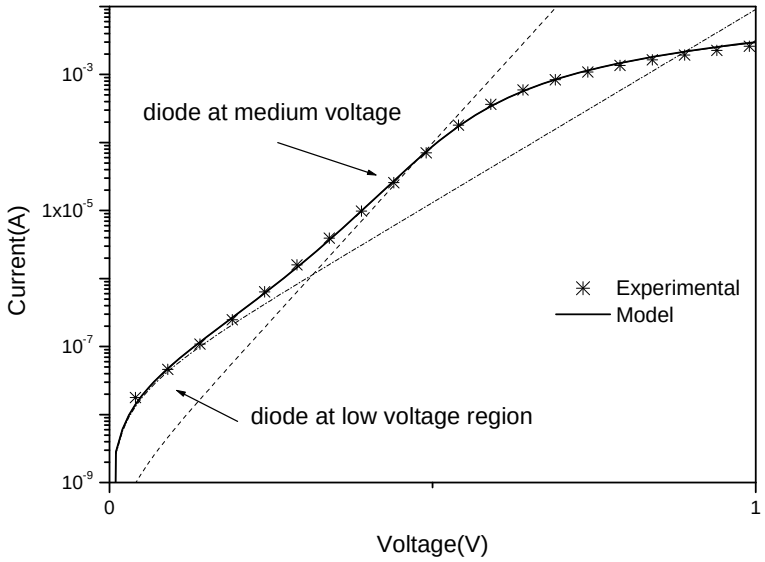

Fig. 4.4: Experimental (symbols) and fitted (solid line) dark I-V-T characteristics of the Pc/C_{60} solar cell.

Fig. 4.5 shows the temperature dependence of the ideality factors and saturation currents for the low and medium regions. Because the ideality factor values are within the range of $1 < n < 2$, we assume that the recombination mechanism is largely responsible for the behavior of the transport mechanism. As it was explained in chapter 2 , for $n = 1$ the activation energy calculated from an Arrhenius plot is the energy gap of the material, while for $n = 2$ the activation energy is half the energy gap of the material. In the present case, the activation energies calculated using J_S vs $1/k_BT$ plots are 0.35 eV and 0.16 eV for medium and low voltages, respectively. Because these values are different from the band-gap and half the band-gap energies (Eg_{Pc} = 2.05 eV and Eg_{C60}= 2.65 eV), we discard the diffusion and recombination mechanism (see Table 2.1).

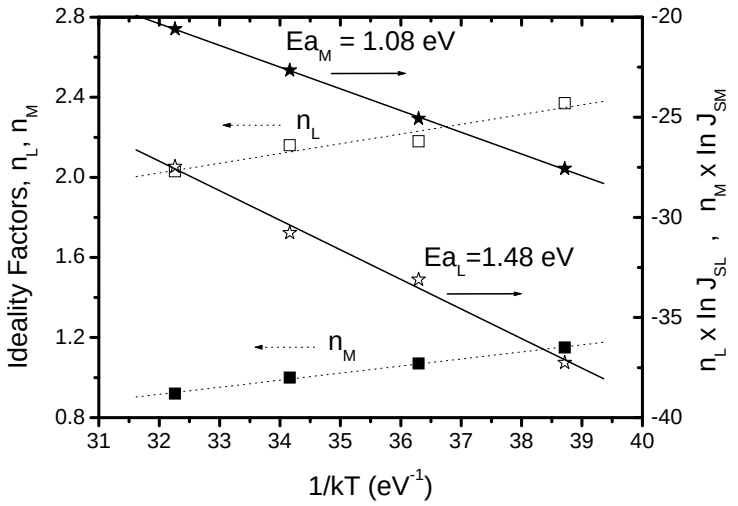

Fig. 4.5: Temperature dependence of the ideality factor (n, square) and the modified reverse saturation current density ($n\ x\ In\ J_S$) for low voltages (empty symbols) and medium voltages (full symbols).

Fig. 4.5 also shows the modified Arrhenius plot, using tunneling-enhanced interface recombination model (Ec. 3.2), leading to activation energy values of E_{aM} = 1.08 eV and E_{aL} = 1.48 eV for the medium and the low voltage region, respectively. Because these energies are significantly different from the Pc and C_{60} band-gap energies, we consider they correspond to the barrier heights at the interface between Pc and C_{60}, $E_{aL} = \Phi_{bL}$, $E_{aM} = \Phi_{bM}$. Therefore, we conclude that the conduction mechanism limiting the dark current of the Pc/C_{60} heterojunction solar cell at low and medium voltage is tunneling-enhanced interface recombination. It should be pointed out that the expression of J_S used by Potscavage et. al.[79] and Li et al.[80] is equivalent to the expression of J_S used here.

Fig. 4.6 shows Arrhenius plot of series resistance, leading activation energy of 0.12 eV. If it is assumed that this activation energy correspond to a Fermi level of one of the active materials, we can calculate the charge carrier density using Ec. 1,2, assuming a density of states of $1x10^{21}/cm^{-3}$ for organic materials. The calculated charge concentration is around $1 \times 10^{19}/cm^{-3}$. Such value is similar to the charge carrier concentration of Pc, calculated later using capacitance-voltage characteristics of the solar cells. Therefore we can say that after medium voltage region ($V > 0.6$ V) the Pentacene is limiting the conduction at dark conditions.

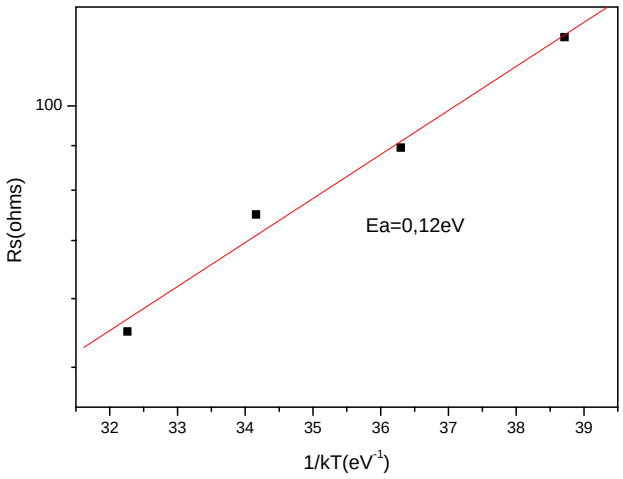

Fig. 4.6: Arrhenius plot of R_S for Pc/C60 solar cell

It should be pointed that the same method to calculated conduction mechanism applied to a device with worse performance result in tuneling mechanism however the values of n and J_S increases, and only one diode ECD model was used.

4.3 C-V modeling and simulation

Fig. 4.7 shows the $1/C^2$ vs V experimental curve (symbols). Two different regions were considered: region I, for low reverse voltages (V > - 0.25 V), and region II, for high reverse voltages (-0.9 V > V > -2.0 V). There are two different regions because one of the materials is fully depleted of free charge carriers[108]. From region I, the effective doping concentration of the C_{60} layer, N_{C60}, can be calculated if we assume that its value is much lower than the effective doping concentration of the Pc layer, N_{Pc}. We used the typical relationship of an abrupt junction[26], previously explained in chapter 2 and rewrite here for the studied heterojunction:

$$\left(\frac{A}{C}\right)^2 = \frac{2(V - V_{bi})}{q\varepsilon_0\varepsilon_{C60}N_{C60}} \tag{4.1}$$

where q is the electronic charge, ε_0 is the vacuum permittivity, $\varepsilon_{C60} = 4.25$ is the relative dielectric constant for the C_{60}[109] and V_{bi} is the built-in potential. From the slope of the curve, we obtained $N_{C60} = 9.1\text{x}10^{17}$ cm^{-3} and from the interception with the voltage axis, we obtained $V_{bi} = 0.97$ V. From region II, we calculated N_{Pc}, using the following relationship[108]:

$$V_D^{\ *} = V_{bi} + \left(\frac{q}{2\varepsilon_o\varepsilon_{Pc}}\right)N_{Pc}d^2 \tag{4.2}$$

where $V_D^* = 21$ V is the intercept on the voltage axis , $\varepsilon_{Pc} = 6.7$ is the relative dielectric constant for the Pc[110] and $d = 30$ nm is the thickness of the C_{60} layer. Using Eq. 4.2 we obtain $N_{Pc} = 1.7\times10^{19}$ cm^{-3}.

To simulate the capacitance-voltage characteristics, it was assumed that 2.80 eV and 4.85 eV are the energies for Pc LUMO and HOMO levels, respectively, and 3.50 eV and 6.17 eV for the C_{60}[11]. The simulated curve, using AFORS-HET (see Apendix C), is also shown in Fig. 37 (solid line).

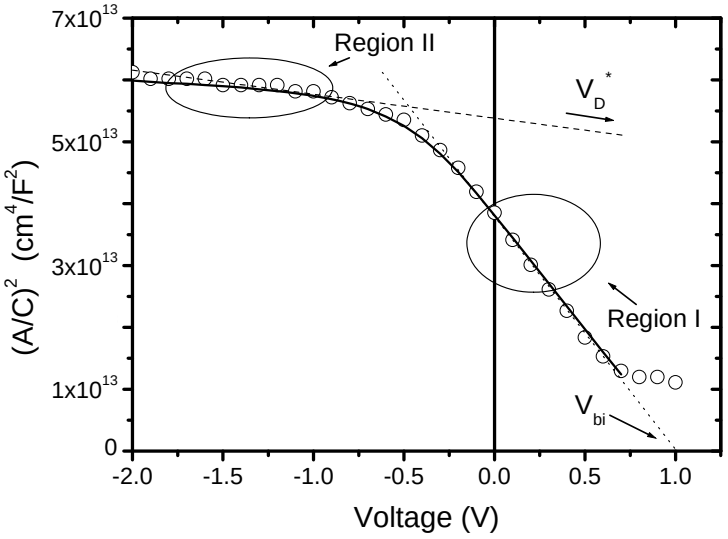

Fig. 4.7: Experimental (symbol) and simulated (line) C-V characteristics of Pc/C_{60} diode. The dotted lines represent the extrapolation of the C-V values in region I and region II.

The agreement between this curve and the experimental one was good, both region I and region II. This result validates the parameter extraction using Eq 4.1 and 4.2.

4.4 C-V characteristics and built-in potential

At this time the origin of built in potential in organic solar cells is also a controversial topic. Some researchers suggest that in organic heterojuntions the charge distribution does not occur as in inorganic case. However, Liu et al.[47] showed the built in potential of the donor-acceptor heterointerface is essential for the efficient operation of small molecule organic solar cell devices. The capacitance measurements, showed in previous section, is additional experimental evidence about the existence of such built-in potential in Pc/C_{60} organic solar cells. The origin of built-in potential can be the distribution of charge at the interface due to initial charge carrier gradients in the heterojunction interface. Additionally interfacial dipoles can be contributing to such built-in potential[112]. It is important have in mind that in this kind of materials this potential can be influence also by the DOS. Here we simulated the V_{bi} for Pc/C_{60} using an effective charge concentration.

4.5 Study of C-V characteristics

In this section, the effect of C_{60} thickness, which is the totally depleted layer, and charge carrier concentrations of both materials Pc and C_{60} on simulated capacitance-voltage curves are analyzed. Similar values to the calculated ones in section 4.4 are assumed for simulations. From simulated C-V curves, charge carrier concentrations and built-in potentials are calculated using Eq. 4.1 and 4.2, and compared with the assumed values in order to discuss the restriction and the accuracy using such equations.

4.5.1 Dependence of the C_{60} layer thickness

Fig. 4.8 shows C-V curves for different C_{60} thickness. Note that as C_{60} thickness increases, the region II decreases. When C_{60} thickness is around 75

nm, the region II is not observed. It is due to the partial depletion of the C_{60} layer.

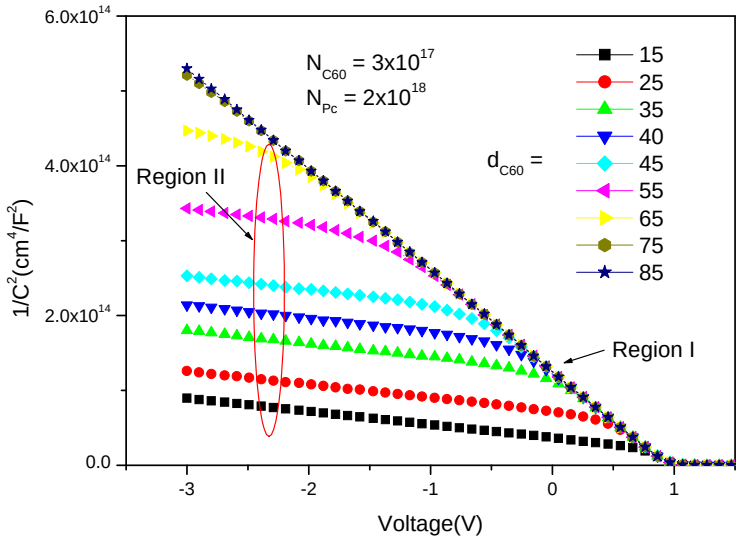

Fig. 4.8: Simulated capacitance-voltage curves for different C_{60} thicknesses d_{C60} in nm.

Table 4.1 shows V_{bi} and N_{C60} values, which were calculated from region I for each thickness using Eq. 4.1.

C_{60} thickness (nm)	15	25	35	40	45	55	65	75	85
N_{C60} (1x10^17 /cm³)	4.62	3.05	2.82	2.75	2.69	2.64	2.61	2.61	2.61
V_{bi} (V)	1.01	0.97	0.96	0.96	0.95	0.94	0.93	0.93	0.93

Table 4.1. N_{C60} and V_{bi} values calculated using region I in Fig. 4.8 and Eq. 4.1.

The assumed value for N_{C60} was 3 x 10^{17} cm^{-3} and 0.94 V for V_{bi}. V_{bi} was calculated from the difference of the work functions between C_{60} and Pc. If we compare these values with the ones shown in Table 4.1, we observe that all of them are similar; the biggest errors are for the lowest thicknesses of

C_{60}. We found an error of 7.5% and 54 % for V_{bi} and N_{C60} respectively when d_{C60} = 15 nm. On the other hand for the highest values of C_{60} thickness, V_{bi} and N_{C60} were 0.93 V and 2.61 x 10^{17} cm^{-3} respectively, leading in errors of 1% and 13%.

Table 4.2 shows the N_{Pc} values, calculated from region II and using Eq. 4.2.

C_{60} thickness (nm)	15	25	35	40	45	55	65	75	85
N_{Pc} (1x10^18/cm³)	2.03	2.12	2.23	2.16	2.11	2.07	1.60	-	-

Table 4.2: N_{Pc} values calculated from region II of Fig. 4.8 and using Eq. 4.2.

The N_{Pc} value assumed in simulations was 2 x 10^{18} cm^{-3} which is similar to the calculated ones shown in Table 4.2. Note the N_{Pc} value with the lowest error is obtained by the 15 nm-thick C_{60}. The reason is that at such thickness, the C-V curve is dominated by the C_{60} layer.

4.5.2 Dependence of charge carrier concentrations

Fig. 4.9 shows C-V curves at different N_{C60}, and one fixed value of N_{Pc} = 2x10^{18} cm^{-3}. Note that region II is only observed when N_{C60} is sufficiently smaller than N_{Pc}. Under this condition the C_{60} layer is totally depleted.

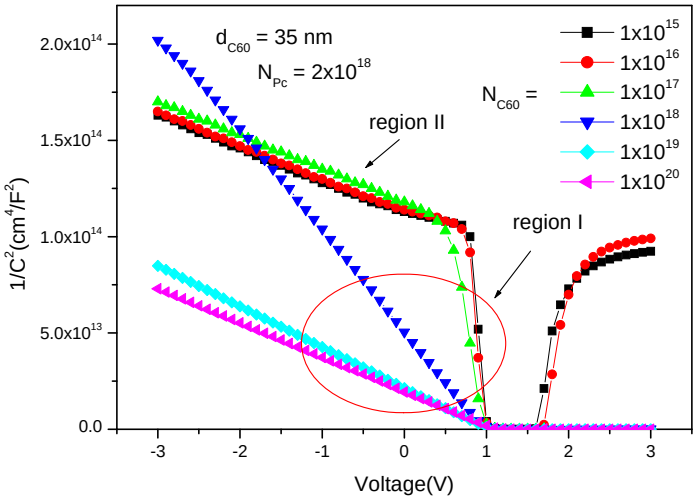

Fig. 4.9 Simulated C-V curves for different C_{60} charge carrier concentrations N_{C60} in cm^{-3}.

Table 4.3 shows N_{C60}, N_{lowest} and V_{bi} values. There are both, the values for V_{bi} assumed in simulations, and the calculated ones using Eq. 4.1. The charge carrier extraction calculated with Eq. 4.1 corresponds to the lowest charge carrier concentration in the junction. Note in table 4.3 that with exception of N_{C60} = 1x10^{15} cm^{-3}, which leads an error of one order of magnitude compared to N_{lowest}, the rest of N_{lowest} are similar to N_{C60}, however for N_{C60} = 1x10^{19} and 1x10^{20} cm^{-3}, N_{lowest} corresponds to N_{Pc} = 2x10^{18} cm^{-3}, because at these N_{C60} values $N_{Pc} << N_{C60}$.

N_{C60} (/cm³)	1x10^15	1x10^16	1x10^17	1x10^18	1x10^19	1x10^20
N_{lowest} calculated (/cm³)	7.35x10^16	7.99x10^16	1.35x10^17	6.93x10^17	1.67x10^18	1.98x10^18
Vbi (V)	0.83	0.89	0.95	1.01	1.07	1.13
Vbi calculated (V)	1.01	1.00	0.97	1.00	1.02	1.10

Table 4.3. Charge concentration and V_{bi} values calculated using the region I in Fig. 4.9 and Eq. 4.1.

Note in Fig. 4.9 that region II is only observed for N_{C60} = 1x10^{15}, 1x10^{16} and 1x10^{17} cm^{-3}. From this region, N_{Pc} was calculated using Eq. 4.2. The N_{Pc} values were: 1.97, 1.97, and 2.17 x10^{18} cm^{-3} respectively. These are similar to the assumed N_{Pc} value of 2 x10^{18} cm^{-3}.

In the following case, N_{C60} was fixed and N_{Pc} was varied. A new region is observed for low N_{Pc} concentrations as shown in Fig. 4.10. Such region can be attributed to the total depletion of charge in Pc.

Table 4.4 shows N_{Pc}, N_{lowest} and V_{bi} assumed values for simulations and the calculated ones. Note again that for the two lowest N_{Pc} values, there are significant errors with respect to the calculated N_{lowest} ones, i.e. one order of magnitude for N_{Pc} = 1x10^{15} cm^{-3}. For $N_{Pc} >> N_{C60}$, the calculated value N_{lowest} corresponds to N_{C60}.

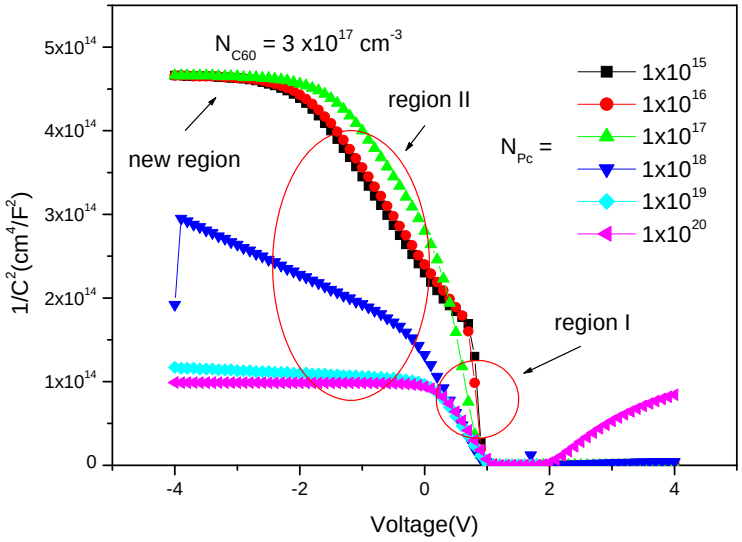

Fig. 4.10: Simulated C-V curves for different Pc charge carrier concentrations N_{Pc} in cm^{-3}.

N_{Pc} (/cm³)	1x10^15	1x10^16	1x10^17	1x10^18	1x10^19	1x10^20
N_{lowest} calculated (/cm³)	3.42x10^16	5.02x10^16	8.87x10^16	2.44x10^17	3.11x10^17	3.14x10^17
Vbi (V)	0.78	0.84	0.90	0.96	1.02	1.08
Vbi calculated (V)	0.93	0.93	0.89	0.93	1.01	1.07

Table 4.4. Charge concentration and calculated V_{bi} values using the region I in Fig. 4.10 and Eq. 4.1.

Finally, Table 4.5 shows the $N_{highest}$ values calculated from region II and using Eq. 4.2. For the three lowest N_{Pc}, $N_{highest}$ corresponds to N_{C60}; and for N_{Pc} = 1x10^{18} and 1x10^{19} cm^{-3}, $N_{highest}$ corresponds to N_{Pc}. Note that for N_{Pc} = 1x10^{20} cm^{-3} the slope of region II is zero. In these last calculations, the highest error is 45% for N_{Pc} = 1x10^{18}.

N_{Pc} (/cm³)	1x10^15	1x10^16	1x10^17	1x10^18	1x10^19	1x10^20
$N_{highest}$ (/cm³)	4.37x10^17	4.34x10^17	3.61x10^17	1.24x10^18	1.13x10^19	-

Table 4.5. $N_{highest}$ values, calculated from region II in Fig. 4.10 and using Eq. 4.2.

4.6 Relation between the barrier interface and the built-in potential

To establish a relation between the obtained barrier heights and the built-in potential, the donor-acceptor model for the band-energy diagram recently used for small molecule organic solar cells was used[47]. Fig. 4.11 shows the simulated band-energy diagram in equilibrium using AFORS-HET v2.2. The equivalent Fermi levels of the layers were calculated using the effective doping concentration values previously obtained in section 4.4, $E_{F,C60} = k_B T \times \ln(1\times10^{21}/N_{C60}) = 0.18$ eV and $E_{F,Pc} = k_B T \times \ln(1\times10^{21}/N_{Pc}) = 0.11$ eV.

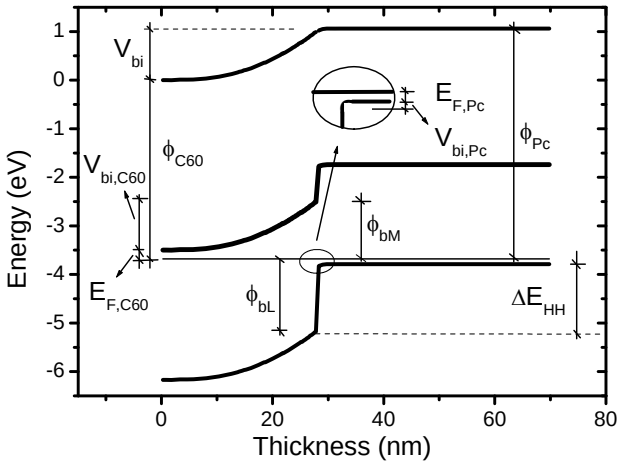

Fig. 4.11 Proposed energy band diagram for the Pc/C_{60} heterojuntion in equilibrium.

Because of the barrier height energies Φ_{bL} and Φ_{bM} are localized in the interface, we used the band-energy diagram to determine that

$$\Phi_{bM} = E_{F,C60} + qV_{bi,C60} \quad (4.3)$$

$$\Phi_{bL} = E_{F,Pc} + qV_{bi,Pc} + \Delta E_{HH} \quad (4.4)$$

where $V_{bi,C60}$ and $V_{bi,Pc}$ are the built-in potentials in C_{60} and Pc, respectively, and ΔE_{HH} is the difference in HOMO levels between Pc and C_{60}. Using these equations, we obtain $V_{bi\text{-}C60} = 0.90$ V and $\Delta E_{HH} = 1.30$ eV, assuming $V_{bi\text{-}Pc} = V_{bi} - V_{bi\text{-}C60} = 0.07$ V. These values are in good agreement with the simulated values in the band-energy diagram.

Finally, from the band-energy band diagram we can also determine

$$qV_{bi} = \phi_{Pc} - \phi_{C60,} = E_{H\text{-}Pc} - E_{L\text{-}C60} - E_{F,Pc} - E_{F,C60} \qquad (4.5)$$

where $E_{H\text{-}Pc}$ is the HOMO level value of the donor and $E_{L\text{-}C60}$ is the LUMO level value of the acceptor. Using Eq. 4.5 and the values mentioned above, we obtain $V_{bi} = 1.06$ V. The difference between this value and the experimental one, 0.97 V, is within the tolerance of the error in the measurement of the HOMO and LUMO values, namely ± 0.2 eV[111]. In addition, it should be taken into account that the C-V characteristics could be slightly affected by the excitation frequency[113].

4.7 Effect of C_{60} thickness on the charge collection in Pentacene/C_{60} solar cells

In this section we analyze the origin of the enhancement of the photocurrent when the C_{60} thickness increases in Pc/C_{60} solar cells. To do so, we use a combination of current-voltage characteristics, capacitance-voltage characteristics and energy band diagram simulations.

The fabrication details of this structure are in Appendix A.

4.7.1 I-V dark and illuminated characteristics

Figure 4.12 shows the illuminated and dark (inset) current density-voltage (I-V) curves for the three solar cells. The first difference that can be seen in the illuminated I-V curves is that the photocurrent increases as the thickness of the C_{60} layer increases. In a previous section we found that the reverse saturation current, J_S, is related to charge recombination at the interface for similar devices. When there is only one conduction mechanism the value of J_S can be obtained by the intersection of the linear region of the inset curve in Fig. 1 with the current density axis. Table I shows the J_S values for all the samples estimated in the medium voltage region (0.3 V < V < 0.6 V). As expected from the dark current behavior the value for the 62 nm samples is small. It is known that if charge recombination increases, J_S increases[79,80]. Therefore, the behavior of J_S further confirms that recombination occurs at the heterojunction interface in this kind of device, because if the recombination were bulk localized, J_S would increase as the C_{60} film thickness increases.

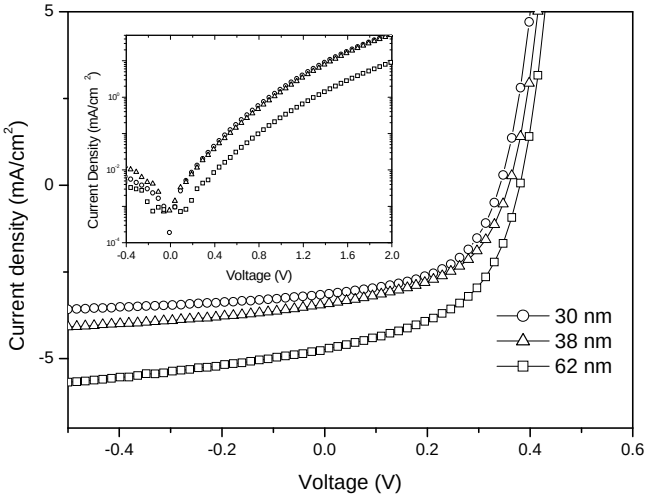

Fig. 4.12: Experimental photocurrent density of the Pc/C_{60} heterojuntion for the three samples with different C_{60} layer thickness. Inset dark IV curves.

Table 4.6 also shows the photovoltaic parameters of the three solar cells. As can be observed, an increase in the thickness of the C_{60} layer increases the efficiency and the short circuit photocurrent . On the other hand, the C_{60} layer thickness does not have a great effect on the open circuit voltage or fill factor. The differences observed in the photovoltaic parameters indicate that device performance is not ultimately limited by contact electrodes. Therefore, the differences can be attributed to the heterojunction.

Thickness (nm)	J_S ($\mu A/cm^2$)	Voc (V)	Jsc (mA/cm^2)	Fill Factor	Efficiency
30	1.84	0.34	3.16	51.26	0.55
38	1.83	0.36	3.43	49.48	0.61
62	0.4	0.38	4.75	49.77	0.90

Table 4.6. Values of inverse saturation current J_S and photovoltaic parameters of Pc/C_{60} heterojuntion for three difrerent thickness.

4.7.2 C-V simulations

The experimental capacitance-voltage characteristics were fitted to simulations so that the physical parameters used in the simulation of the energy band diagrams in equilibrium could be validated. Figure 4.13 shows the Mott-Schottky plot for both the experimental and simulated curves for the three samples.

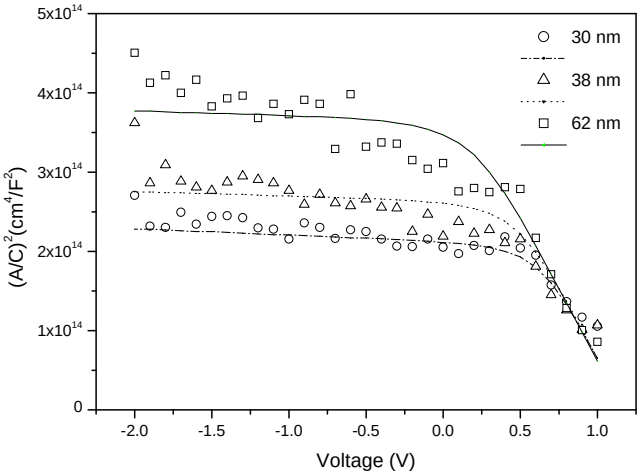

Fig. 4.13: Experimental (symbol) and simulated (line) capacitance-voltage characteristics of the Pc/C60 diode for the three samples.

The simulation was performed using the dielectric constant (ε), the Highest Occupied Molecular Orbital (HOMO), the Lowest Unoccupied Molecular Orbital (LUMO), the effective doping concentration (N_{C60} and N_{Pc}) and the thickness (d_{C60} and d_{Pc}) for C_{60} and Pc, respectively. We take the following values from literature: LUMO Pc / C_{60} = 2.8 eV / 3.3 eV, HOMO Pc / C_{60} = 4.8 eV / 6.17 eV,[111] and ε_{Pc} = 6.7[110]. The value $N_{Pc} = 1.7\times10^{19}$ cm^{-3} was assumed from previous simulations. The fitting parameters for the samples were $N_{C60} = (1.6 \pm 0.6)\times10^{17}$ cm^{-3} and ε_{C60} = 2.8, 3.1, 3.9 (for d_{C60} = 30, 38 and 62, respectively, with an error of ± 0.1 for them all). These fitting values are similar to those previously reported[109]. There may be two reasons for the variation in ε_{C60}: first, the C_{60} oxygen absorption[114] and second, the structural changes in the molecular orientation in the C_{60} films[109]. We suggest that in our devices the variation in the C_{60} dielectric constant is due to the structural changes in the C_{60} molecular orientation, because the C_{60} layer for the 38 nm and 62 nm samples were evaporated in two and three steps, respectively, as has been explained in detail in the experimental section. Moreover, the samples were kept under nitrogen (<0.01 ppm O_2, <0.01 ppm H_2O) during

preparation, storage and measurement, so oxygen absorption can be discarded.

4.7.3 Energy band diagram and the origin of photocurrent increases

Figure 4.14 shows the simulated energy band diagrams in equilibrium for the three samples using the above parameters. We found that for the three samples the C_{60} layer is totally depleted and the built in potential value is V_{bi} = 1.2 V. This value is consistent with the V_{bi} value estimated from the interception of the C-V curves with the voltage axis in Figure 4.13. The relationship between the internal electric field (E_{bi}) and V_{bi} is given by $V_{bi} = d_{C60} \times E_{bi}$. In this case d_{C60} was used as it corresponds to the totally depleted layer. E_{bi} is in the order of 10^5 V/cm^{-1} for all samples. In Figure 4.14, E_{bi} is the slope average of the band bending for each sample.

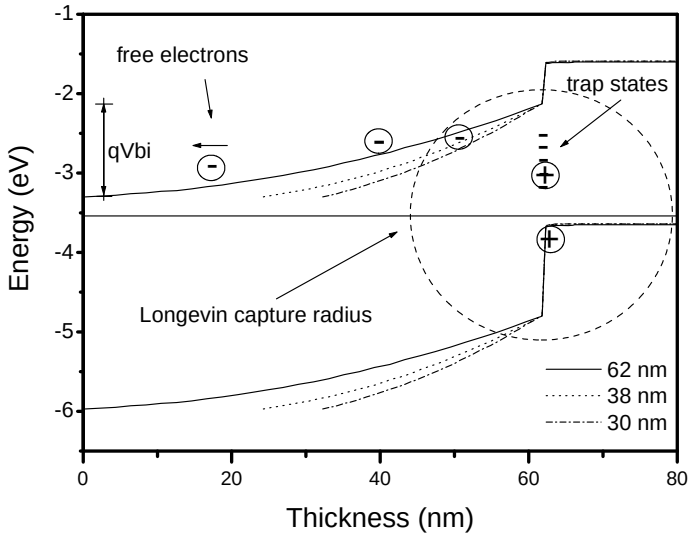

Fig. 4.14: Simulated energy band diagram for the Pc/C_{60} heterojuntion in equilibrium for the three samples. The influence of the thickness on the charge collection are show.

To analyze the effects of C_{60} thickness on the charge collection in the three samples, we assumed that a change in the C_{60} dielectric constant is not responsible for the photocurrent differences for all the samples. It has been reported that a variation in the C_{60} dielectric constant can change the conductivity (σ)[114]. This variation in conductivity would lead to a change in series resistance (R_s) in the device because $R_s = d_{C60}/\sigma \times A$. However, significant changes in the solar cell series resistance are not observed, It was calculated by the inverse of the slope in the I-V curve around the voltage axis on Figure 4.12.

In the model described by Pandey et al.[104], the excitons are generated in both the Pentacene and C_{60} layers. In this experiment, the Pc layer has a fixed thickness and our internal electric field is negligible for this layer because $N_{Pc} >> N_{C60}$. Therefore, no changes are expected in the free carrier collection assigned to the Pc layer in the three samples. The exciton diffusion length of the C_{60} layer reported in the literature is 40 ± 5 nm[113], so the photocurrent variation observed in samples with a C_{60} thickness of 30 nm and 38 nm could be attributed to the difference in photon absorption, as the layer thickness is within the range of the exciton diffusion length[110]. However, the C_{60} layer of 62 nm is thicker than the exciton diffusion length, which suggests that the photocurrent enhancement is also affected by other factors. Interestingly, similar phenomena have been observed for a phase separation significantly larger than the exciton diffusion length in conjugated polymer blends[115].

For a bilayer structure, Peumans et al.[47] suggested that the increase in the magnitude of the E_{bi} at the heterojunction interface region, increases the separation of geminated pairs. However, as pointed out above, E_{bi} varies only slightly between each sample. Therefore, no significant changes are expected in the separation of geminated pairs as a result of variation in E_{bi}.

We propose that the increase in the photocurrent in the 62 nm-thick C_{60} sample is caused by the decrease in the recombination of the geminated pairs at the heterojunction interface. Although E_{bi} makes no contribution to charge

separation increases, it affects charge recombination. This is because the distance between the free electrons and the holes in the 62 nm C_{60} sample is greater than in the other samples. Therefore, the holes in the Pc valence band—even ones in the interface (trapped holes)—can capture more electrons. The capture radius, which has been called the Longevin capture radius, has been reported to be around 20 nm for small molecule organic materials[32]. From simulations, we estimated that this effect can be significant up to a layer thickness of 90 nm C_{60}. This coincides with the point at which the C_{60} layer starts being partially depleted and the distance from the depleted conduction band to the interface is the same independently of the C_{60} thickness. This approach is consistent with the lowest value of the dark reverse saturation current density for the 63 nm sample, and it should be taken into account that this parameter had previously been related to charge recombination[79,80].

4.8 Summary of results

In conclusion, the conduction mechanism limiting the dark current-voltage characteristics in the Pc/C_{60} heterojunction is tunneling-enhanced interface recombination. From the C-V characteristics we obtained N_{C60} = 9.1x10^{17} cm^{-3} and N_{Pc} = 1.7 x 10^{19} cm^{-3}. A band-energy diagram in equilibrium was simulated and validated by fitting with the experimental C-V characteristic.

The effect of C_{60} thickness and charges concentrations were studied by simulations. At the same time Ec. 4.1 and 4.2 were validated. We conclude that there is one order of magnitude errors using Eq. 4.1, when C_{60} has low charge carrier concentrations (1x10^{15} cm^{-3}).

Afterwards we determined that as observed in typical EBD, the barrier height for the electrons was the sum of the Fermi level and built-in potential in C_{60}. We also showed that the barrier height for holes is the sum of the Pc Fermi level, the built-in potential in Pc, and the difference between the Pc and C_{60} HOMO levels. The present result, together with the classical relation between V_{OC} and J_S already proved in small molecule solar cells, suggests that the open-circuit voltage is not only limited by the LUMO and HOMO values of the C_{60} and Pentacene, respectively, but also by the Fermi levels and the interface properties between these materials.

Finally, Pentacene / C_{60} devices were prepared with three different C_{60} thickness. It was found that the device prepared with 62 nm of C_{60} performed best, mostly due to an increase in photocurrent. After carrying out a variety of simulations, we propose that the photocurrent increases because of the reduction in geminated pairs and their subsequent recombination at the interface.

Chapter 5

Chapter 5

P3HT:PCBM solar cells

Here the I-V characteristics of P3HT:PCBM solar cells fabricated at different laboratories were analyzed. Afterwards the conduction mechanism for one sample was determined. Finally the degradation effects related to hole transport layer were studied using I-V, C-V, and C-f (capacitance-frequency) characteristics. Interestingly, some differences were observed in DOS distributions, which were calculated using C-f measurements.

5.1 Illuminated I-V characteristics

Recently power conversion efficiencies around 8% have been reported in polymer:fullerene BHJ solar cells[45]. The OBHJ solar cell is interesting from a processing point of view, as the active layer is solution processable. This allows for the low cost production of photovoltaics on large area, flexible substrates at low temperatures.

Although devices were fabricated in different laboratories the fabrication process is similar. It is indicate in Appendix A.

Fig. 5.1 shows the dark and illuminated I-V curves of the P3HT:PCBM OBHT's solar cells. The fabrication laboratories are indicated in Table 5.1. The parameters of the illuminated I-V curves and cathode materials are also indicated in Table 5.1. All devices were encapsulated except m4 and m5. As it can be observed the main differences between devices are *Jsc* and *FF*. In OBHT the variation of such parameters can be attributed to different causes like: spectroscopy absorption, mobility, and defect distribution[76]. Therefore, determined the nature of such variation considering only I-V curves at one temperature is a bit speculative. However here it was introduce a discussion about the differences on these curves considering that there are some technological differences.

The cathode material does not appear to be a determinant factor in solar cell efficiencies. However the highest efficiencies are for Ca/Ag solar cells. The lowest efficiency devices were m3 and m4. It was attributed to device degradation, because m3 was measurement several days after fabrication leading Al contact oxidation, and m4 in contrast to m5 was fabricated outside glove box.

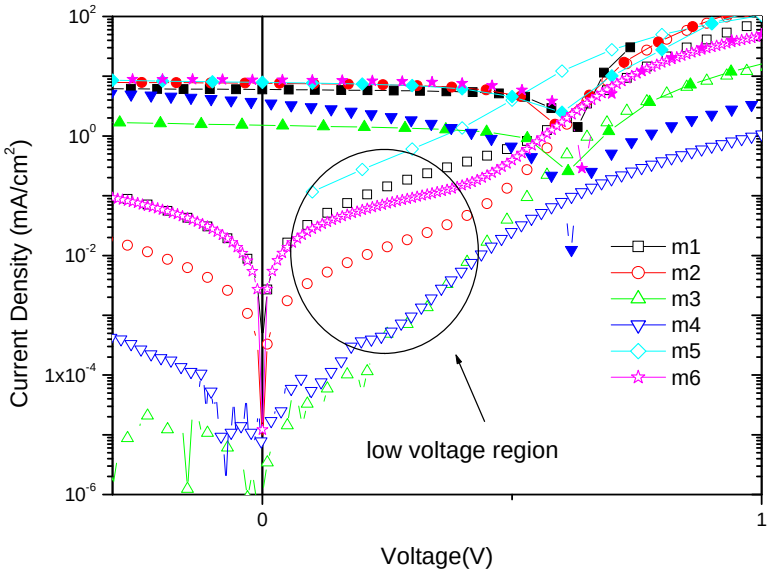

Fig. 5.1 Dark and illuminated (fill symbols) I-V characteristics of the P3HT:PCBM bulk heterojuntions fabricated in different laboratories.

Sample	Jsc (mA/cm^2)	Voc (V)	FF	Efficiency	Cathode Material	Laboratory	Ref.
m1	6.00	0.63	64.6	2.44	Ca/Ag	IKERLAN	-
m2	7.66	0.59	52.4	2.36	Ca/Ag	IKERLAN	-
m3	1.44	0.62	57.6	0.51	Al	IKERLAN	116
m4	3.55	0.61	24.7	0.55	Ca/Ag	URV/ICIQ	-
m5	7.66	0.60	50	2.29	Al	ICIQ	117
m6	8.7	0.60	52	2.76	Ca/Ag	EHF	118

Table 5.1. Photovoltaic Parameters, Cathode Material and laboratory for OBHT solar cells

As can be observed in Fig. 5.1 for dark I-V curves, the degraded samples (m3 and m4) do not present an additional slope at low voltage region. It suggests that this change can be related to degradation mechanisms. Similar slopes observed in the Si/P3HT and Pc/C60 solar cells were explained like additional conduction mechanism in the same heterojuntion however here the problem turns more complex, because there can be other junctions in parallel to the P3HT/PCBM one i.e. Ca/P3HT or PEDOT/PCBM[117]. In

addition it will be show in section 5.4, the interface involving HTL has an important role in solar cells performance. It means that additional mechanism involving such interface should be considered at least in degradation studies. For this reasons, in principle the m3 dark conduction mechanism analysis is presented here.

5.3 Conduction mechanisms

Figure 5.2 shows the dark current J-V characteristics of the sample m3 measured at ± 2 V for temperatures between 300 and 360 K. This curves show the typical diode-like behavior.

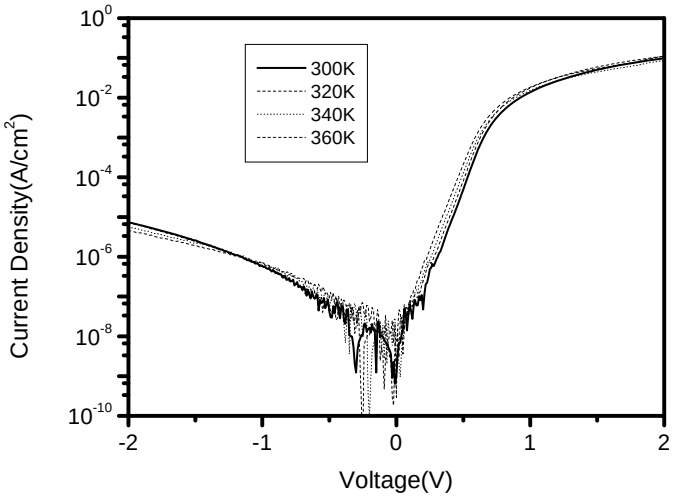

Fig. 5.2 Dark current I-V characteristics of the ITO/PEDOT:PSS/P3HT:PCBM/Al solar cell at different temperatures.

The electrical equivalent circuit used to fit the experimental dark I-V characteristics is the single diode model (Fig. 2.12 without current source).

Figure 5.3 shows the forward density current contribution of the different conduction mechanism terms to the total current at 300 K. Note a good agreement between calculated and experimental curves. The plot can be described using three distinctive regions: a) region below 0.2 V, where the current is affected by R_{SH}, b) region between 0.2 V and 0.6 V, where the current is limited by J_D, and c) region above 0.6 V, where the current is limited by SCLC and R_S.

From the model, the calculated R_{SH} value is 150 MΩ at 300K and this decrease when the temperature increases until 70 MΩ at 360 K. In addition, the calculated R_S value is 200 Ω at 300 K and decreases when the

temperature increases until 150 Ω at 360 K. Finally, the calculated m value is 2 for all the range of temperatures measured. These m values are typical for SCLC mechanism .

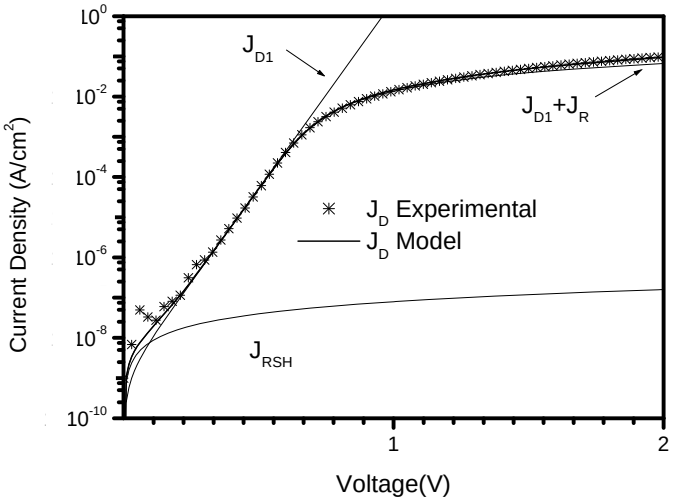

Fig. 5.3: Forward dark current density-voltage characteristics of the ITO/PEDOT:PSS/P3HT:PCBM/Al solar cell at 300 K.

Figure 5.4 shows the temperature dependence of the exponential factor *A*. We can see that the trend line is almost constant, which means that a tunneling mechanism current is present in the medium voltage region.

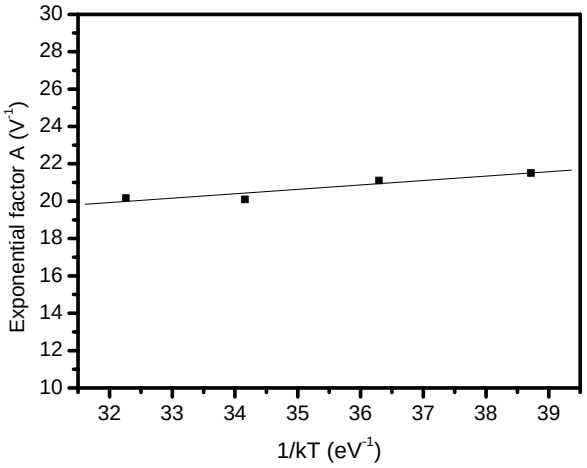

Fig. 5.4: Temperature dependence of the exponential factor *A*.

In order to analyze the type of tunneling present in the device, Fig. 5.5 shows the dependence of reverse saturation current with respect to the temperature.

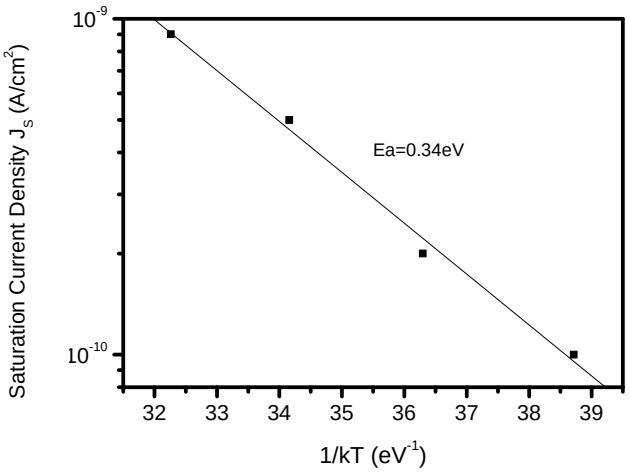

Fig. 5.5: Arrhenius plot of the saturation current density J_S.

Because of J_S depends exponentially on $1/k_BT$ we can assume that MTCE mechanism is present. From this mechanism J_S is given by Ec. 2.12.

Assuming that the semiconductor with higher charge concentration is PCBM and according to MTCE model, the activation energy obtained of 0.34eV corresponds at the Fermi level of P3HT. The difference between this value and the one obtained in chapter 3 can be due to a change at the P3HT morphology film. Fig. 5.6 shows a diagram of the conduction mechanism proposed at medium voltage. The electrons are tunneling from PCBM to the Fermi level of P3HT and then the capture of holes from the HOMO level in this semiconductor occurs. We can conclude that the concentration of holes in the HOMO level of the P3HT is the limiting factor of the saturation current in the device.

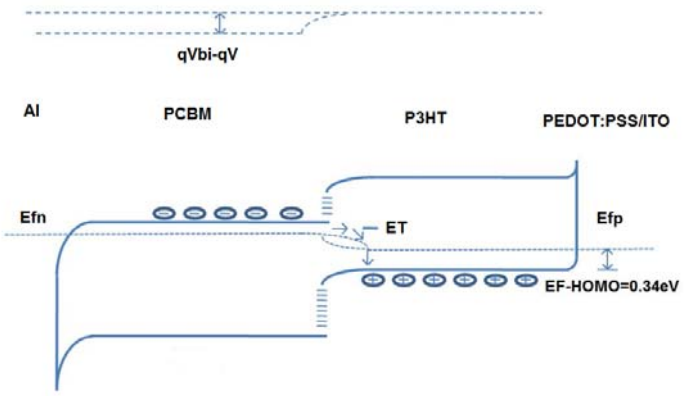

Fig. 5.6: Band diagram at low forward bias voltage with proposed tunneling mechanism in the ITO/PEDOT:PSS/P3HT:PCBM/Al solar cell and built in voltage V_{bi}.

Assuming N_V of $1x10^{21}$ cm^{-3} for the P3HT, the charge concentration using Boltzmann approximation can be estimated to be $1.9x10^{15}$ cm^{-3}. This result is similar to $1.1x10^{15}cm^{-3}$ at 250 K obtained for Chirvase et al.[119] for an ITO/P3HT/Au structure.

5.3 Degradation effects related to the hole transport layer (HTL)

To bring organic solar cells with full success onto the market, in addition to higher efficiencies and cost-effective processing, longer device lifetimes are necessary[120]. Recent research has been focusing on this subject and two major points regarding the stability and longevity of organic solar cells are addressed in the literature. Firstly, strategies to provide extrinsic stability through the use of proper encapsulation to prevent degradation due to ambient oxygen and water are being investigated, and secondly research is being conducted to improve the understanding of the intrinsic stability of the different thin film materials and interfaces present in the solar cell in order to isolate the origins of solar cell degradation.

The unique degradation mechanisms affecting the active layer, the interfaces, the transport layers, and the contacts are not yet well understood. A variety of different approaches and techniques is reported in the literature to investigate the intrinsic mechanisms leading to device degradation[121-125].

In this section the effect of the HTL on the stability of polymer:fullerene bulk heterojunction solar cells has been investigated. A blend of P3HT:PCBM was used as the active layer. Solar cells were prepared with the different HTLs, two water based dispersions, (PEDOT:PSS (H_2O)) and (PANI:PSS (H_2O)), and one isopropyl alcohol based (PANI:PSS (IPA)). Devices were fabricated at EHF laboratory. The details about preparation can be found in ref 118. The HTLs additionally differed from each other in composition, conductivity and work function. The characteristics of the HTLs are summarized in Table 5.2**.** By varying only the HTL between the devices, the degradation effects related specifically to the HTL interface in the device were isolated. The characteristics of non encapsulated and encapsulated cells were compared to gain insight into the difference between internal and external degradation mechanisms at the HTL interface.

HTL	Solvent	pH value	Transmittance [%] [a]	Solid content [wt%]	Work function [eV] [c]	Conductivity [S/cm] [b]
PEDOT:PSS (H_2O)	water	1.5	94	1.5	4.81	3.9 E-4
PANI:PSS (H_2O)	water	1.6	76	3.0	5.08	3.0 E-2
PANI:PSS (IPA)	2-propanol	-	86	2.3	5.49	1.6 E-3

Table 5.2: Properties of the hole transport layers used in this study. [a] layer thickness: 100nm; measured from 400nm to 900 nm, [b] measured in vacuum at room temperature, [c] measured by Kelvin probe in air at 0% relative humidity and room temperature.

5.3.1 Illuminated I-V characteristics

To investigate the solar cells, I-V characteristics were measured under different illumination intensities. Fresh solar cells were measured initially under 1 sun, and subsequent measurements were performed under increasing light intensities, at 16, 30, 48, 80, and 100 mW cm^{-2}. The solar cells were under illumination for a total of 7 hours. In Figure 5.7 the initial and final I-V characteristics of the solar cells at 100 mW cm^{-2} for the non encapsulated cells (a) and the encapsulated cells (b) are shown.

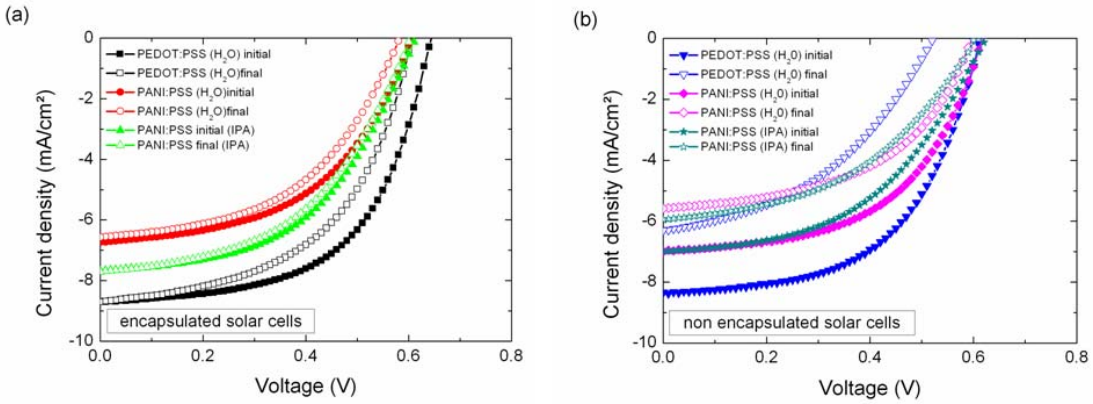

Figure 5.7: I-V characteristics of (a) encapsulated and (b) non-encapsulated solar cells with different transport layers before and after photo-degradation.

The cells prepared with PEDOT:PSS (H_2O) initially demonstrated the best performance. This is attributed to the difference in transmittance of the HTLs[118]. The PEDOT:PSS layer has a higher transmittance compared to the PANI:PSS layer based solar cells, allowing for more light absorption by the active layer and therefore an increase in the photogeneration of charge, leading to a higher short circuit current density.

From the comparison between the initial and final measurements it can be seen that a decrease in the solar cell performance occurs for both encapsulated and non encapsulated devices. In the case of the non encapsulated devices, J_{sc} is significantly diminished between the initial and final measurements in all devices. Additionally there is a decrease in the fill factor of the devices, and in the case of PEDOT:PSS (H_2O) the V_{oc} is considerably lower after degradation. In general, the sample prepared with PEDOT:PSS (H_2O) shows the largest effects of degradation while the PANI:PSS (IPA) resulted in the most stable devices.

Regarding encapsulated devices, the degradation effects in all devices are minimal in comparison to the non encapsulated devices. J_{sc} remains constant between the initial and final measurements for all the HTLs. A decrease in the fill factor and in V_{oc} is apparent primarily in the PEDOT:PSS (H_2O) based device, and to a smaller degree in the PANI:PSS (H_2O) based device.

Again, the PANI:PSS (IPA) HTL results in the least variation between the initial and the final measurements, and these results indicate that using IPA based HTLs can increase the lifetime of organic solar cells, even in the case of encapsulated devices.

5.3.2 C-V characteristics and charge carrier extraction

To obtain deeper insight into the processes involved in the degradation associated with the HTL, C-V characteristics of the solar cells were used.

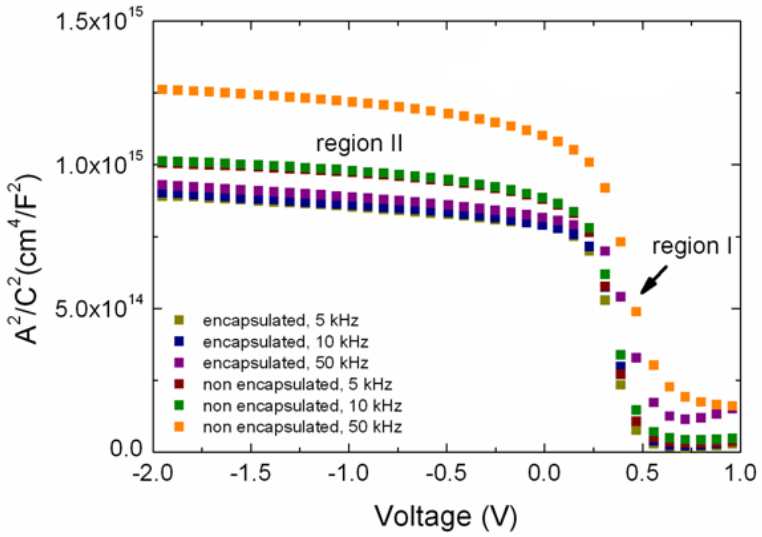

Fig. 5.8: Mott-Schottky representation of experimental C-V data (symbols) measured in the dark of a) encapsulated and non encapsulated devices containing PEDOT:PSS (H_2O) as hole transport layer.

In Figure 5.8 the C-V characteristics of the PEDOT:PSS (H_2O) based device conducted in the dark at frequencies of 5 kHz, 10 kHz and 50 kHz are shown in the Mott-Schottky representation. The same trend was observed for the other devices (not shown here). As Pc/C_{60} solar cells, two regimes with different slopes can be observed from the characteristics, one (I) at around 0 V to +0.5 V and the second (II) at -2 V to 0 V. These regimes are related to

the profile of the space charge in the device in inorganic junctions[108] and have been attributed to the contributions from the P3HT phase (I) and the PCBM phase (II) in polymer:fullerene bulk heterojunction structures.[29] Probing the capacitance vs. voltage over different frequencies demonstrates that the slopes in both regions I and II remain constant but a shift in the characteristics with increasing frequencies to higher forward voltages can be observed. This implies that the built-in voltages, which are given by the extrapolated interception of the respective region with the voltage axis, depend on the frequency applied during the measurement, an indication that interface traps are present[26,126].

The P3HT charge carrier concentration from region I, assuming that $N_{PCBM} >> N_{P3HT}$, can be extracted using classical abrupt junction model (Ec. 4.1).

In this case the totally depleted material is the P3HT. Applying equation (1) to the C-V characteristics recorded at 50 kHz for the various illumination intensities we obtain the charge carrier concentration in the P3HT phase vs. light intensity shown in Figure 5.9.

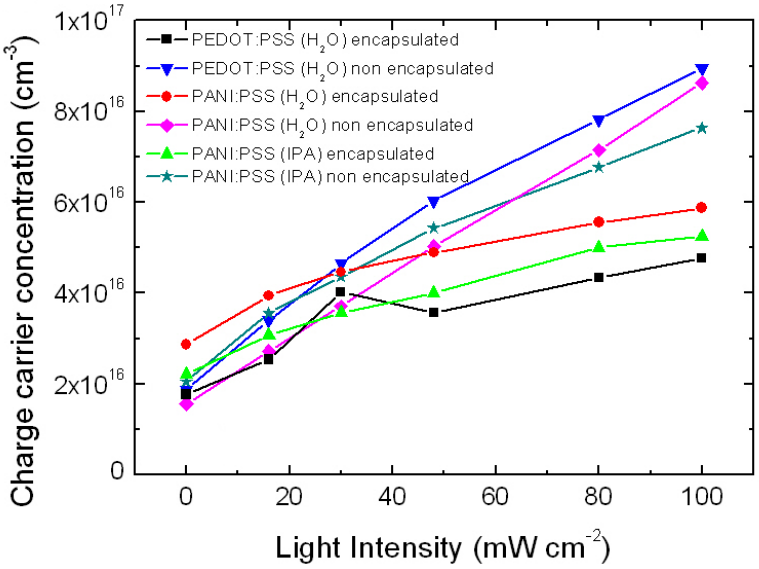

Fig. 5.9: Charge carrier concentration in P3HT plotted versus illumination intensity. Values extracted from C-V measurements taken at 50 kHz.

To calculate the charge carrier concentration in the PCBM phase N_{PCBM} (region II), we assume that the P3HT phase is fully depleted of free charges, so Ec. 4.2 can be used. The calculated charge carrier concentration of the PCBM phase vs. light intensity is shown in Figure 5.10.

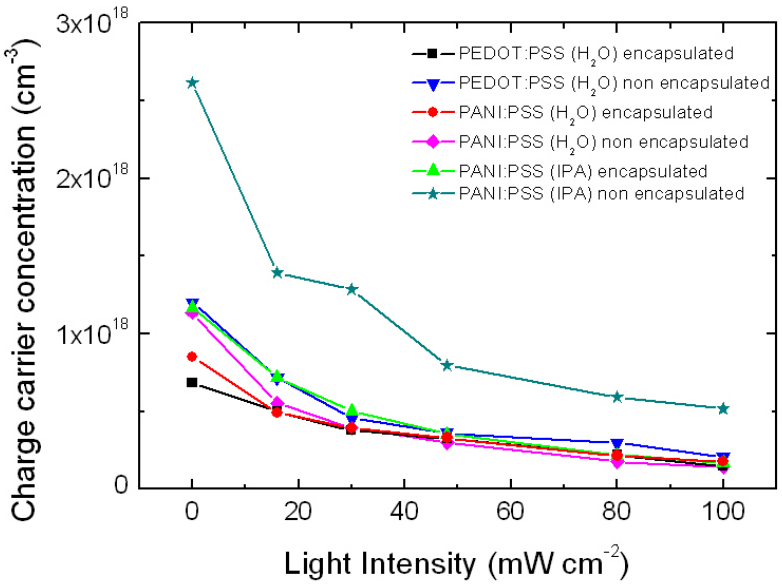

Fig. 5.10: Charge carrier concentration in P3HT plotted versus illumination intensity. Values extracted from C-V measurements taken at 50 kHz.

The extracted free charge carrier concentrations of P3HT and PCBM were used in AFORSHET to simulate C-V data. The simulated data (lines) is presented together with the experimental data for the C-V characteristics (symbols) at 50 kHz in Figure 5.11 and demonstrate good agreement. An error in the sample thickness of 15 nm and in the charge carrier concentration of 4 x 10^{15} cm^{-3} was found.

In the case of P3HT it can be seen that the charge carrier concentration increases with light intensity for all the devices, as expected for the photo-generation of charge in the bulk. There is an increase in the slope of the characteristics in the non encapsulated devices compared to the encapsulated devices. This is attributed to oxygen doping, which introduces trap states for electrons into the bulk[124]. This can result in an increase in the hole density in

the polymer. In the case of PCBM, there is a slight decrease observed in the charge carrier concentration with increasing illumination intensity and degradation time for all devices. This could be due to increased oxidation of the fullerene with degradation time[121]. A decrease of the charge carrier concentration in the acceptor phase has also been observed in degraded solar cells with a copper phthalocyanine (CuPc):N,N'-bis(2-phenylethyl)-perylene-3,4,9,10-tetracarbonicacid-diimide(BPE-PTCDI) heterojunction[47].

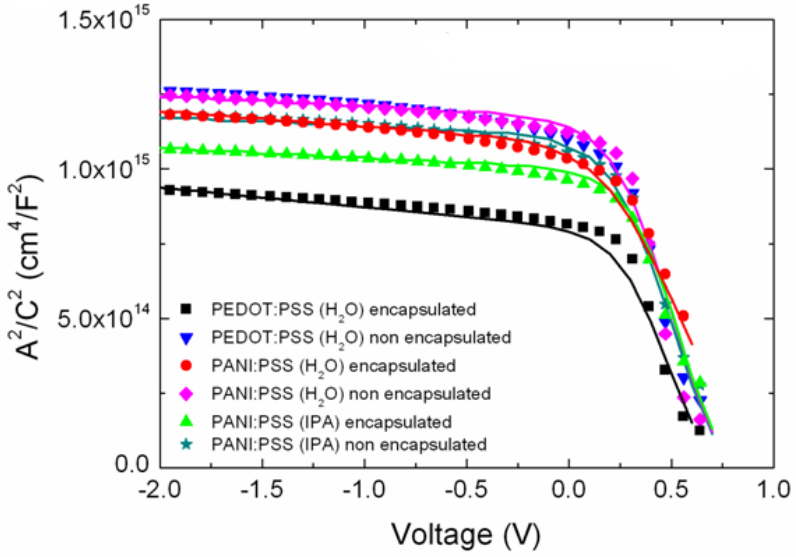

Fig. 5.11. Simulations (lines) compared to experimental data (symbols) of the different hole transport layers at an applied frequency of 50 kHz.

5.3.3 Determination of the density of states (DOS)

Using capacitance vs frecuency measurements we calculated the density of states (DOS) as proposed by Walter et al. for non-crystalline, inorganic materials and applied by Reis et al. for polymer diodes and by Boix et al. for polymer:fullerene solar cells[29,127,128]:

$$DOS(E) = -\frac{V_{Bi} \cdot \omega}{t \cdot q \cdot k_B \cdot T} \cdot \frac{\partial C}{\partial \omega} \tag{5.1}$$

Where, E is the energy, ω is the angular frequency, k_B is the Boltzmann factor and T is the temperature. The assumption in equation (5.1) is that variations in the capacitance of the device with frequency directly correspond to trapping and release of charge by trap sites in the band gap close to the Fermi energy E_F. In the case of disordered organic materials, we understand this to equate to probing transport sites close to E_F located energetically below E_T. In order to convert the angular frequency dependent DOS into the energy dependent DOS, we used[127]:

$$E = k_B \cdot T \cdot In \frac{2 \cdot \beta \cdot N}{\omega} \tag{5.2}$$

Where β is the capture cross section and N is the effective density of states. In this study a value for β was assumed. It should be noted that changes in β only result in a shift of the DOS on the energy scale, and not a change in the shape of the distribution. In the following, the influence of the different HTLs on the shape of the DOS is examinated. The value for β can be extracted from temperature dependent measurements.

Figure 5.12 presents the calculated DOS at open circuit conditions at illumination intensities of 16 mW cm^{-2} (at the start of the degradation

process) and 100 mW cm^{-2} (after degradation), respectively. Two Gaussian distributions at different energetic positions are present. We attribute the Gaussian at lower energies to the DOS in the active layer, as the distribution is common to all the devices. From this analysis, it is not possible to distinguish between contributions from the electron and hole sites to the DOS[127]. The higher noise ratio for the distribution at higher energies is an indication that this distribution accounts for the HTL interface as it also varies between the samples containing different HTLs and is accompanied by flicker noise[129]. The hole transport layers for both encapsulated and not encapsulated devices show a similar behavior at 16 mW cm^{-2}, as the devices are still fresh.

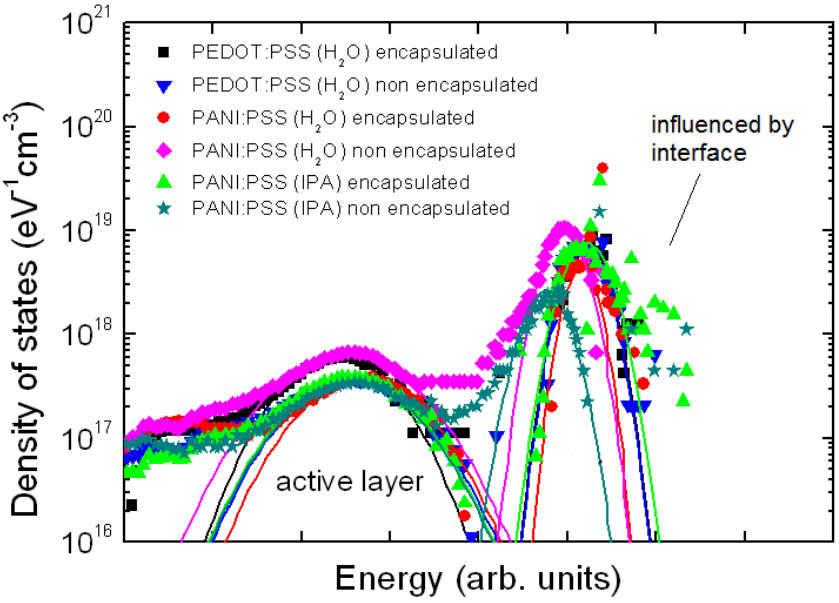

Fig. 5.12: Density of states (DOS) plotted vs. energy for devices illuminated with 16 mW cm^{-2} , under open circuit conditions. Lines show Gaussian fits to states attributed to the bulk and interface.

At 100 mW cm^{-2} (Figure 5.13) the distribution related to the bulk is shifted towards slightly lower energies and a broadening of the distribution is observed. This effect is more apparent in the non encapsulated devices but also visible in the encapsulated devices. This effect may be due to the increase in charge carrier concentration at higher light intensities, leading to the filling of higher energy states. It may, however, also be a result of

degradation, specifically of traps due to oxygen in the case of the non encapsulated devices in addition to internal instabilities in the bulk, such as changes to the morphology, for both non encapsulated and encapsulated devices.

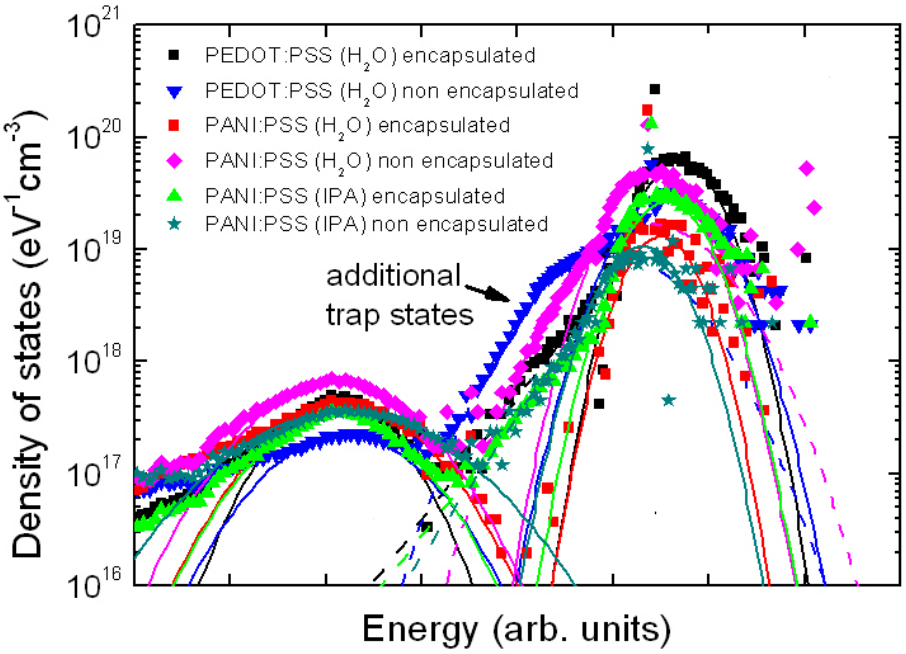

Fig. 5.13: DOS plotted vs. energy for devices illuminated with 100 mW cm^{-2} , under open circuit conditions. Lines show Gaussian fits to states attributed to the bulk and interface. Dashed lines are fits to states originating to interfacial trap states.

The distribution related to the HTL interface also demonstrates a broadening in form and the DOS is shifted away from the bulk related distribution to higher energies compared to the initial data at 16 mW cm^{-2}. Interestingly, in the case of the water based HTLs an additional shoulder becomes visible, which is prominent for the PEDOT:PSS (H_2O) and also observed for the PANI:PSS (H_2O). Additional Gaussian fits in this energy range reveal distributions, which are attributed to the formation of additional trap states at the interface between the HTL and bulk. This is a clear indication that the choice of solvent of the HTL has a major impact on device stability, which is improved with IPA based solvents over water based solvents.

5.4 Summary of results

From the comparison of solar cells fabricated at different laboratories it was observed that the performance of the device are related with an additional slope in dark curves, observed at low voltage regions.

We analyzed the conduction mechanism of a P3HT:PCBM solar cell. In the medium voltage range ($0.2 < V < 0.6$V), the current is limited by MTCE. From Arrhenius plot of the saturation current an activation energy value of 0.34 eV was obtained. At lower voltages ($V < 0.2$V) the current is affected by shunt resistance and at higher voltages ($V > 0.6$V) the current is affected by series resistance and space-charge limited current. Finally, the built in potential of the device was estimated to be 0.90 eV from the saturation of the junction voltage drop.

Finally the stability of the solar cell was observed to be lower in the devices prepared with water based HTLs compared to devices prepared using the IPA based HTL, particularly in the case of non encapsulated devices. In encapsulated devices an increase in the intrinsic stability can be observed for the solar cells prepared with the IPA based HTL. Charge carrier densities extracted from C-V measurements revealed a minimal impact of the ambient conditions on the degradation of the bulk-heterojunction. Degradation effects at the HTL interface, however, were found to be significant, and lead to a shift of the built-in voltage with increasing probing frequency. Finally, the DOS calculated from C-f measurements shows additional trap states for non encapsulated water based HTLs at the HTL-interface.

Chapter 6

Conclusions

Au/P3HT/c-Si/Al heterojunction solar cells have been fabricated and characterized. The best conversion efficiency for this structure was 1.29 %.

A two-diode model ECD was used to model dark I-V characteristics. From the temperature dependence of the parameters in the equivalent circuit we obtained the limiting conduction mechanisms of the P3HT/c-Si diode. At low forward bias, the current is limited by multi-tunneling capture emission, while at medium forward bias the current is limited by tunneling-enhanced recombination. Both mechanisms are related with hopping between localized states next the P3HT/c-Si interface.

Using conduction mechanism analysis, several physical parameters of the P3HT layer were calculated: charge concentration, electron affinity and characteristic temperature of the exponential trap distribution. These values were in good agreement with those obtained by other electrical and optical calculation methods. Additionally, a band diagram for the structure was proposed using the above values. The method used to study the hybrid structure was useful not only for determining the conduction mechanism but also for calculating the fundamental physical parameters in the material commented above. A similar procedure can be used to study any other organic semiconductor.

The conduction mechanism limiting the dark current-voltage characteristics in the Pc/C_{60} heterojunction was tunneling-enhanced interface recombination. From the C-V characteristics we calculated the charge concentration for Pc and C_{60}. Also for this structure a band-energy diagram in equilibrium was simulated and validated with experimental C-V characteristics.

The effect of C_{60} thickness and charges concentrations were studied by simulations.

Some relations in the simulated EBD were then proven. This EBD shows the consistency of conduction mechanism analysis with capacitance voltage characteristics.

Also for the Pc/C_{60} structure, three devices were prepared with different C_{60} thicknesses. The device prepared with the highest thickness of C_{60} performed the best, mainly due to an increase in photocurrent. After performing a variety of simulations, we suggested that reduction in geminated pairs and their subsequent recombination at the interface contribute to the photocurrent increases.

For the P3HT:PCBM structure, the conduction mechanism of a P3HT:PCBM solar cell was determined for samples with only one conduction mechanism. We found that multi-tunneling capture emission limited the current in the medium voltage range.

Finally, for P3HT:PCBM the DOS distribution was calculated using impedance spectroscopy. It was useful to study how the hole transport layer (HTL) affected the stability of the device.

The methods presented in this thesis and the interpretations of the results are a new approach in the study of organic solar cells. These results support the thesis that we can use the experience gained from both the technology and physics of inorganic devices, especially from thin film technologies.

Finally, some of the unsolved topics that need to be addressed in the future are: the light dependence of the ECD parameters, a consistent ECD for OBHT modeling applied to devices that present two conduction mechanisms, and further research into DOS calculation, which has been shown to be a powerful tool for studying these devices.

Appendixes

Appendix A: Fabrication of solar cells

1) P3HT/Si hybrid solar cell

Ohmic back-contact was made by thermal evaporation of Al on an n-type silicon wafer with a doping level N_{Si} = 3.5×10^{17} cm^{-3}. After standard RCA cleaning and before the polymer layer was deposited, the Si wafer was dipped into a 10% dilution of HF to eliminate any residual oxide. P3HT was then spin-coated at 5000 rpm. Finally, 30 nm-thick gold top contacts were deposited by sputtering using a mechanical mask. Fig. 3.2 shows a top view of one device. Typically, P3HT forms an ohmic contact with gold. [74]

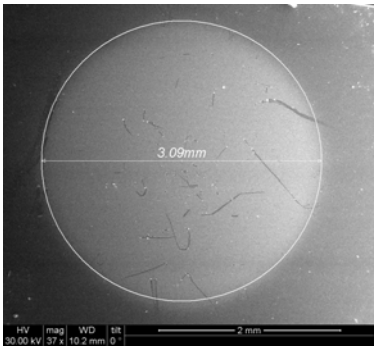

Fig. A.1: Top view of Au/P3HT/n-type crystalline silicon/Al heterojunction.

The polymer film was determined to be around 90 nm thick by ellipsometry. The fabricated structure was annealed at 120 ^{o}C.

2) Pentacene/C_{60} solar cell

Devices were fabricated on cleaned indium tin-oxide-coated glass substrates with a resistance of 4 Ω/sq. The C_{60}, Pc and Al were deposited by thermal evaporation at a pressure of $2 \cdot 10^{-6}$ bar. All materials were used as received without further purification. The device structure was: ITO (250 nm) / Pc (40 nm) / C_{60} (30 nm) / Bathocuproine (12 nm) / Al (150 nm). Thicknesses were verified with an Ambios XP-1 profilometer. Devices have an active area of A = 0.09 cm^2.

Fig. A.2 shows the glove box used for solar cell fabrication. The thermal evaporator is inside the glove box.

Fig. A.2 Glove box

Fabrication details of the samples with different C_{60} thicknesses.

In this case, in order to have equal Pc/C_{60} interfaces, the C_{60} layers were evaporated in three steps. First, a C_{60} film of 30 nm was evaporated on the three samples at the same time. After one sample had been removed from the chamber, another 8 nm of C_{60} was evaporated to obtain a thickness of 38 nm. Finally, after one of the two remaining samples had been removed, 24 nm was deposited in order to obtain a thickness of 62 nm. Thicknesses were verified with an Ambios XP-1 profilometer. The devices had an active area of A = 0.09 cm^2.

3) P3HT: PCBM bulk heterojunction solar cells

The glass substrates were acquired with a previous deposited film of ITO. In some cases the ITO contact area was defined by etching and in other cases this pattern was defined by the manufacturer. P3HT and PCBM were obtained from commercial houses.

The fabrication of the device can be sensitized in the following steps:

1. Cleaning of ITO substrates: this was done in acetone and isopropyl alcohol using an ultrasonic bath followed by oxygen plasma treatment.

2. P3HT:PCBM blend preparation: the organic semiconductors were blended in chlorobenzene. Although the percentage of each material in the blend can vary, it is generally around 1:1. The solution was kept under stirring for several hours.

3. Hole transport layer (HTL) deposition: this layer is useful for smoothing the ITO surface and obtaining ohmic contact with the active layer. Typically, PEDOT:PSS is used and deposited by spin-coating. After layer deposition the samples were dried by heating.

4. Active layer deposition: the active layer was spin-coated on top of the HTL.

5. Cathode deposition: the cathode material can be Al, Ca, Ag. After cathode deposition the devices were annealed.

6. Solar cell encapsulation: this was done using a cover glass plate with an epoxy resin.

Fig. A.3 shows a substrate with four P3HT:PCBM solar cells. This cell is encapsulated with a cover glass plate with an epoxy resin.

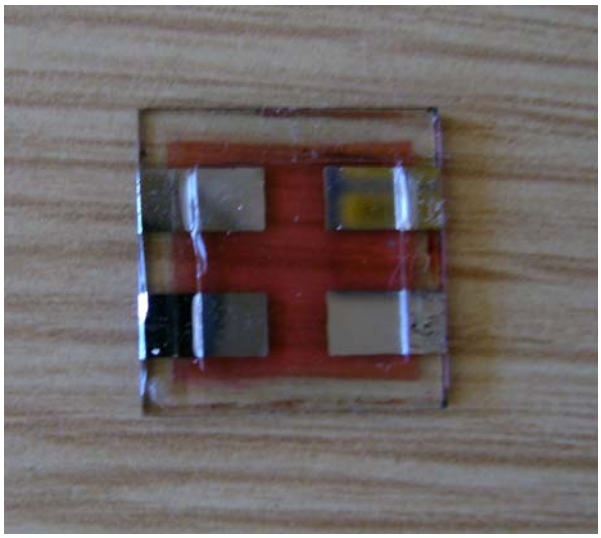

Fig. A.2 Substrate with four P3HT:PBM solar cells.

Appendix B

Electrical characterization techniques

1) Illuminated I-V curves

The illuminated I-V measurements were performed using an Oriel 250 W Xenon lamp with the appropriate Oriel filters in order to simulate the desired 1.5 AM solar spectrum (see Fig. B.1). In this work the samples were inside an acrylic box in order to avoid degradation effects.

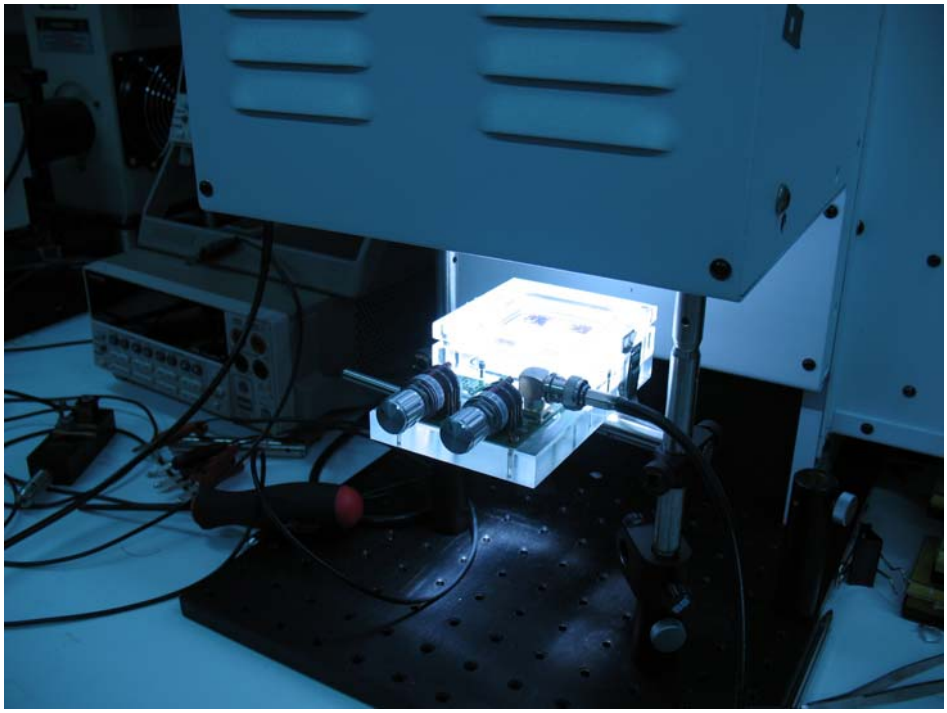

Fig. B.1 solar cell simulator

2) Dark I-V curves at different temperatures

Current-voltage-temperature (I-V-T) measurements were performed using an HP4145B semiconductor parameter analyzer and a K-20 temperature controller (see Fig. B.2). These were connected to the cryostat, where the sample was measured.

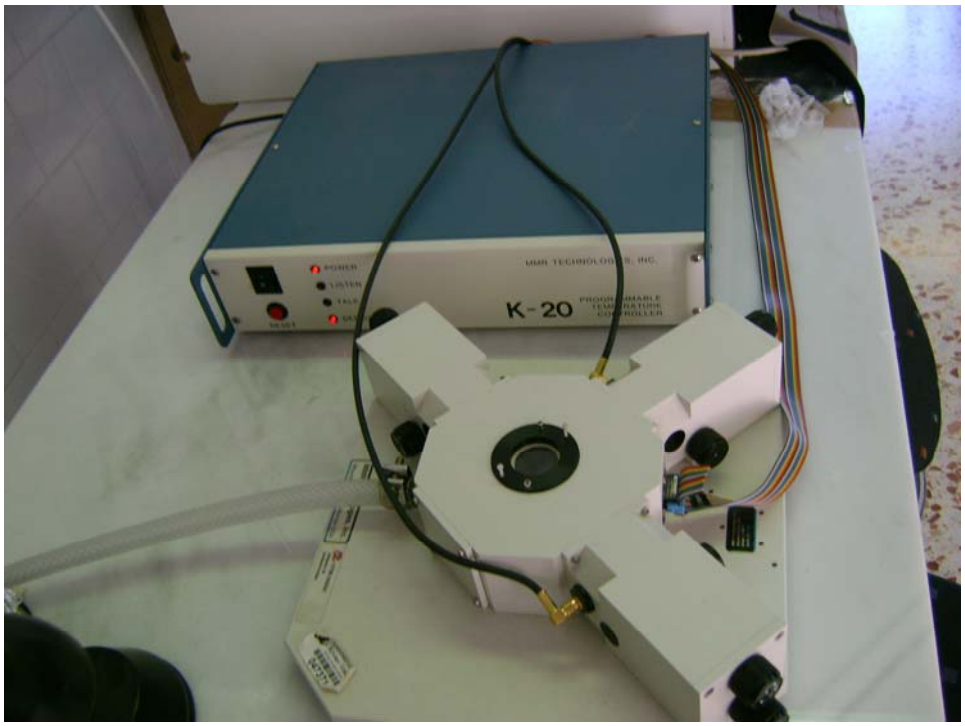

Fig. B.2 K-20 temperature controller and cryostat.

The K-20 was controlled by software.

3) Capacitance measurements

Capacitance measurements were performed using a 4192A LF impedance analyzer and four-point equipment (see Fig. B.3).

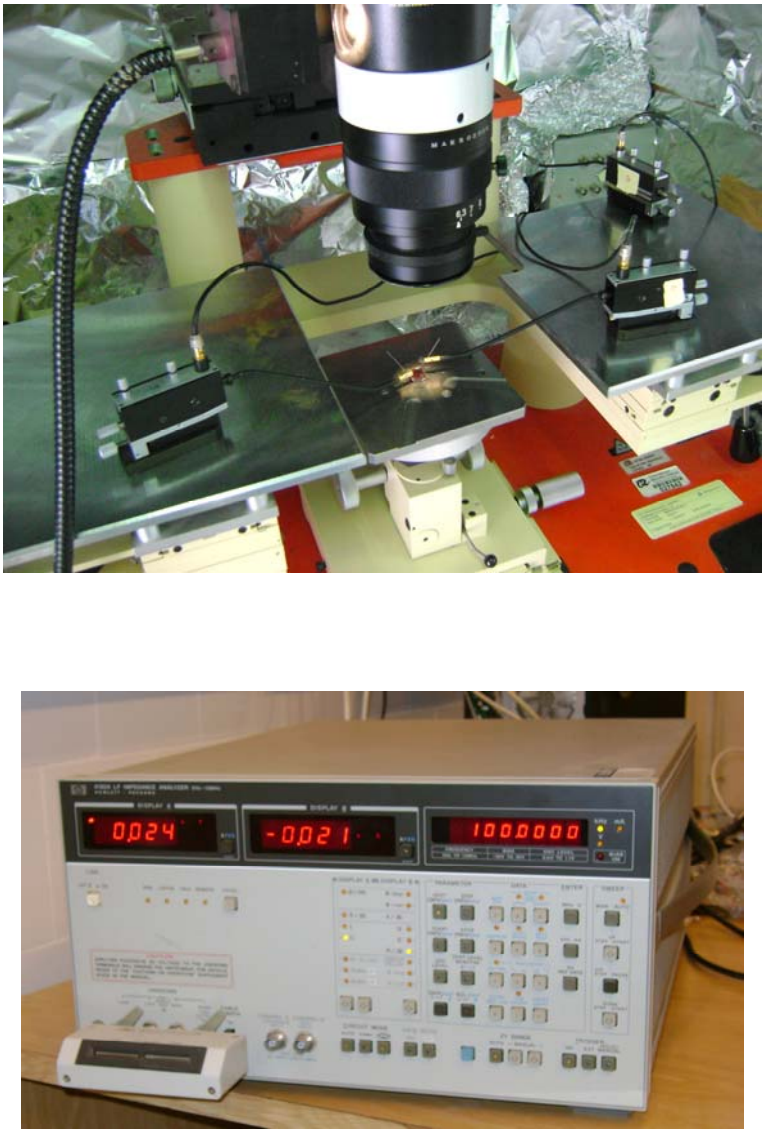

Fig. B.3 Four-point equipment (top) and a 4192A LF impedance analyzer (bottom).

Appendix C

Heterojunction simulator software (AFORST-HET)

AFORST-HET is a heterojunction simulator that solves one-dimensional semiconductor equations using Shockley-Read-Hall recombination statistics. It was developed by the Helmholtz Centre Berlin for Materials and Energy in Germany and can be obtained free over the Internet.

Fig. B.4 shows the main menu of AFORS-HET v2.2. This software is very easy to handle.

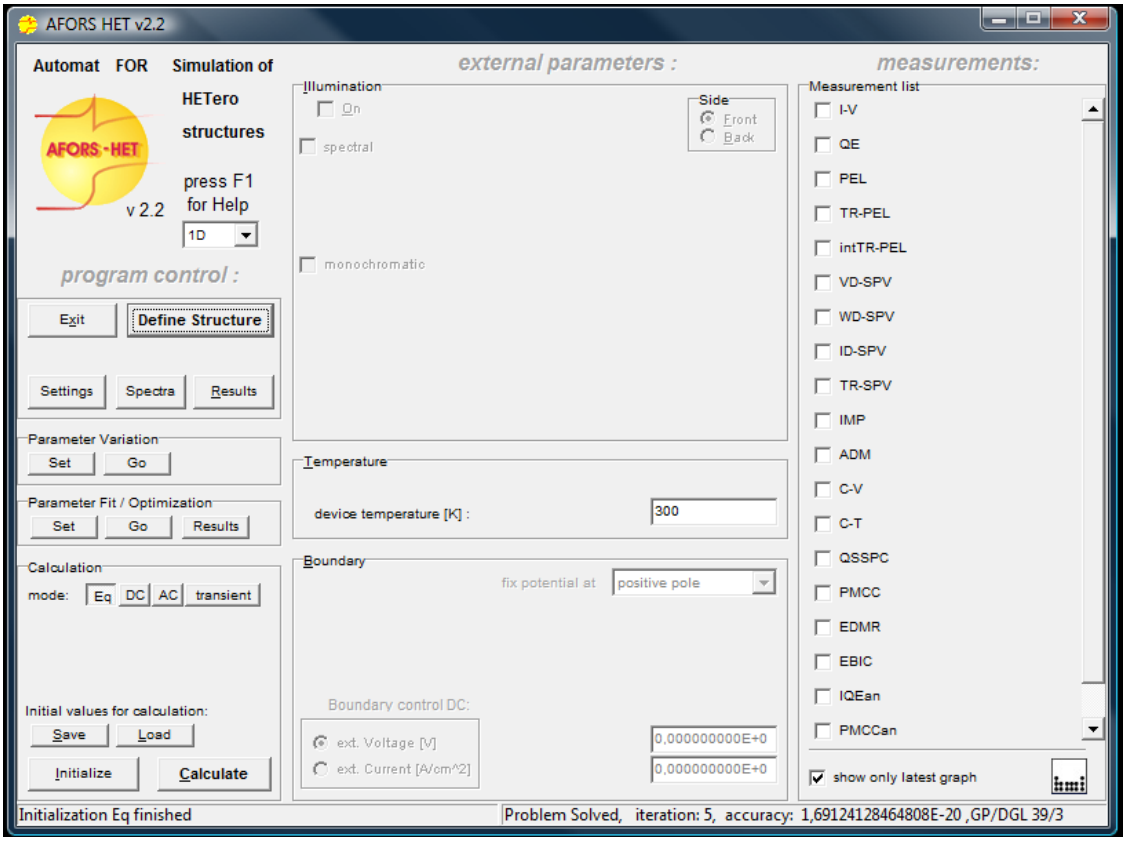

Fig. B.4 Main menu of AFORS-HET

To conduct a simulation, fundamental physical properties such as dielectric constants, electron affinity, band gap, effective DOS in the bands and charge carriers concentration must be defined for each layer. In theory these physical properties are enough to obtain C-V characteristics and band diagram simulations. Fig. B.5 shows an example of a band diagram simulation in AFORS-HET.

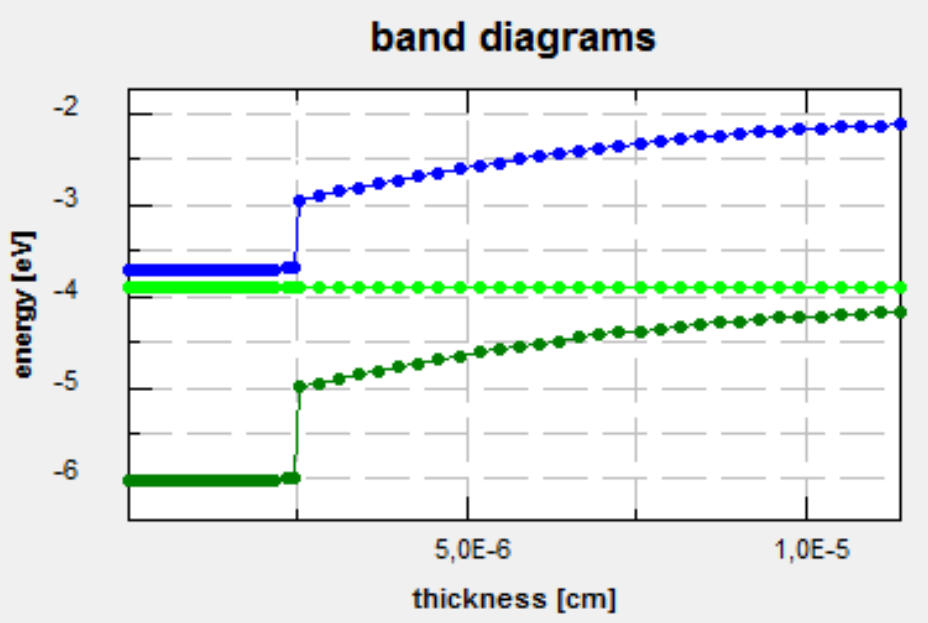

Fig. B.5 Energy band diagram simulation in AFORST-HET

AFORST-HET can be used to simulate several electrical and optical measurements for both transient and equilibrium states. Depending on the kind of simulation, additional parameters are required. For example, for I-V characteristics we need to specify the mobility of each material.

In this work we used AFORS-HET to simulate both energy band diagrams and C-V characteristics.

Figure B.6 show a $1/C^2$ vs V curve simulated in AFORS-HET.

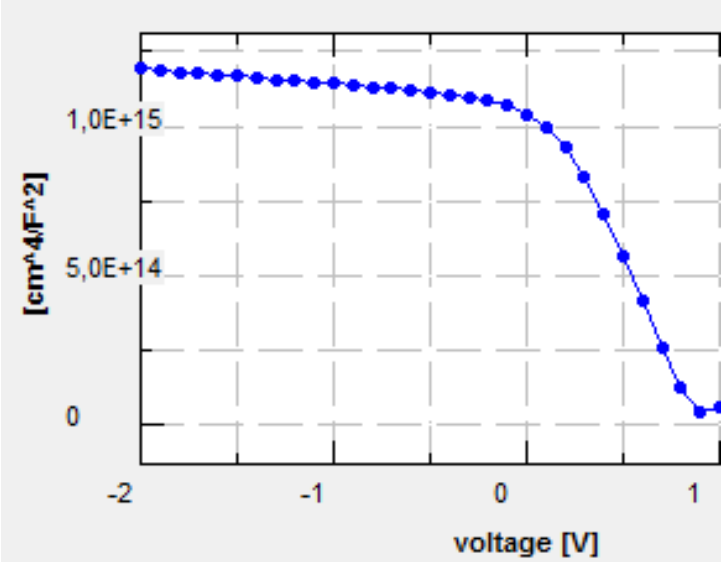

Figure B.6 Simulated $1/C^2$ vs V curve

Appendix D: List of abbreviations

A_i Exponential factor
a-Si:H Amorphous Silicon hydrogenated
β Capture cross section
c-Si Crystalline Silicon
C Capacitance
C_B Conduction band
CINVESTAV Centro de investigación y estudios avanzados, DF,México.
C-V Capacitance voltage characteristics
C-f Capacitance vs frequency measurements
d Layer thickness
D Diffusion coefficient
DOS Density of states
q Electron charge
E Energy
Ea Activation energy
EBD Energy band diagrams
ECD Equivalent circuit device
E_F Fermi level
E_{FN} Quasi Fermi-level of electrons
E_{FP} Quasi Fermi-level of holes
E_g Band gap
ε_i Semiconductor dielectric constant
EHF Energie-und Halbleiterforschung, Oldenburg Germany
E_T Localized state
FF Fill factor
HOMO Highest occupied molecular orbital
HTL Hole transport layer
ICIQ Institut Català d'Investigació Quimica, Tarragona Spain
IKERLAN Centro de inovaciones tecnológicas, Mondragon Spain
I_L Photocurrent
I_M Maximum current
Isc Short-circuit current
I_P Ionization potential
I-V Current voltage characteristics
I-V-T Current voltage temperature characteristics
ITO Indium thin oxide
Js Inverse saturation current
J_D Diode current
k Parameter of the SCLC mechanisms
k_B Boltzmann constant

L Diffusion length
LUMO Lowest unoccupied molecular orbital
m Parameter of the SCLC mechanisms
MIM Metal-Insulator model
MTCE Multituneling capture emission
MTR Multi-trapping and release process
N_i Charge carrier concentration
N_A Concentration of aceptors
N_C Effective DOS in the conduction band
N_D Concentration of donors
N_{ph} Photon flux density
n Ideality factor
n_i Intrinsic concentration
η Solar cell efficiency
η_{EQE} External quantum efficiency
ni Intrinsic concentration
N_V Effective DOS in the valence band
OBHT Organic bulk heterojuntion
P3HT Poly (3-hexylthiophene)
Pc Pentacene
Φ_b Interface barrier
P_M Maximum power
R_L Load resistance
R_S Series resistance
R_{SH} Parallel resistance
SCLC Space charge limited current
STB Somewhat bound state
STF Free sate
STL Transit laying state
σ Variance of the DOS distribution
TEIR Tuneling-enhanced interface recombination
μ Mobility
V Applied voltage
V_B Valence band
V_{bi} Built-in potential
V_M Maximum voltage
V_{oc} Open-circuit voltage
Wfa Anode work function
Wfc Cathode work function
Wfp P-semiconductor work function
Wfn N-semiconductor work function
χ_i Electron affinity

References

[1] Z. D. Popovic, Mol. Cryst. Liq. Cryst. **171,** 103 (1989).

[2] H. Shirirakawa, E. J. Louis, A. G. MacDiarmid, C. K. Chiang and A. J. Heeger, Chem. Commun. 578, (1977).

[3] C. K. Chiang, C. R. Fincher, Y. W. Park. A. J. Heeger, H. Shirakawa and E. J. Louis, Phys. Rev. Lett. **39**, 1098 (1977).

[4] J. H. Burroughes, et. al., Nature, **341**, 539 (1990).

[5] G. Yu, J. Gao, J. C. Hummelen, F. Wudl and A. J. Heeger, Science, **270**, 1789 (1995).

[6] N. Mott & E. A. Davis, Electronic processes in non-crystalline materials, Oxford university press, (1979).

[7] R. A. Street, Adv. Mater. **21**, 2007 (2009).

[8] G. Hadziioannou, and G. G. Malliaras, Semiconducting Polymers, Weinheim Germany, (2007).

[9] S. Baranovski, Charge Transport in Disordered Solid with Applications in Electronics, Marburg Germany, (2006).

[10] M. Hanack and M. Lang, Adv. Mater. **6**, 819 (1994)

[11] M. Hanack, K. Duerr, A. Lange, J. Osio Barcina, J.Pohmer and E. Witke, Synth. Met. **71,** 2275 (1995).

[12] L. Q. Minh, T. Chot, N. N. Dinh, N. N. Xuan, N. T. Binh, D. M. Phuoc and N. T. Binh, Phys. Stat. Sol., **101,** 143 (1987).

[13] M. Katayose, S. Tai, K. Kamijima, H. Hagiwara and N.Hayashi, J. Chem. Soc. **2** 403 (1992).

[14] K. Y. Law, Chem.Rev., **93** 449 (1993).

[15] K. Y. Law, Handbook Org.Cond.Mol.Polym., **1,** 488 (1997).

[16] M. Pope, C. E. Swenberg: Electronic processes in Organic Crystals and polymers (Oxford Univ. Press, Oxford 1999).

[17] Y. Preezant and N. Tessler, Phys. Rev. B, **74**, 235202 (2006).

[18] M. A. Green, Silicon solar cells advanced principles and practice, University of New South Wales Sydney, (1995).

[19] S. Barth and H. Baessler, Phys.Rev.Lett., **79,** 4445 (1997).

[20] P. G. D. Costa and E. M. Conwell, Am.Phys.Soc.-Rap.Comm., **48**, 1993 (1993).

[21] M. Chandross, S. Mazumdar, S. Jeglinski, X. Wei., Z.Vardeny, E.W. Kwock and T.M. Miller J.Phys.: Condens.Matter **6**, 1379 (1994).

[22] Z. Xu and B. Hu, Adv. Funct. Mater., **18**, 2611 (2008).

[23] V. I. Arkhipov, E. V. Emelianova, P. Heremans and G. J. Adriaenssens, J. Optoelectr. Adv. Mater, 4, 425 (2002).

[24] M. C. J. M. Vissenberg and M. Matters, Phys. Rev. B. **57**, 12 964 (1998).

[25] D. Monroe, Phys. Rev. Lett. **54**, 146 (1985).

[26] S. M. Sze, Physics of semiconductor devices, John Wiley & Sons, New York (1981).

[27] C. Tanase, E.J. Meijer, P.W.M. Blom and D. M. de Leeuw, Phys. Rev. Lett. **91**, 216601 (2003).

[28] M. Lenes, S. W. Shelton, A. B. Sieval, D. F. Kronholm, J. C. Hummelen, and P. W. M. Blom, Adv. Funct. Mater., **19**, 3002 (2009).

[29] P. P. Boix, G. Garcia-Belmonte, U. Muñecas, M. Neophytou, C. Waldauf, R. Pacios, Appl. Phys. Lett., **95**, 233302 (2009).

[30] K. Petritsch, PhD Thesis Organic solar cells architectures, Graz Austria (2000).

[31] B. A. Gregg, Soft Mater., **5**, 2985 (2009).

[32] R. A. Street, Appl. Phys. Lett. **93**, 133308 (2008).

[33] D. Woehrle and D. Meissner, Adv. Mater., **3**, 129 (1991).

[34] G. A. Chamberlain, Solar Cells **8**, 47 (1983).

[35] N. F. Mott, Trans. Faraday Soc. **34**, 500 (1938).

[36] W. Schottky, Naturwiss. **26**, 843 (1938).

[37] M. Granstrom, K. Petritsch, A. C. Arias, A. Lux, M. R. Andersson and R. H. Friend, Nature, **395**, 257 (1998).

[38] E. Becquerel, C. R. Acad. Sci., **9**, 561 (1839).

[39] D. M. Chapin, C. S. Fuller and G. L. Pearson, J. Appl. Physc. , **25**, 676 (1954).

[40] S. Hegedus, Prog. Photovoltaics, **14**, 393 (2006).

[41] F. Dimroth and S. Kurtz, MRS Bull, **32**, 230 (2007).

[42] D. J. Milliron, I. gur and A. P. Alivisatos, MRS Bull, **30**, 41 (2005).

[43] M. Grätzel, Photochemical cells, Nature, **414**, 338 (2001).

[44] C. W. Tang, Appl. Phys. Lett., **48**, 183 (1986).

[45] http://www.pv-tech.org/news/_c/opv_dssc

[46] K. Petritsch, PhD Thesis, Cambridge and Graz (2000).

[47] A. Liu, S. Zhao, S. Rim, J. Wu, M. Konemann, P. Erk, and P. Peumans, Adv. Mat. **20**, 1065 (2008).

[48] H. Hoppe and N. S. Sariciftci, J. Mater. Res., **19**, 1924 (2004).

[49] O. Lundberg, M. Bodegård, J. Malmström, and L. Stolt, Prog. Photovoltaics, **11**, 77, (2003).

[50] J. Y. Kim, Science, **317**, 222 (2007).

[51] B. P. Rand, P. Pneumans and S. R. Forrest, J. Appl. Phys., **96**, 7519 (2004).

[52] A. L. Ayzner, C. J. Tassone, S. H. Tolbert and B. J. Schwartz, J. Phys. Chem. C., **113**, 20050 (2009).

[53] A. K. Pandey, P. E. Shaw, I. D. W. Samuel and J. M. Nunzi, Appl. Phys. Lett., **94**, 103303 (2009).

[54] J. J. M. Halls, K. Pichler, R. H. Friend, S. C. Moratti and A. B. Holmes, Appl. Phys. Lett. **68**, 3120 (1996).

[55] J. J. M. Halls and R. H. Friend, Synth.Met., **85** 1307 (1996).

[56] H. Wiesenhofer, et.al., Adv. Funct. Mater., **15**, 155 (2005).

[57] C. B. Murphy, et al., J. Phys. Chem. B, **108**, 1537 (2004).

[58] B. Kippelen and J. L. Bredas, Energy Environ. Sci., **2,** 251 (2009).

[59] G. A. Chamberlain, Solar Cells, **8**, 47 (1983).

[60] R. N. Marks, J. J. M. Halls, D. D. C. Bradley, R. H. Friend y A. B. Holmes, J. Phys.: Cond. Mat. **6**, 1379 (1994).

[61] K. Petritsch and R. H. Friend Synth.Met., **102**, 976 (1998).

[62] K. Tada, M. Onada, A. A. Zakhidov and K. Yoshino, Jpn. J.Appl. Phys. **36**, L306 (1997).

[63] G. Yu, J. Gao, C. J. Hummelen, F. Wudl and A. J. Heeger, Science, **270**, 1789 (1995).

[64] N. C. Greenham, X. Peng and A. P. Alivisatos, Phys. Rev. B, **54** 17628 (1996).

[65] H. Ago, K. Petritsch, M.S.P. Sha.er, A.H.Windle and R.H. Friend, Adv. Mat., **11**, 1281 (1999).

[66] X. Ai, N. Anderson, J. Guo, J. Kowalik, L. M. Tolbert, and T. Lian, J. Phys. Chem., **110**, 25496 (2006).

[67] K. Shankar, G. K. Mor, H. E. Prakasam, O. K. Varghese, and C. A. Grimes, Langmuir, **23**, 12445 (2007).

[68] P. Ravirajan, A. M. Peiro, M. K. Nazeeruddin, M. Graetzel, D. D. C. Bradley, J. R. Durrant, and J. Nelson, J. Phys. Chem, **110**, 7635 (2006).

[69] D. C. Olson, S. E. Shaheen, R. T. Collins, and D. S. Ginley, J. Phys. Chem, **111**, 16670 (2007).

[70] D. Tasis, N. Tagmatarchis, A. Bianco, and M. Prato, Chem. Rev. **106**, 1105 (2006).

[71] F Garnier, J. Opt., Pure and Appl. Opt., **4**, S247 (2002).

[72] Y. Shirota, and H. Kageyama, Chem. Rev. **107**, 953 (2007).

[73] W. Shockley, and H. J. Queisser, J. Appl. Phys. **32**, 510 (1961).

[74] M. A. Green, Solar cells; operating principles technology, and system applications, University of New South Wales Australia (1982).

[75] L. J. A. Koster. V. D. Mihailetchi and P. W. M. Blom, Appl. Phys. Lett. **88**, 093511 (2006).

[76] G. Dennler, M. C. Scharber and C. J. Brabec, Adv. Mater. **21**, 1323 (2009).

[77] M. F. Lo, et. al., Appl. Phys. Lett., **96,** 113303 (2010).

[78] C. Waldauf, M. C. Scharber, P. Schilinsky, J. A. Hauch, and C. J. Brabec, J. Appl. Phys., **99**, 104503 (2006).

[79] W. J. Potscavage, S. Yoo, and B. Kippelen, Appl. Phys. Lett., **93**, 193308 (2008).

[80] N. Li, Brian E. Lassiter, R. R. Lunt, G. Wei, and S. R. Forrest, Appl. Phys. Lett. **94**, 023307 (2009).

[81] R.A. Street and M. Schoendorf, Phys. Rev. B, **81**, 205307 (2010).

[82] P. Schilinsky, C. Waldauf, J. Hauch, C. J. Brabec, J. Appl. Phys., **95**, 3816 (2004).

[83] J. Pallares, R. Cabré, L.F. Marsal, R. E. I. Schropp, J. Appl. Phys. **100**, 084513 (2006).

[84] F. Schauer, Sol. Energy Mat. Sol. Cells **87**, 235 (2005).

[85] C. Deibel and A. Wagenpfahl, Phys. Rev. B, **82**, 207301 (2010).

[86] R. A. Street, Phys. Rev B, **82**, 207302 (2010).

[87] H. Matsuura, T. Okuno, H. Okushi, K. Tanaka, J. Appl. Phys. **55**, 1012 (1984).

[88] U. Rau, A. Jasenek, H. W. Schock, F. Engelhardt, and T. Meyer, Thin Solid Films **361–362**, 298 (2000).

[89] K. C. Kao and W. Hwang, Electrical Transports in Solids with Particular Reference to Organic Semiconductors, Pergamon Press, Oxford (1981).

[90] M. A. Lampert, P. Mark Current Injection in Solids, Academic Press, New York, 1970.

[91] H. Sirringhaus, N. Tessler, and R. H. Friend, Synth. Met. **102**, 857 (1999).

[92] L. Bürgi, T. J. Richards, R. H. Friend, and H. Sirringhaus, J. Appl. Phys. **94**, 6129 (2003).

[93] E. J. Meijer, C. Detcheverry, P. J. Baesjou, E. van Veenendaal, D. M. de Leeuw, and T. M. Klapwijk, J. Appl. Phys. **93**, 4831 (2003).

[94] J. C. Nolasco, M. Estrada, Y. Matsumoto, L. F. Marsal, J. Pallares, ECS Transactions **9**, 587 (2007).

[95] R. L. Anderson, Solid-State Electron. **5**, 341 (1962).

[96] M. Estrada, I. Mejia, A. Cerdeira and B. Iñiguez, Solid-State Electron. **52**, 53 (2008).

[97] M. Chang, C. Wu, Y. Chen, B. Hsieh, W. Huang, K. Ho, T. Hsieh, and Y. Han, Org. Electron. **9**, 1136 (2008).

[98] A. Rose, Phys. Rev. **97**, 1538 (1995).

[99] F. Torricelli, Zs. M. kovács-Vajna, and L. Colalongo, Org. Electron. **10**, 1037 (2009).

[100] C. Tanase, E. J. Meijer, P. W. M. Blom, and D. M. Leeuw, Phys. Rev. Lett. **91**, 216601 (2003).

[101] S. Yoo, B. Domercq, and B. Kippelen, Appl. Phys. Lett., **85**, 5427 (2004).

[102] A. C. Mayer, M. T. Lloyd, D. J. Herman, T. G. Kasen, and G. G. Malliaras, Appl. Phys. Lett., **85**, 6272 (2004).

[103] S. Yoo, et. al. , Solid State Electron. **51**, 1367 (2007).

[104] A. K. Pandey, and J.-M. Nunzi, Appl. Phys. Lett., **89**, 213506 (2006).

[105] P. Sullivan and T. S. Jones, Org. Electronics, **9**, 656 (2008).

[106] J. Yang and T.-Q. Nguyen, Org. Electronics, **8**, 566 (2007).

[107] M. Vogel, S. Doka, Ch. Breyer, M. Ch. Lux-Steiner, and K. Fostiropoulos, Appl. Phys. Lett. 89, 163501(2006).

[108] Chopra K. L. and Das S. R., Thin Film Solar Cells, pp. 173, Plenum Press, New York and London (1983).

[109] A. Fartash, Phys. Rev. B 54, 17215 (1996).

[110] Y. S. Yang, et. al., Appl. Phys. Lett. **80**, 1595 (2002).

[111] P. I. Djurovich, E. I. Mayo, S. R. Forrest, M. E. Thompson, Org. Electron. **10**, 515 (2009).

[112] D. Cahen and A. Kahn, Adv. Mater., **15**, 271 (2003).

[113] P. Peumans, A. Yakimov, and S. R. Forrest, J. Appl. Phys. **93**, 7 (2003).

[114] K. H. Bhuiyan and T. Mieno, Thin Solid Films **506-507**, 239 (2006).

[115] C. R. McNeill, S. Westenhoff, C. Groves, R. H. Friend and N. C. Greenham, J. Phys. Chem. C **111** (51), 19153 (2007).

[116] J. C. Nolasco, et. al., Proceedings of the 2009 Spanish Conference on Electron Devices, Santiago de Compostela Spain.

[117] V. S. Balderrama, et. al., Microelectronics Reliability, **51** 597 (2001).

[118] B. Ecker, et. al., Adv. Funt. Mater., DOI: 0.1002/adfm.201100429

[119] D. Chirvase, et. al., J. Appl. Phys., **93**, 3376 (2003).

[120] M. Jørgensen, K. Norrman, F. C. Krebs, Sol. Energy Mater. Sol. Cells, **92**, 686 (2008).

[121] M. O. Reese, A. M. Nardes, B. L. Rupert, R. E. Larsen, D. C. Olson, M. T. Lloyd, S. E. Shaheen, D. S. Ginley, G. Rumbles, N. Kopidakis, Adv. Funct. Mater. , **20**, 3476 (2010).

[122] M. O. Reese, A. J. Morfa, M. S. White, N. Kopidakis, S. E. Shaheen, G. Rumbles, D. S. Ginley, Sol. Energy Mater. Sol. Cells, **92**, 746 (2008).

[123] J. Schafferhans, A. Baumann, A. Wagenpfahl, C. Deibel, V. Dyakonov, Org. Electron., **11**, 1693 (2010).

[124] A. Seemann, H.-J. Egelhaaf, C.J. Brabec, J. Hauch, Org. Electron., **10**, 1424 (2009).

[125] K. Kawano, C. Adachi, Adv. Funct. Mater., **19**, 3934 (2009).

[126] I. Torres, D. M. Taylor, E. Itoh, Appl. Phys. Lett., **85**, 314 (2004).

[127] T. Walter, R. Herberholz, C. Mueller, H. W. Schock, J. Appl. Phys., **80**, 441 (1996).

[128] F. T. Reis, L. F.Santos, R. F. Bianchi, H. N. Cunha, Appl. Phys. A, **96**, 909 (2009).

[129] O. D. Jurchescu, B. H. Hamadani, H. D. Xiong, S. K. Park, S. Subramanian, N. M. Zimmerman, J. E. Anthony, T. N. Jackson, D. J. Gundlach, Appl. Phys. Lett., **92**, 132103 (2008).